Structuring Light: From knots to geometrical phases

by

Manuel Francisco Ferrer Garcia

A thesis
submitted to the University of Ottawa
in partial fulfillment of the
thesis requirement for the degree of
Doctor of Philosophy
in
Physics

Abstract

Undoubtedly, light is one of the physical phenomena that has amazed humanity for millennia. In the past decades, rapid advances in technology have allowed us to study the *hidden* features of the electromagnetic field. Structured light – light beams whose intensity, phase profile, polarization, or frequency distribution has been tailored on demand – became a tool to explore the intersection between Maxwell's equations and abstract mathematical concepts. The use of topology has become ubiquitous in photonics, such as the existence of caustics and optical systems that mimic the behavior of solid-state systems, among others. Here, physicists have taken advantage of quantities that stay unchanged under deformations, known as topological invariants, to obtain information regarding the nature of the system of interest.

In this work, I propose the use of structured light as a platform to explore the topological effects in different fields of optics. As our first attempt, we numerically explore the relationship between the dislocations carried by a structured field and the landscapes carved on a dispersive-absorptive substrate in the paraxial and nonparaxial regime. Inspired by the three-dimensional fields obtained by means of a high-numerical-aperture lens, we introduce a simple methodology to *tie* the tip of the electric field and generate knotted polarization states. In parallel, we propose the use of framed knots to encode and share information. In contrast to the non-trivial polarization states, these knots are obtained by tracking the spatial evolution of the singular points in the field along propagation. Finally, we study the nature of the time-independent acquired Pancharatnam-Berry phase as a function of the strength of a measurement. The results of these developments could have implications for current and future research to unveil new physics phenomena inspired by topology. The authors foresee advances in structuring non-paraxial light, exotic light-matter interactions, and optical metrology, among others.

Acknowledgments

First of all, I want to express my sincere gratitude to my supervisor Prof. Ebrahim Karimi. His continuous motivation, patience, support, and valuable advice throughout my PhD, not only make me a better scientist but a better person. I was privileged to continue pursuing my research career in such a diverse and dynamic scientific environment.

I would like to thank Alessio D'Errico for his unconditional and invaluable advice. Sharing and discussing crazy new ideas was one of the most enriching experiences during my graduate studies. Thank you for your patience inside and outside the laboratory; I will forever treasure everything I learned from you. I would like to extend my gratitude to all the members of the SQO group for all their help and moral support during my PhD. Thank you, Tareq, Lukas, Florence, Xiaoqin, Alicia, Felix, Francesco, Dilip, Kevin, Tugrul, Sergei, Qasem, and Nazanin. You taught me so much; I will carry it wherever I go. I wish to thank all my collaborators, Hugo Larocque, Eliahu Cohen, Avishy Carmi, Kyrylo Snizhko, Alessandro Romito, Yuval Gefen, and Yousef Alvandi. Your guidance and patience allowed me to open my eyes to new physics. I look forward to seeing you at conferences and discussing new ideas.

Thanks to all the people I met at the University of Ottawa. Especially to Yaryna, Daniel, Ryan, Aldo, Kate, Yaswant, Theng-Loo, Ashish, Evan, Alina, and Paris for all the fruitful discussions, nonsense conversations, support, and advice during these four years. I have the fortune of not only calling you colleagues but also my friends. In addition, I would like to thank Eric, Anushree, and Zemar for sharing the good and bad days in Ottawa. Special thanks to my friends abroad, Daniel H., Daniel J., Ana, Anabel, Joel, Antonio, Luis, Israel, and Viviana. In addition, I extend my deepest gratitude to Benito Antonio Martinez Ocasio and Ramón Luis Ayala Rodríguez, for their motivation during the long hours at work. Although we are far away, you never stopped believing in me. I have no words to express how lucky and thankful I am for having my back.

Finally, I would like to thank my family, particularly my parents Manuel Ferrer and Maria Eugenia García, for their unconditional support. No siempre fue sencillo dar el siguiente paso, pero ustedes siempre me ayudaron a poner un pie frente al otro. Gracias por ayudarme a lograr mi sueño. Este logro es tan suyo como mio.

Live life. Do not let life lives you.

List of Publications

1. **M. F. Ferrer-García**, Y.Alvandi, Y. Zhang, and E.Karimi, "Theoretical analysis on spatially structured beam induced mass transport in azo-polymer films." *Optics Express* **28**, 19954-19965 (2020).

2. H. Larocque, A. D'Errico, **M. F. Ferrer-García**, A. Carmi, E. Cohen, and E. Karimi. "Optical framed knots as information carriers." *Nature communications* **11**, 5119 (2020).

3. **M. F. Ferrer-García**, A. D'Errico, H. Larocque, A. Sit, and E. Karimi, "Polychromatic electric field knots." *Physical Review Research* **3**, 033226 (2021).

4. **M. F. Ferrer-García**, A. Carmi, A. D'Errico, H. Larocque, E. Cohen, and E. Karimi, "Secure communication using low dimensional topological elements." *arXiv*:2212.04350 (2022).

5. **M. F. Ferrer-García**, K. Snizhko, A. D'Errico, A. Romito, Y. Gefen, and E. Karimi, "Topological transitions of the generalized Pancharatnam-Berry phase." *Science advances*, **9**(47), eadg6810.(2023).

6. L. Scarfe, F. Hufnagel, **M. F. Ferrer-García**, A. D'Errico, K. Heshami, and E. Karimi, "Fast Adaptive Optics for High-Dimensional Quantum Communications in Turbulent Channels." *arXiv*:2311.13041 (2023).

Statement of originality and collaborative contributions

To the best of his knowledge, the author states that the work described in this document constitutes original research in the field of physics. Bellow, we provide the collaborative contribution of each participant for every chapter.

E. Karimi and Y. Zhang conceived the idea for the work presented in chapter 2 regarding the landscape modification on an azopolymer thin film by means of structured light. M. Ferrer-Garcia and Y. Alvandi performed the numerical simulations and analysis of the obtained data. M. Ferrer-Garcia and E. Karimi wrote the manuscript with help from all the authors. All authors discussed the results and contributed to the text of the manuscript.

M. Ferrer-Garcia, A. D'Errico, A. Sit and E. Karimi conceived the idea presented in chapter 3, on generating knotted polarization curves using tightly focused beams. M. Ferrer-Garcia and A. D'Errico designed the optical fields. M. Ferrer-Garcia performed the simulations. M. Ferrer-Garcia and H. Larocque analyzed the data. M. Ferrer-Garcia, A. D'Errico, and E. Karimi wrote the manuscript with help from all the authors. All authors discussed the results and contributed to the text of the manuscript.

A. Carmi, E. Cohen, H. Larocque and E. Karimi initiated the work presented in chapter 4 about using optical knots to encode information. M. Ferrer-Garcia and A. Carmi described the challenge-response algorithm used for secure communications presented in chapter 4. M. Ferrer-Garcia, A. D'Errico, and E. Karimi wrote the manuscript with help from all the authors. All authors discussed the results and contributed to the text of the manuscript.

K. Snizhko, A. Romito, Y. Gefen, and E. Karimi conceived the idea presented in chapter 5 on detecting the measurement's strength-dependent topological transition of the Pancharatnam-Berry phase. M. Ferrer-Garcia, A. D'Errico, K.Snizhko, and E. Karimi designed the experiment. M. Ferrer-Garcia and K. Snizhko performed the theoretical simulations. M. Ferrer-Garcia and A. D'Errico performed the experiment and collected the data. M. Ferrer-Garcia, A. D'Errico, and K.S. analyzed the data. M. Ferrer-Garcia, K. Snizhko, A. D'Errico, and A. Romito prepared the first version of the manuscript. All authors discussed the results and contributed to the text of the manuscript.

List of Figures

Contents

Chapter 1

Introduction

Light is a phenomenon that has captivated the imagination and curiosity of humanity for millennia. However, the correct description of its nature was a mystery that eluded some of the greatest minds in history. It was not until James C. Maxwell introduced to the world a set of equations that describes the electromagnetic phenomena [1]. Therefore, the behavior of all electromagnetic radiation – including light – is dictated by solutions to Maxwell's equations. Traditionally, the study of electrodynamics heavily relies on using simple models such as plane waves [2]. These ideal, almost mythological, structures are characterized by having a constant phase and uniform intensity over the transverse plane and form. However, while mathematically convenient, it is not difficult to show that plane waves are not physically realizable since they carry an infinite amount of energy [2]. In reality, optical fields are described as time-dependent complex vector fields obtained from solving Maxwell's equations under specific constraints. The resultant light structures possess many degrees of freedom, providing physicists with tools for exploring new optical phenomena. Unequivocally, one of the features that caught the attention of the community is the existence of singular points in the electric field. For our purposes, a singularity can be defined as a location in space and time in which some variable associated with the field is defined [3]. Nevertheless, not all singularities are created equally. Arguably, the first study on singularities of the electromagnetic field can be attributed to Paul Dirac and his postulates of the magnetic monopoles in quantum theory [4]. In general, it is accepted that the first observation of singular points in optical fields is given in the work of Hans Wolter. On his way to unravel a physical explanation for the Goos–Hänchen shift, Wolter discovered the existence of singularities of the Poynting vector in the form of power flow circulation around points in space [5]. Later on, a similar circulating power flow pattern was observed near the focus on the diffracted field after going through a lens [6].

Curiously, Wolten concluded his work with thought-provoking speculation: this *circulation* phenomena may be present in more areas of optics. This statement became a reality when John Nye and Michael Berry introduced the study of phase singularities in a seminal paper [7]. Since its foundation, the study of optical singularities, or *singular optics*, has led to the discovery of a plethora of different optical phenomena. Unquestionably, the rapid growth of the field during the last twenty years can be attributed to *vortex* beams. These beams get their name from the characteristic behavior of the field in the vicinity of the singularity: as we move on an oriented path around the singular point, a feature of the field seems to *circulate*, resembling amphidromic points on tides [8]. In general, it is possible to distinguish two main types of optical vortices. The first type belongs to the realm of singularities of the scalar complex amplitude of the fields. Although it is possible to find relatively easy phase singularities in random fields [9], we focus our attention on the family of solutions to Maxwell's equations carrying optical singular points, such as the Bessel beams or Laguerre-Gauss modes [10], among others. In this case, the wavefront acquires an azimuthal structure such that the optical phase advances or retards by a multiple of 2π around the singularity. As a result of the undefined value for the phase, they have a zero-value intensity at the singular point [10]. Possibly, one of the most important features of an optical vortex is its linkage with the orbital angular momentum of light (OAM) [11]. On the other hand, the second type of optical vortices is related to the vector nature of light. In this case, the singularities arise from the non-uniformity of the polarization distribution [12]. In contrast to the scalar case, the behavior of the field may adopt a number of different configurations due to the vector properties of the polarization [13]. Independently of their nature, optical vortices have found a wide range of applications in classical and quantum communications [14–17], microscopy [18, 19], among others.

Introduced in [7], the study of optical singularities implied the existence of hidden-in-plain-sight symmetries complex structures in the electric field. An example of these structures is described by the dynamics of the optical singularities upon propagation. As the optical beam evolves in space, the singular points may move on the transverse plane. When the positions are recorded and connected, the existence of an organized three-dimensional structure is revealed [20]. While the skeleton simply traces a straight line for Laguerre-Gaussian modes, non-trivial structures such as braids or knots occur when more complex engineered beams [21, 22]. The existence of these topological features of the electric field has forced physicists to borrow tools from mathematicians to study these systems. In simple words, topology can be defined as the study of space properties that remain unchanged under continuous deformations. For example, a sphere cannot be deformed into a doughnut without punching a hole in the sphere. By doing so, we would violate the assumption of a continuous transformation. However, a common mug and the

doughnut can indeed be smoothly deformed from one into the other. Thus, it is said that they belong to the same *equivalent class*. In this case, the number of present holes in a body takes the role of a topological invariant: a quantity that all the realizations in an equivalent class possess and does not change upon deformations [23]. Nevertheless, the presence of topological features in optics is not only restricted to the singularities: solutions to Maxwell's equations have been found such that field lines trace knots and links in space [24, 25] and the generation of *hula-hoop* solitons has been proposed in laser media with fast saturable absorption [26], among others.

The work presented in this thesis aims to explore the effect of topological features and optical beams by means of structured light beams in different regimes. In the rest of this chapter contains a succinct introduction to the formalism used to describe structured light beams. Here, we cover the concepts of spatial modes, the vector nature of light, and its use to describe spatially-variant polarized fields in the paraxial regime. In chapter 2, we numerically investigate the effect of light beams with a spatially-variant polarization distribution on a dispersive-absorptive substrate. Here, the comparison between beams carrying phase and polarization singularities is made in both paraxial and nonparaxial regimes. In chapter 3, we theoretically explore a strategy to create knotted polarization curves using tightly focused polychromatic vector fields. As a result, large and rich populations of nontrivial polarization states are obtained within a focal volume. Meanwhile, in chapter 4, we introduce the use of optical frame knots to carry information securely between two points. To do so, we use the framed braid representation of the knot to encode prime numbers. In addition, we extend the original work and propose a challenge-response algorithm based on framed links that may be used for authentication purposes. Finally, in chapter 5, we investigate both, theoretically and experimentally, the behavior of the Pancharatnam-Berry phase acquired after a sequence of measurements. Our results prove the existence of a topological transition in the geometrical phase as a function of the measurement's strength. Additionally, the proposed measurement protocol shows robustness despite the presence of certain imperfections in the experimental implementation.

1.1 Structuring light

It is possible to define optical modes as solutions to Maxwell's equations that form a complete and orthogonal basis [27]. Let us consider that our set of modes is a composite space where each subspace is directly related to a particular degree of freedom in our electric beam. For the sake of simplicity, we restrict ourselves to the ones of our interest that can be applied to laser beams in the laboratory. In the absence of sources, it is possible

to obtain wave equations for the electric field by arranging Maxwell's equations in vacuum. For our purposes, we focus on the electric field, but similar procedures can be followed for the magnetic field [28]. By considering a monochromatic light source with frequency ω, it is possible to rewrite the wave equation, yielding the vector Helmholtz equation. While it is possible to find solutions to the vector Helmholtz vector [29], we prefer transverse wave fields whose propagation direction is orthogonal to their wave vector at each point of space. Therefore, it becomes possible to identify two elements in the electric field of a different nature: a unitary vector defining the field's polarization and a complex scalar amplitude function. In general, it is possible to decompose the electric field polarization vector in different two-dimensional bases, such as the Cartesian basis $\{\hat{\mathbf{x}}, \hat{\mathbf{y}}\}$ or the circular basis $\{\hat{\mathbf{L}} = (\hat{\mathbf{x}} + i\hat{\mathbf{y}})/\sqrt{2}, \hat{\mathbf{R}} = (\hat{\mathbf{x}} - i\hat{\mathbf{y}})/\sqrt{2}\}$.

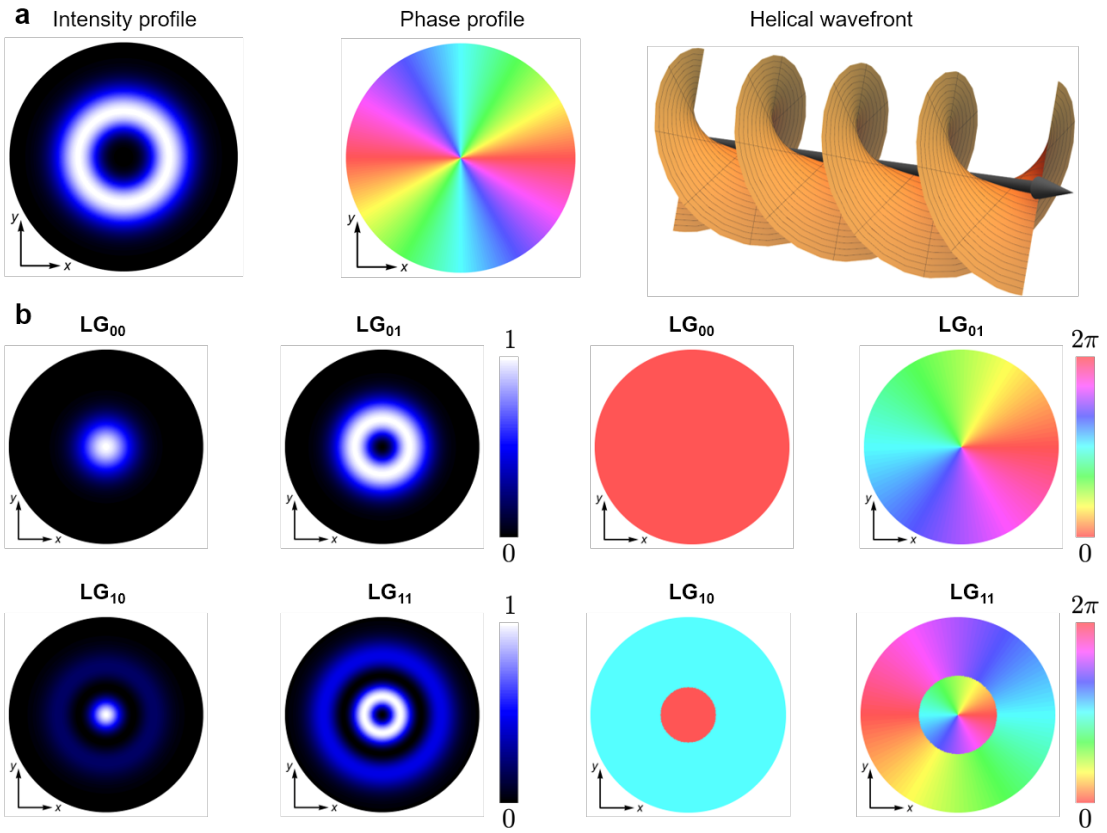

Figure 1.1: **Laguerre-Gaussian Modes.** **a.** Intensity and phase distribution of a Laguerre-Gaussian (LG) mode and its corresponding helical wavefront structure. **b.** Intensity and phase distributions for different LG modes.

On the other hand, the complex amplitude is obtained by solving the scalar wave equation. Although the mythical plane and multiple families of diffraction-free beams are theoretically-convenient solutions, they are not physically realizable in real optical systems. In the laboratory, it is common to deal with light beams that are solutions to the scalar wave equation under the paraxial approximation, i.e., the amplitude remains virtually unchanged along propagation [10]. In the cylindrical coordinate system, (r, ϕ, z), the solution yields the orthonormal family of optical modes known as Laguerre-Gaussian (LG),

$$\begin{aligned}\mathrm{LG}_{p,\ell}(r,\phi,z) =& \sqrt{\frac{2p!}{\pi(p+|\ell|)!}}\frac{1}{w(z)}\left(\frac{\sqrt{2}r}{w(z)}\right)^{|\ell|} L_p^{|\ell|}\left(\frac{2r^2}{w(z)^2}\right)\exp\left[-\frac{r^2}{w(z)^2}+i\ell\phi\right] \\ &\times \quad \exp\left[-i(2p+|\ell|+1)\arctan\left(\frac{z}{z_R}\right)+ik\frac{r^2 z}{2(z_R^2+z^2)}\right], \end{aligned} \tag{1.1}$$

where $L_p^{|\ell|}(\cdot)$ is the generalized Laguerre polynomial with radial index $p \in \mathbb{N}$ and azimuthal index $\ell \in \mathbb{Z}$, $w(z) = w_0\sqrt{1+z^2/z_R^2}$ is the spot parameter, w_0 is the beam waist, $z_R = \pi w_0^2/\lambda$ is the Rayleigh range and $k = 2\pi/\lambda$ is the wave number. The transverse intensity of these beams at a plane z corresponds to $p+1$ concentric rings, while the phase is represented by $|\ell|$ intertwined helical wavefronts whose handedness depends on its sign, see Figure 1.1-b. It should be noted that LG modes form a complete orthonormal basis under the operation,

$$\int_0^{2\pi}\int_0^{\infty} \mathrm{LG}_n^m(\mathbf{r})\ \left[\mathrm{LG}_q^p(\mathbf{r})\right]^* r\mathrm{d}r\mathrm{d}\phi = \delta_{mp}\delta_{nq}, \tag{1.2}$$

where δ_{mn} is the Kronecker delta symbol. Therefore, it is possible to decompose any field at a given plane z as a superposition of LG modes. As mentioned previously, the wavefront of an LG mode with $|\ell| \geq 1$ is not flat. As we circle the optical axis on a particular plane, the field phase experiences $|\ell|$ increments by 2π, generating an interweaved helical wavefront, see Fig. 1.1-a. Moreover, the phase at $r = 0$ becomes indeterminate, leading to a phase singularity with a topological charge of $|\ell|$.

1.1.1 Vector nature of light

As discussed above, light is a transverse electromagnetic wave oscillating on a plane orthogonal to its wavevector $\mathbf{k}$. A monochromatic field propagating towards the z direction

is given by

$$\mathbf{E}(\mathbf{r}) = \begin{bmatrix} U_x e^{i\Phi_x} \\ U_y e^{i\Phi_y} \end{bmatrix}, \tag{1.3}$$

where U_i and Φ_i are the amplitude and phase of the Cartesian component of the electric field. Eq. (1.3) defines a convenient representation of the complex electric field vector known as the Jones vector. In this formalism, the effect of a linear optical element is represented by a 2×2 matrix [30]. By multiplying Eq. (1.3) by the temporal phase, we can define the physical electric field vector

$$\boldsymbol{\mathcal{E}}(\mathbf{r}, t) = \mathrm{Re}\left[\mathbf{E}(\mathbf{r}) e^{-i\omega t}\right], \tag{1.4}$$

where ω is the angular frequency of the field. As shown in Figure 1.2-a, as it evolves the tip of the electric field vector traces a three-dimensional curve $\mathcal{C}_{3D}(t)$. Since $\boldsymbol{\mathcal{E}}(\mathbf{r}, t)$ is periodic, the projection of $\mathcal{C}_{3D}(t)$ to the transverse plane yields a simple oriented closed curve: the polarization ellipse. The handedness of the polarization state, i.e., the direction in which the electric field rotates, is typically defined as right(left)-handed if the rotation is (counter)-clockwise direction with respect to an observer looking at the incoming field [30].

While Jones formalism and the polarization ellipse are advantageous and elegant tools to describe the evolution of the electric field going through optical elements, they have a variety of limitations. For example, it is almost impossible to measure the oscillation of the electric field in real time in most scenarios since their period tends to be extremely short. Secondly, more complicated fields, such as partially polarized fields, lack a representation using the polarization ellipse. In 1852, George Stokes introduced the concept of describing light's polarization in terms of the contributions of different polarization bases [31]. The idea resurfaced years later as a mathematical alternative to the polarization ellipse. In general, the so-called Stokes parameters are defined as

$$S_0 = |E_x|^2 + |E_y|^2, \tag{1.5a}$$
$$S_1 = |E_x|^2 - |E_y|^2, \tag{1.5b}$$
$$S_2 = |E_{\pi/4}|^2 - |E_{3\pi/4}|^2, \tag{1.5c}$$
$$S_3 = |E_R|^2 + |E_L|^2, \tag{1.5d}$$

where the subscripts refer to different bases for the polarization: the rectangular $\{\hat{\mathbf{x}}, \hat{\mathbf{y}}\}$, a rectangular basis rotate by $\pm\pi/4$ and the circular basis $\{\hat{\mathbf{R}}, \hat{\mathbf{L}}\}$.

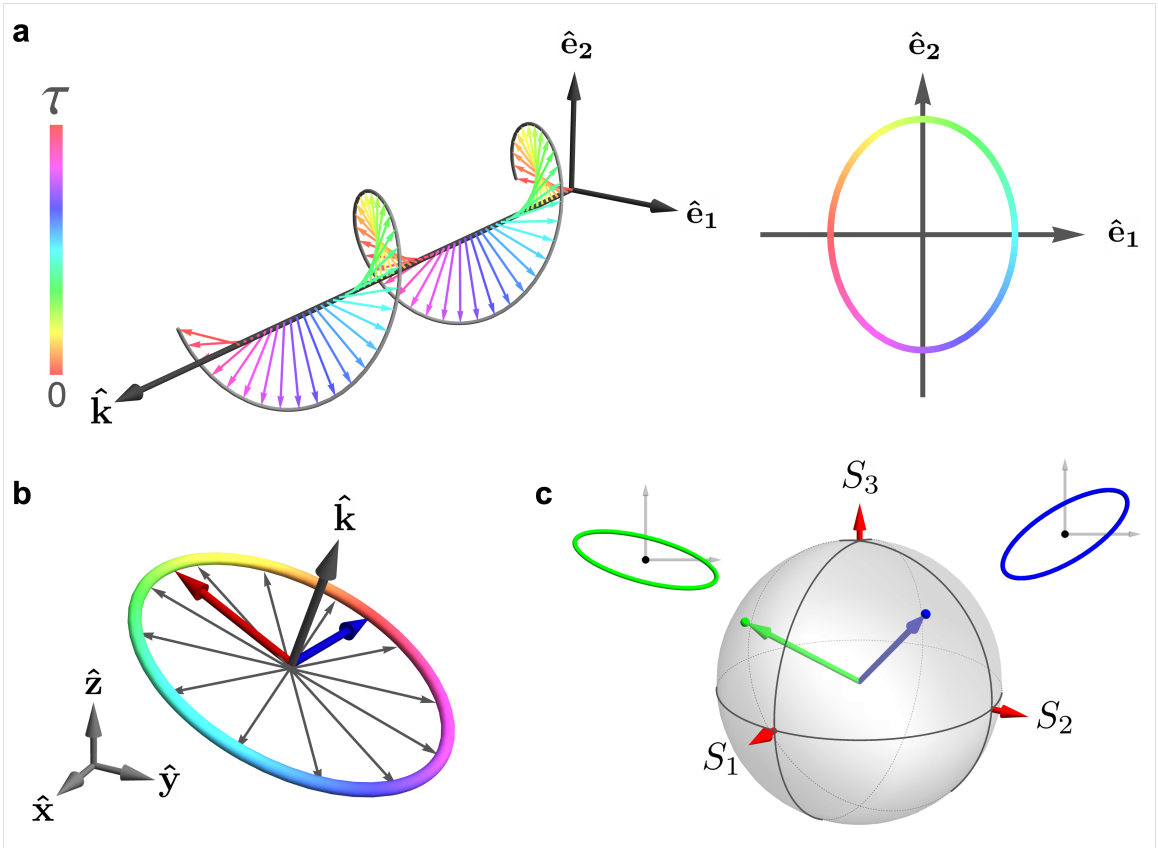

Figure 1.2: **Vector nature of light a.** The electric field vector for an elliptically polarized electromagnetic wave and its corresponding polarization ellipse. The period of the oscillation of the wave is τ. **b.** The three-dimensional polarization ellipse exists on the transverse plane to the vector $\mathbf{k}$. The major and minor axes of the ellipse are indicated by the red and blue arrows, respectively. **c.** The Poincaré sphere is a useful representation of the polarization states. Each point on its surface corresponds to a specific polarization state.

These parameters are often combined into a vector $\mathbf{S} = (S_0, S_1, S_2, S_3)$, known as the Stokes vector. In contrast to the polarization ellipse, it is possible to determine the degree of polarization (DOP) from the relation

$$\text{DOP} = \sqrt{\frac{S_1^2 + S_2^2 + S_3^2}{S_0^2}}, \tag{1.6}$$

which allows us to describe the ratio of light that is fully polarized. Partially polarized light has a DOP within the interval of $(0, 1)$, whereas the extreme values 0 or 1 correspond to the cases of unpolarized and fully polarized light, respectively [30].

Later on, Poincaré defined a one-to-one mapping between a polarization state $\hat{\mathbf{e}}$ and a point on the surface of a sphere with unitary radius by constructing a stereographic projection of the complex plane [32]. Linear polarization states lie on the equator, while circularly polarized state corresponds to the points on the poles. Due to this connection, the three last components of the normalized Stokes vector $\hat{\mathbf{s}} = \mathbf{S}/|\mathbf{S}|$ correspond to the coordinates of a point on the surface of the sphere when the light is fully polarized. In contrast to the elliptical representation, partially polarized light is portrayed as a point inside the sphere, where the DOP gives the distance from the origin.

1.1.2 Vectorial optical fields

In recent decades, remarkable phenomena have been revealed when beams with tailored complex amplitude and different polarization states interfere [33]. For the sake of simplicity, let us restrict to the case where two beams with tailored amplitudes, $\mathbf{E_1}(\mathbf{r})$ and $\mathbf{E_2}(\mathbf{r})$, with mutually orthogonal polarization states are superimposed. As shown in Figure 1.3-a, the resultant beam's intensity is simply the linear combination of the intensities of each polarization component. Nevertheless, the local polarization state varies from point to point on the transverse plane. Notably, the nonuniform spatial distribution of polarization states leads to the generation of new kinds of singularities [3]. The polarization singularities are typically understood as regions in the transverse plane in which a parameter of the polarization ellipse becomes undefined [12]. The first case corresponds to isolated locations where the major axis' inclination of the polarization ellipse becomes singular, called C-points. In other words, they are the points on the transverse plane with purely circularly polarized light. In a similar fashion, it is possible to identify linear polarization states as polarization singularities. In this case, the handedness of the polarization ellipse is undefined. Therefore, it is expected to find these singular states on lines, named L-lines, that separate regions with opposite handedness [3].

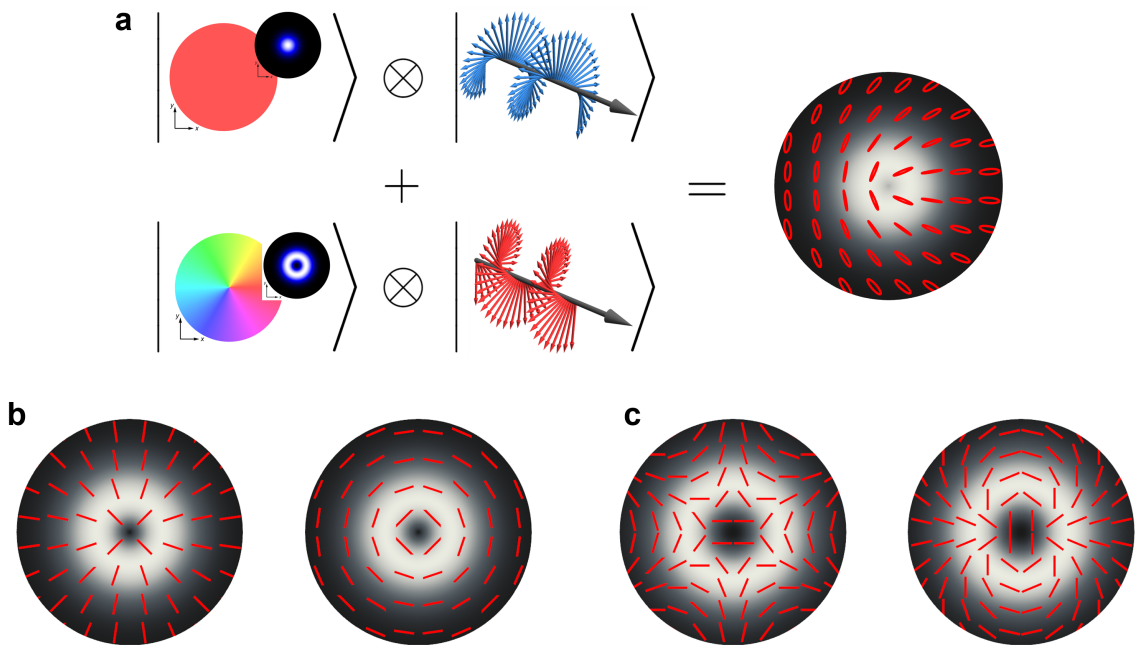

Figure 1.3: **Examples of vectorial fields a.** Vector beams can be obtained by the coherent superposition of scalar LG modes with different polarization states. Here, it is possible to observe a C-point at the origin, and L-line encloses it. **b.** Spatially-variant polarization distribution of a beam with a radial and azimutal vector beams.

Arguably, the most well-studied family of polarization-structured fields, also known as vectorial light fields, is those whose intensity exhibits cylindrical symmetry [34, 35]. While the cylindrical vector (CV) beams possess a single-ringed intensity pattern, similar to an LG mode, their spatially-varying polarization distribution is composed exclusively of linear polarization states, whose local orientation changes azimuthally (See Figure 1.3-b). More intricate polarization patterns with multiple L-lines, similar to flowers and spiderwebs, are obtained considering higher-order vector fields [36]. It should be noted that all polarization states contained in a CVB correspond to the points located at the equator of the Poincaré sphere [37]. The applications for CV beams are vast, spanning from optical manipulation [38–40] to communications [41]. In particular, radially polarized beams have proven useful for manufacturing due to the narrower intensity spot obtained by tight focusing them [42].

In contrast to the CV beams, it is possible to define another relevant set of vector beams that features every possible polarization, virtually covering the entire Poincaré sphere. Depending on their construction, full Poincaré beams may exhibit different types of

polarization dislocations characterized by a topological index that depends on the number of L-lines exiting the C-point and the direction in which the handedness of the local polarization states changes.

Chapter 2

Carving reliefs using spatially varying beams

This chapter is based on the following manuscript:

1. **M. F. Ferrer-García**, Y.Alvandi, Y. Zhang and E.Karimi, "Theoretical analysis on spatially structured beam induced mass transport in azo-polymer films", *Optics Express* **28**, 19954-19965 (2020) DOI: https://doi.org/10.1364/OE.395054

In the past decades, the use of structured light has revolutionized the field of optical manipulation. In this chapter, we present a detailed theoretical analysis of the optically induced forces exerted on an absorptive-scatter medium when they are exposed to structured beams. In particular, we analyze the effects of the different types of polarization topologies on the different components of the optical forces. In addition, we extend our calculations to nonparaxial monochromatic fields obtained by means of tightly focusing different vector vortex beams. The formalism used to describe focused fields due to a lens with a high numerical aperture is provided in Section 2.1. The numerical implementation used in this work can be found in Appendix A. We believe the results of this work would be useful to engineer more complicated landscapes on the surface of azo-benzene materials.

2.1 Focused Fields

Heretofore, the electric field has been described as a superposition of fully polarized solutions to the paraxial equation. However, the condition for paraxiality does not hold on

particular scenarios, such as focusing an optical beam using a lens with a high numerical aperture (NA), i.e., a microscope objective. Under these conditions, it is indispensable to consider the vector nature of light to give a correct description of the fields at the focal volume. For pedagogical purposes, let us consider as input to our imaging system a uniformly polarized monochromatic electric field whose wavevector $\mathbf{k}$ is always orthogonal to the entrance pupil's plane. It is reasonable to assume that every $\mathbf{k}$ points towards the focus after going through an ideal lens. As shown in figure 2.1-a it is possible to identify a spherical surface $\mathcal{S}$ with radius f centered on the focal point where every incoming geometrical ray meets its counterpart on the image space.

Formally, the electric field on the image space $\mathbf{E}(\mathbf{r})$ can be calculated from its angular spectrum representation [43]

$$\mathbf{E}(x,y,z) = -\frac{i}{2\pi}\iint_{\Omega}\frac{\mathbf{A}(k_x/k,k_y/k)}{k_z}e^{ik\Phi(k_x/k,k_y/k)}e^{i(k_x x+k_y y\pm k_z z)}\mathrm{d}k_x\mathrm{d}k_y, \tag{2.1}$$

where $k = 2\pi/\lambda$ is the corresponding wavenumber, $\Omega = (k_x^2 + k_y^2) \leq k^2$ is the solid angle formed by all the $\mathbf{k}$-vectors associated with the geometrical rays that reach the image space through the exit pupil and $\Phi(k_x/k, k_y/k)$ stands for the wave aberration function from the ideal spherical wave. Here, the strength factor $\mathbf{A}(k_x, k_y) = \mathbf{T}\ \mathbf{E_{in}}(k_x, k_y)$ defines the transformation of the input beam after going through reference sphere $\mathcal{S}$.

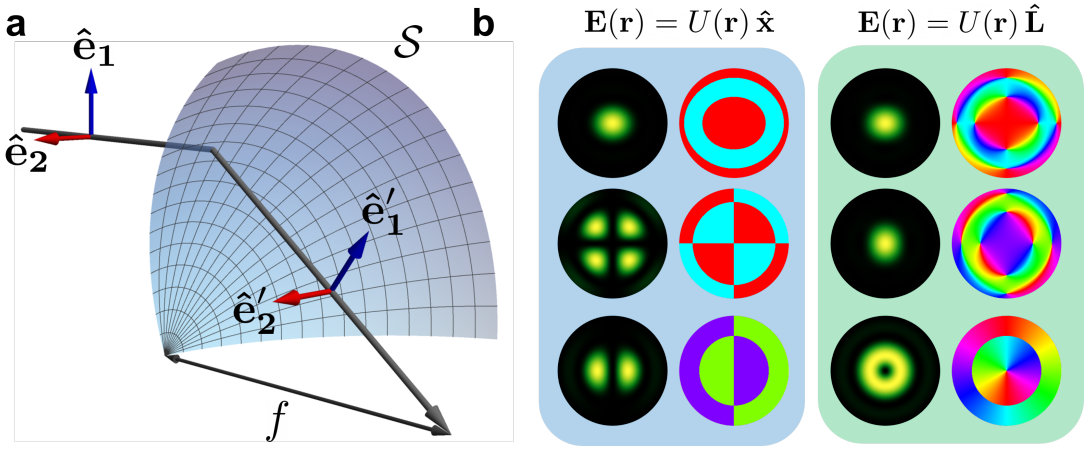

Figure 2.1: **Tight focusing of optical beams: a.** Schematic diagram of the coordinate system transformation occurring at the reference sphere $\mathcal{S}$. **b.** Amplitude and phase distributions of the electric field components are obtained by tightly focusing an $\mathrm{LG}_{0,0}$ mode for different input polarization states: the one on the right corresponds to a linearly polarized, while the left one is given by left-handed circularly polarized beam.

To determine the transformation $\mathbf{T}$, we must describe the refraction of the incident beam. Figure 2.1-a illustrates the polarization vector before and after crossing the reference sphere. Notice that $\mathcal{S}$ defines a transformation between a cylindrical coordinate system into a spherical coordinate system. Therefore, it is convenient to decompose the incident electric field vector into radial and azimuthal components. Notice that while the azimuthal contribution of the field remains unchanged in the image space, the radial component transforms into a polar component. Explicitly, we can write

$$\mathbf{T} = \sqrt{\cos\theta}\begin{bmatrix} \cos\theta\cos^2\phi + \sin^2\phi & (\cos\theta - 1)\sin\phi\cos\phi & \sin\theta\cos\phi \\ (\cos\theta - 1)\sin\phi\cos\phi & \cos\theta\sin^2\phi + \cos^2\phi & \sin\theta\sin\phi \\ -\sin\theta\cos\phi & -\sin\theta\sin\phi & \cos\theta \end{bmatrix}, \tag{2.2}$$

where θ and ϕ corresponds to the spherical coordinates. The factor $\sqrt{\cos\theta}$ is obtained by imposing energy conservation considerations during the process. For the case of an aplanatic system with a high numerical aperture, the electric field in the focal volume can be calculated using the Richards and Wolf [44] integral,

$$\mathbf{E}_f(\rho,\varphi,z) = -\frac{ifk}{2\pi}\, e^{-ikf} \int_0^{\alpha}\int_0^{2\pi} \mathbf{T}\mathbf{E}_{\mathbf{in}}(\theta,\phi) e^{ikz\cos\theta + \rho\sin\theta\cos(\phi-\varphi)} \sin\theta \; \mathrm{d}\phi\mathrm{d}\theta, \tag{2.3}$$

where $\alpha = \arcsin(\mathrm{NA}/n)$, NA is the lens numerical aperture, and n is the refractive index of the medium in which the focusing occurs.

Due to our interest in using LG mode, here we concentrate our efforts on deriving expressions for calculating when they are tightly focused. An arbitrarily polarized Laguerre Gauss mode with radial index $p = 0$ at the plane $z = 0$ is described as,

$$\mathbf{E}_{\mathbf{in}}(\mathbf{r}) = \mathrm{LG}_{0,\ell}(r,\phi)\left(\cos\eta\,\hat{\mathbf{x}} + e^{i\chi}\sin\eta\,\hat{\mathbf{y}}\right) \tag{2.4}$$

where η and χ control the relative amplitude and phase between the Cartesian components of our beam's polarization. Let us assume that the incoming field fills the lens's input pupil completely. Then, the complex amplitude of the LG mode in terms of the spherical coordinates,

$$\mathrm{LG}(\theta,\phi) \propto \left[\frac{\sin\theta}{\sin\alpha}\right]^{|\ell|} \exp\left(-\frac{\sin^2\theta}{\sin^2\alpha}\right)\exp(i\ell\phi). \tag{2.5}$$

Since the complex amplitude has azimuthal symmetry, it is possible to perform the integrals over ϕ, by making use of the Jacobi-Anger expansion [45]

$$e^{iz\cos\varphi} = \sum_{n=-\infty}^{\infty} i^n J_n(z) e^{in\varphi}, \tag{2.6}$$

where $J_n(\cdot)$ is a Bessel function of the first kind of integer order n, and

$$\int_0^{2\pi} e^{i(n-m)\varphi} d\varphi = 2\pi\delta_{nm}, \tag{2.7}$$

Thus, the focal field for an arbitrarily polarized LG mode is given by

$$\mathbf{E}(\rho,\varphi,z) = \frac{\cos\eta}{2}\begin{bmatrix} 2I_1 + I_2 + I_3 \\ (I_2 - I_3)/i \\ 2\,(I_5 - I_4) \end{bmatrix} + \frac{e^{i\chi}\sin\eta}{2}\begin{bmatrix} (I_2 - I_3)/i \\ 2I_1 - I_2 - I_3 \\ 2i(I_4 + I_5) \end{bmatrix}, \tag{2.8}$$

where we have defined the integral expressions,

$$I_1 = -\frac{\pi i^{\ell+1} f}{\lambda} e^{i\ell\varphi} \int_0^{\alpha} G(\theta,z)\,(1+\cos\theta)\,\mathrm{J}_\ell(k\rho\sin\theta)\mathrm{d}\theta, \tag{2.9a}$$

$$I_2 = -\frac{\pi i^{\ell+1} f}{\lambda} e^{i(\ell+2)\varphi} \int_0^{\alpha} G(\theta,z)\,(1-\cos\theta)\,\mathrm{J}_{\ell+2}(k\rho\sin\theta)\mathrm{d}\theta, \tag{2.9b}$$

$$I_3 = -\frac{\pi i^{\ell+1} f}{\lambda} e^{i(\ell-2)\varphi} \int_0^{\alpha} G(\theta,z)\,(1-\cos\theta)\,\mathrm{J}_{\ell-2}(k\rho\sin\theta)\mathrm{d}\theta, \tag{2.9c}$$

$$I_4 = \frac{\pi i^{\ell} f}{\lambda} e^{i(\ell+1)\varphi} \int_0^{\alpha} G(\theta,z)\,\mathrm{J}_{\ell+1}(k\rho\sin\theta)\mathrm{d}\theta, \tag{2.9d}$$

$$I_5 = \frac{\pi i^{\ell} f}{\lambda} e^{i(\ell-1)\varphi} \int_0^{\alpha} G(\theta,z)\,\mathrm{J}_{\ell-1}(k\rho\sin\theta)\mathrm{d}\theta, \tag{2.9e}$$

and

$$G(\theta,z) = \sqrt{\cos\theta}\sin\theta\left[\frac{\sin\theta}{\sin\alpha}\right]^{|\ell|}\exp\left(-\frac{\sin^2\theta}{\sin^2\alpha}\right)\exp\left(ikz\cos\theta\right). \tag{2.10}$$

It should be noted that the integrals defined above do not have closed form solutions, and they must be evaluated numerically. As shown in Figure 2.1-b depicts the focal fields obtained when considering different polarization states for a Gaussian beam. Appendix A contains implementations in different programming languages to calculate focal fields.

Research Article | Vol. 28, No. 14 / 6 July 2020 / Optics Express 19954
Optics EXPRESS

Theoretical analysis on spatially structured beam induced mass transport in azo-polymer films

MANUEL F. FERRER-GARCIA,[1,4] YOUSEF ALVANDI,[1,2,4] YINGWEN ZHANG,[3] AND EBRAHIM KARIMI[1,2,3,*]

[1]Physics Department, University of Ottawa, Advanced Research Complex, 25 Templeton, Ottawa, ON K1N 6N5, Canada
[2]Department of Physics, Institute for Advanced Studies in Basic Sciences, Zanjan 45137-66731, Iran
[3]National Research Council of Canada, 100 Sussex Drive, Ottawa, ON K1A0R6, Canada
[4]These authors contributed equally to this work
[*]ekarimi@uottawa.ca

Abstract: The radiation force from paraxial beams possessing helical phase fronts causes twists on the surface of an azobenzene polymer sample, and leads to the formation of micro-scale structures. Here, we theoretically investigate the radiation force generated by spatially structured optical beams on a dispersive-absorptive substrate. We derive an analytical expression for the radiation force from spatially structured polarized beams, including, lemon, star, monstar and vector vortex beams in the paraxial regime. Finally, we extend our calculation for non-paraxial beams - optical beams under the tight-focusing regime - and simulate the transverse radiation forces numerically at the focal plane.

1. Introduction

Structured light - electromagnetic waves possessing well-engineered amplitude, polarization, and spatial modes - has received increasing interest during the last few decades [1,2]. For instance, beams carrying orbital angular momentum (OAM) have been used in optical microscopy (ranging from optical spanners to stimulated emission depletion microscopy) [3,4], telecommunications [5–8] and quantum information [9,10]. The interaction of structured light beams and their induced optical forces for beams, such as Bessel beams [11–13] Airy beams [13,14], Airy sheets [15] and Poincaré beams [16,17], have been widely explored with very promising results during the last decades. Very recently, the interaction between spatially structured optical beams and an a medium with complex electrical susceptibility has been studied at the quasi-continuous wave (CW), pico-, nano- and femtosecond regimes [18–22].

Among all the possible materials, azo-polymers - organic polymers containing azo functional groups - have recently attracted much attention from the scientific community due to the exhibited reversible photo-induced isomerization [23]. It has been shown that a photoinduced mass transport phenomena is triggered when an azo-polymer film is illuminated with light in the ultraviolet or visible wavelengths, leading to controlled deformations on the polymer film [24–27]. Such modifications of the surface relief has been proven to be wavefront-sensitive [28]. In particular, it has been shown that beams carrying optical angular momentum (spin and OAM) can induce mass-transport and produce nano-scale helical structures [29–32]. Nevertheless, since the isomeric transitions are reversible, this photoinduced writing can be erased by heating or irradiating the sample with incoherent light [33]. This photoresponsive property makes the azo-polymers highly suitable for multiple applications, such as reversible storage materials, holographic gratings and micro-scale machining [25,33–36]. A simple analytical approach for the photoinduced surface relief formation based on the macroscopic optical radiation force by a

#395054 https://doi.org/10.1364/OE.395054
Journal © 2020 Received 14 Apr 2020; revised 12 Jun 2020; accepted 16 Jun 2020; published 22 Jun 2020

Optics EXPRESS

continuous-wave vortex beam was used to explain the spiral shaped deformations formed in the azo-polymer film in paraxial approximation [31].

Here, we extend this analysis from vortex beams to space-varying polarized light beams. The induced-force density due to structured optical beams onto the surface of a dispersive-absorptive medium is calculated at both paraxial and non-paraxial regimes. First, we present the calculations for the coherent superposition of optical vortices having opposite polarization states, e.g. the Cylindrical (CV) Vector beams [37] and the Full-Poincaré (FP) beams (including lemon, star and monstar polarization topologies) [38]. We have allocated the optical properties of an arbitrary azo-polymer in our calculations. Later on, a numerical analysis for the non-paraxial case of tightly focused vector beams is provided. Due to the combination of the inhomogeneous polarization and phase distributions, we predict the possible formation of significantly more complex patterns on the azo-polymer.

2. Optical forces due to structured light

The time-averaged optical radiation force density $\mathbf{F}$, which arises from optically induced electric polarization in a dielectric material, is expressed as, [31]

$$\mathbf{F} = \langle \rho_p \mathbf{E} + \mathbf{j}_p \times \mathbf{B} \rangle, \tag{1}$$

where $\mathbf{E}$ and $\mathbf{B}$ are respectively the electric field and magnetic flux density, ρ_p is the polarization charge density, $\mathbf{j}_p$ is polarization current density, and $\langle \cdot \rangle$ stands for time-average. For an isotropic and homogeneous material, such as azo-polymers when they are illuminated with a low power source, the surface polarization charge density is equal to zero ($\rho_p = 0$), and the polarization current density (for a monochromatic beam) can be written as $\mathbf{j}_p = -i\omega\epsilon_0\chi\mathbf{E}$. Here, ϵ_0 is the dielectric constant in vacuum, ω is the angular frequency of the optical field, and $\chi = \chi_r + i\chi_i$ is the complex electric susceptibility of the material. Therefore, Eq. (1) can be expressed as,

$$\begin{aligned} \mathbf{F} &= \langle i\omega\epsilon_0\chi\mathbf{E} \times \mathbf{B} \rangle \\ &= \frac{\omega\epsilon_0}{2} \left[\chi_r \mathrm{Im}(\mathbf{E} \times \mathbf{B}^*) + \chi_i \mathrm{Re}(\mathbf{E} \times \mathbf{B}^*) \right]. \end{aligned} \tag{2}$$

Here, the first term that is proportional to χ_r is a scattering force, while the second term which is proportional to χ_i is related to the absorption. Note that for the sake of simplicity, we have considered monochromatic electric fields with frequency ω. Using the Maxwell-Faraday equation, which dictates the relationship between the magnetic density flux and the electric field, i.e. $\mathbf{B} = (-i/\omega)\boldsymbol{\nabla} \times \mathbf{E}$, Eq. (2) yields,

$$\mathbf{F} = \frac{\epsilon_0}{2} \left[-\chi_r \mathrm{Re}(\mathbf{E} \times \boldsymbol{\nabla} \times \mathbf{E}^*) + \chi_i \mathrm{Im}(\mathbf{E} \times \boldsymbol{\nabla} \times \mathbf{E}^*) \right], \tag{3}$$

in which the time-averaged optical radiation force is expressed in terms of just the electric field and properties of the materials. It should be noted that Eq. (3) is a general expression for the optical force when an arbitrary electromagnetic field (with electric field $\mathbf{E}$) illuminates an azo-polymer film. The complex electric susceptibility $\chi = \chi_r + i\chi_i$ can be obtained from the transmission spectrum and Kramers-Kronig relations [39].

For the specific case of structured light, we consider an electric field formed by the coherent superposition of two optical vortices having opposite circular polarization states, i.e.,

$$\mathbf{E} = \mathbf{E}_1 + \mathbf{E}_2 = \left[\cos\alpha \, \mathrm{LG}_{p_1}^{\ell_1}(r, \phi) \, \hat{\mathbf{e}}_\mathbf{R} + e^{i\delta} \, \sin\alpha \, \mathrm{LG}_{p_2}^{\ell_2}(r, \phi) \, \hat{\mathbf{e}}_\mathbf{L} \right] e^{ikz}, \tag{4}$$

where $\{\hat{\mathbf{e}}_\mathbf{R}, \hat{\mathbf{e}}_\mathbf{L}\}$ are unit vectors of the circular polarization basis, and $k = 2\pi/\lambda$ is the wavenumber. The relative amplitude and phase between both beams can be tuned by the parameters $\alpha \in [0, \pi/4]$

Optics EXPRESS

and $\delta \in [0, 2\pi]$, respectively. The normalized amplitude of the optical vortices in cylindrical coordinates (r, ϕ, z) at a given plane (plane of interaction, i.e. $z = 0$) is described by Laguerre-Gauss (LG) modes,

$$\mathrm{LG}_p^{\ell}(r,\phi) = \sqrt{\frac{2(p!)}{\pi(p+|\ell|)!}}\frac{1}{w_0}\left(\frac{\sqrt{2}r}{w_0}\right)^{|\ell|} L_p^{|\ell|}\left(\frac{2r^2}{w_0^2}\right)\exp\left(-\frac{r^2}{w_0^2}\right)e^{i\ell\phi}, \tag{5}$$

where w_0 is the waist of the Gaussian envelope at the plane $z = 0$, $L_p^{|\ell|}(.)$ is the generalized Laguerre polynomials with azimuthal and radial indices of ℓ and p, respectively. The field described by Eq. (4) allows us to produce spatially variant polarization patterns, which are characterized by the topological index of the polarization singularity η [40]. η, the polarization topological index, is the amount of rotation of the polarization ellipse in a closed path around a point of circular polarization divided by 2π, and its quantity for a continuous field is half-integer. It is easy to show that Eq. (3), the induced force density, can now be written as

$$\mathbf{F} = \frac{\epsilon_0}{2}\left[-\chi_r \mathrm{Re}\left(\sum_{i,j}^{2}\mathbf{E}_i \times \nabla \times \mathbf{E}_j^*\right) + \chi_i \mathrm{Im}\left(\sum_{i,j}^{2}\mathbf{E}_i \times \nabla \times \mathbf{E}_j^*\right)\right]. \tag{6}$$

The vector quantity in Eq. (6), i.e. $\mathbf{E}_i \times \nabla \times \mathbf{E}_j^*$, is given by,

$$\begin{aligned}\mathbf{E}_i \times \nabla \times \mathbf{E}_j^* =& \frac{a_i a_j\, e^{i\delta_{ij}}\,\mathrm{LG}_{p_i}^{\ell_i}(r,\phi)}{2} \\ &\times \left\{e^{-i\sigma_j\phi}\left[\frac{l_j}{r}\mathrm{LG}_{p_j}^{-\ell_j}(r,\phi) + \sigma_j\frac{\partial}{\partial r}\left(\mathrm{LG}_{p_j}^{-\ell_j}(r,\phi)\right)\right](-i\sigma_i\hat{\mathbf{x}} + \hat{\mathbf{y}})\right. \\ &\left. - ik\,\mathrm{LG}_{p_j}^{-\ell_j}(r,\phi)(\sigma_i\sigma_j + 1)\hat{\mathbf{z}}\right\},\end{aligned} \tag{7}$$

where $a_{i(j)}$ are superposition weights (i.e. $\cos\alpha$ and $\sin\alpha$), $\sigma_{i(j)} = \pm 1$ are the beams' helicities, and δ_{ij} is the relative phase between $\mathbf{E}_i$ and $\mathbf{E}_j$.

For simplicity we assume LG modes with zero radial index, i.e. $p = 0$. Intensity of these beams is characterized by a single-ring shape (e.g., see Fig. 1), and it is invariant under free-space propagation. The above expression for LG modes with $p = 0$ reads,

$$\begin{aligned}\mathbf{E}_i \times \nabla \times \mathbf{E}_j^* =& \frac{a_i a_j\, e^{i\delta_{ij}}\,\mathrm{LG}_0^{\ell_i}(r,\phi)\mathrm{LG}_0^{-\ell_j}(r,\phi)}{2} \\ &\times \left\{e^{-i\sigma_j\phi}\left[\frac{\ell_j + \sigma_j|\ell_j|}{r} - \frac{2\sigma_j r}{w_0^2}\right](-\sigma_i\hat{\mathbf{x}} + \hat{\mathbf{y}}) - ik(\sigma_i\sigma_j + 1)\hat{\mathbf{z}}\right\}.\end{aligned} \tag{8}$$

It should be noted that the optical radiation force density in the the transverse plane varies slowly upon propagation – this can be seen in Eq. (4), where the field varies slowly in z, i.e. paraxial approximation. The previous expression can be substituted in Eq. (6) to obtain an analytical expression for the force density. Numerical simulations are used to calculate the optical radiation forces exerted on an azo-polymer film substrate. In these simulations, we assume the incident beam carries low power (below <50 mW), and an optically linear substrate where $\chi_r \approx \chi_i$ are constant for a certain wavelength in the visible domain. As a first example, we consider the exerted force for the CV beams, which are recovered from Eq. (4), when one sets $\alpha = \pi/4$ and

Optics EXPRESS

$\ell_1 = -\ell_2 = \ell$ for non-zero ℓs, i.e.,

$$\mathbf{E}_{\mathrm{CV}} = \left(\frac{1}{\sqrt{2}} \mathrm{LG}_0^{\ell}(r,\phi)\, \hat{\mathbf{e}}_{\mathbf{R}} + \frac{e^{i\delta}}{\sqrt{2}} \mathrm{LG}_0^{-\ell}(r,\phi)\, \hat{\mathbf{e}}_{\mathbf{L}} \right) e^{ikz}. \tag{9}$$

The intensity of these beams is a doughnut shape with a space-varying linear polarization. The orientation of the linear polarization on the intensity ring changes azimuthally, and it possesses a topology with $|\ell|$-fold symmetry, here ($|\eta| = 1$). Intensity and polarization distributions for two classes of the CV beams are shown in Figs. 1 and 2 - see bottom row. The transverse optical force density for these two beams, using Eq. (3), is calculated and shown in the upper row of Figs. 1 and 2. It can be noted that the absorption-dependent contribution, of the force vanishes for every value of ℓ. Furthermore, it is evident that for the case of a radially polarized light, the optical force density only exists in the z-direction, as seen in the first column of Fig. 1 - the force density does not have transverse components. In particular, for the case of $\ell = 1$ as the value of δ reaches to π, the magnitude of the exerted force on the surface increases independently of the polymer's absorption. The magnitude of the optical radiation force vanishes in the presence of polarization dislocations, creating a $2|\ell - 1|$ petal-like pattern in Fig. 2. Variations in the relative phase between the beams induce a rotation on the local polarization ellipse, as it can be observed in Figs. 1 and 2. Moreover, for positive values of ℓ, the force lines point towards the vortex singularity, and this direction is inverted when the topological charge is negative. Following these results, it is evident that the use of CV beams in the formation of complicated landscapes on the surface of an azo-polymer film independently of the absorption coefficient is possible.

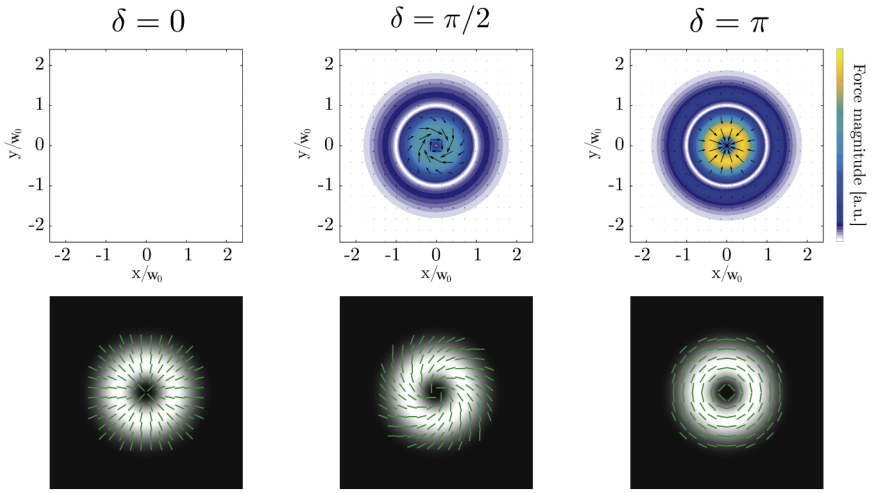

Fig. 1. Transverse optical radiation force density of a CV beam with $\ell = 1$ for $\delta = 0, \pi/2, \pi$. The colormap indicates the force magnitude, whereas the arrows indicate the force direction. The lower row shows the corresponding polarization distribution and intensity profile over the beam's transverse plane.

In a similar fashion, the induced optical radiation force is calculated for another set of space-varying polarized beams: Full-Poincaré (FP) beams [38]. In contrast with the CV beams, the polarization distribution of FP beams spans the entire surface of the Poincaré sphere while the beams' intensity is a quasi-uniform (flat-top) profile - see the first column of Fig. 3(a), (b), (c). Two possible types of polarization dislocations with non-integer η arise from Eq. (4): lemon and star topologies. However, a hybrid, nevertheless, independent topology, called monstar, can be

Optics EXPRESS

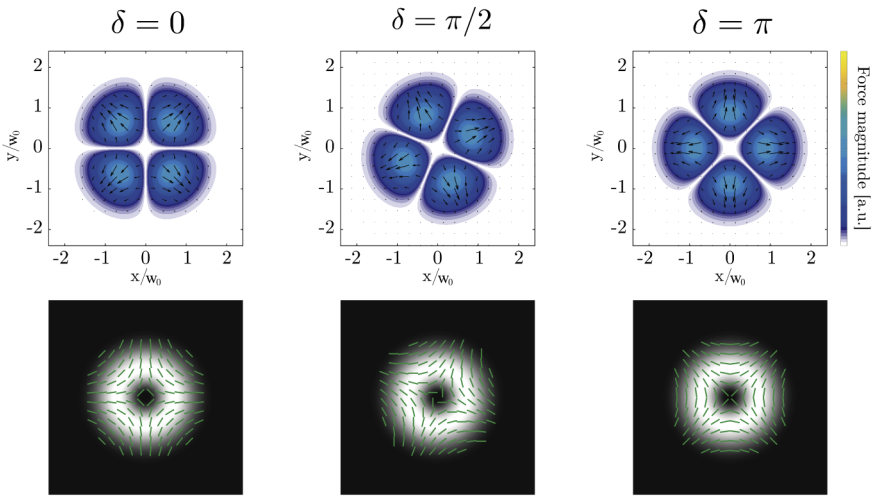

Fig. 2. Transverse optical radiation force density of a CV beam with $\ell = -1$ for various values of $\delta = 0, \pi/2, \pi$. The colormap indicates the force magnitude, whereas the arrows indicate the force direction. The lower row shows the corresponding polarization distribution over the intensity profile.

obtained when a third optical vortex is added to, Eq. (4) [41,42]

$$\mathbf{E}_{\mathrm{FP}} = \left\{\cos\alpha \left[\cos\beta\, \mathrm{LG}_0^{\ell_1}(r,\phi) - \sin\beta\, \mathrm{LG}_0^{-\ell_1}(r,\phi)\right] \hat{\mathbf{e}}_{\mathbf{R}} + e^{i\delta} \sin\alpha\, \mathrm{LG}_0^{\ell_2}(r,\phi)\, \hat{\mathbf{e}}_{\mathbf{L}}\right\} e^{ikz}, \quad (10)$$

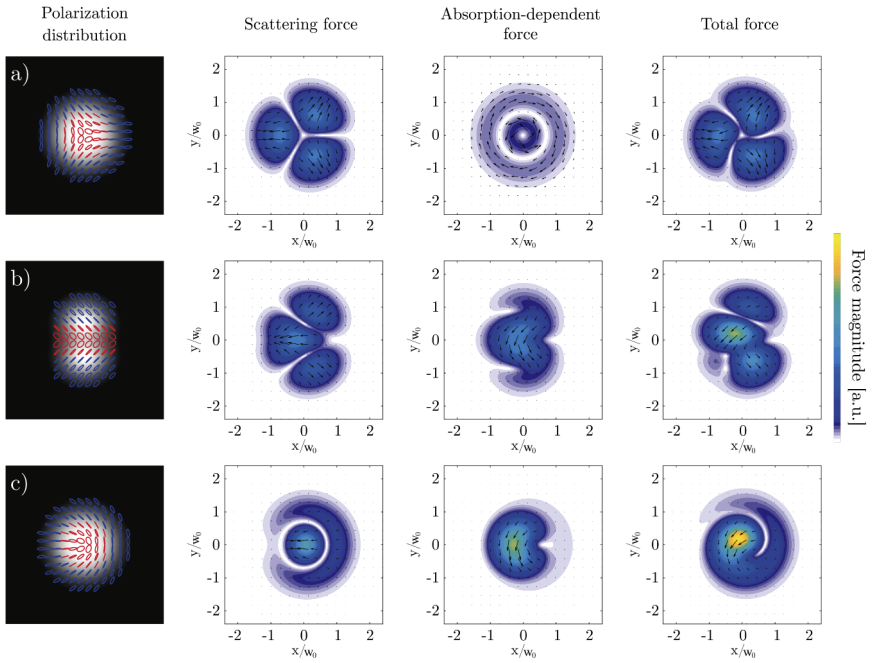

Fig. 3. Transverse optically induced force density of FP beams for (a) star ($\beta = 0$), (b) monstar ($\beta = \pi/4$), and (c) lemon ($\beta = \pi/2$) polarization topologies. The colormap indicates the force magnitude, whereas the arrows indicate the force direction. The first column shows the corresponding polarization distribution over the intensity profile. The red and blue colors of the ellipses indicate their handedness, left- and right-handed, respectively.

Optics EXPRESS

where $\beta \in (0, \pi/2)$. Equation (8) is still valid and can be used to calculate the induced force density. As it is shown in Fig. 3, both the scattering and absorption-dependent force contributions exert an non-trivial effect on the surface relief of the azo-polymer. Notice that the absorption-dependent force density for the star topology is formed by two rings with opposite directions – the force is counterclockwise for inner ring and clockwise for the outer ring. In this case, the induced force contribution is significantly smaller than that exerted by the scattering part. However, this symmetry is broken for any other configuration. In fact, for the case of lemon topology, the contribution due to χ_i, i.e. the absorption force, overcomes the scattering forces.

3. Optical forces of tightly focused space-varying polarized beams

Heretofore, we have considered paraxial beams whose polarization distribution exclusively lies on a transverse plane. However, it is well-known that when optical beams undergo focusing by means of a high numerical aperture (NA) lens, i.e. tight-focusing regime, a longitudinal component of the beam arises [43]. Indeed, the beam wavefront is tilted, and thus the beam polarization (which is locally transverse) possesses a component along the beams propagation direction. Under these conditions, it has been shown that the non-paraxial polarization structure generates complex and exotic 3-dimensional polarization topologies, such as Möbius strips or ribbons [44,45]. As a result of the creation of this non-negligible longitudinal component in the electric field, the cylindrical symmetry of the vector beam's intensity is broken for most of the cases [46] – see Fig. 4(b). Therefore, we present an analysis of the optical force exerted by the space-varying polarized beams, namely those beams studied in the previous section, under tight-focusing regime.

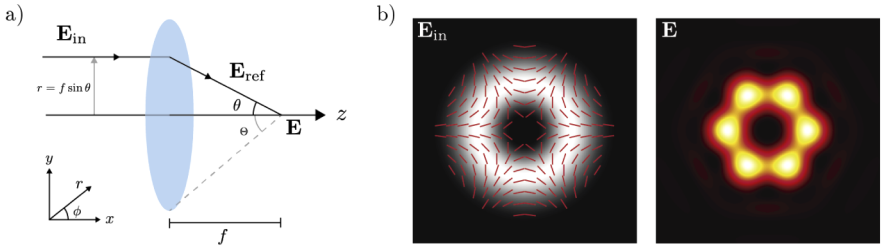

Fig. 4. Tight focusing of optical beams: (a) Schematic diagram of the coordinate system transformation used to calculate the tightly focused fields, (b) Input field and its corresponding focal field distribution intensity.

The electric field $\mathbf{E}_f(\rho, \varphi, z)$ at the focal plane of an aplanatic lens with focal length f, is given by Richards and Wolf's diffraction integral, [47]

$$\mathbf{E}_f(\rho, \varphi, z) = -\frac{ikf}{2\pi} e^{-ikf} \int_0^{2\pi} \int_0^{\Theta} \mathbf{E}_{\text{ref}}(\phi, \theta) e^{ikz\cos\theta + ik\rho\sin\theta\cos(\phi-\varphi)} \sin\theta \mathrm{d}\theta\, \mathrm{d}\phi, \tag{11}$$

where $\Theta = \arcsin(\text{NA}/n)$ is the maximum angular aperture of the objective, n is the refractive index of the medium, NA is the lens numerical aperture, and $\mathbf{E}_{\text{ref}}(\theta, \phi) = \mathbf{T}\,\mathbf{E}_{\text{in}}(\theta, \phi)$ is the transformation of the incident field $\mathbf{E}_{\text{in}}$ after the objective, see Fig. 4. The transformation matrix $\mathbf{T}$ for $\mathbf{E}_{\text{in}} = \left(E_x(\theta, \phi),\ E_y(\theta, \phi),\ 0\right)^{\text{T}}$ - ^{T} stands for transpose - is given by,

$$\mathbf{T} = \sqrt{\cos\theta} \begin{bmatrix} -\cos^2\phi\,\cos\theta + \sin^2\phi & -\cos\phi\sin\phi(\cos\theta + 1) & -\cos\phi\sin\theta \\ -\cos\phi\sin\phi(\cos\theta + 1) & \cos^2\phi - \sin^2\phi\,\cos\theta & -\sin\phi\sin\theta \\ \cos\phi\sin\theta & \sin\phi\sin\theta & -\cos\theta \end{bmatrix}. \tag{12}$$

Optics EXPRESS

Here, the input field $\mathbf{E}_{\text{in}}$ does not have a z-component; however, the transformation matrix $\mathbf{T}$ is given in its general form. It must be noted that despite $\mathbf{E}_{\text{in}}$ is a solution to the paraxial equation, $\mathbf{E}_{\text{f}}$ satisfies Maxwell's Equations. Since closed analytical solutions for Eq. (11) are hard or even impossible to obtain, the components of the electric field under tight focusing in air ($n = 1$) are calculated by numerical integration of Eq. (11) when the incident field is given by Eq. (4). In addition to the assumptions of the previous section, we consider a microscope objective with NA= 0.95 and the waist of the beam follows the relation $w_0 = f\,\text{NA}/n$ in order to fill completely the back of the microscope objective. Likewise, very short exposure times have been considered in order to avoid photo-bleaching, substrate degradation or damage due to the high-intensity irradiation.

In order to offer a more complete comparison between the paraxial and non-paraxial regimes, we have performed numerical calculations for the optical induced forces due to tightly focused Laguerre Gauss modes with radial index $p = 0$ and uniform polarization distribution. First, we present the results for an LG_0^0 mode with different polarization states on the Poincaré sphere. The results of numerical calculations are shown in Fig. 5. For a linearly polarized LG_0^0 beam, the induced force is associated to the real part of the electrical susceptibility, i.e. scattering force. The exerted force creates stretching-compressing effects on the surface of the azo-polymer film, whose direction depends on the inclination angle of the linear polarization state of the incident beam $\mathbf{E}_{\text{in}}$. A rotation is induced on the transverse optical radiation force density when

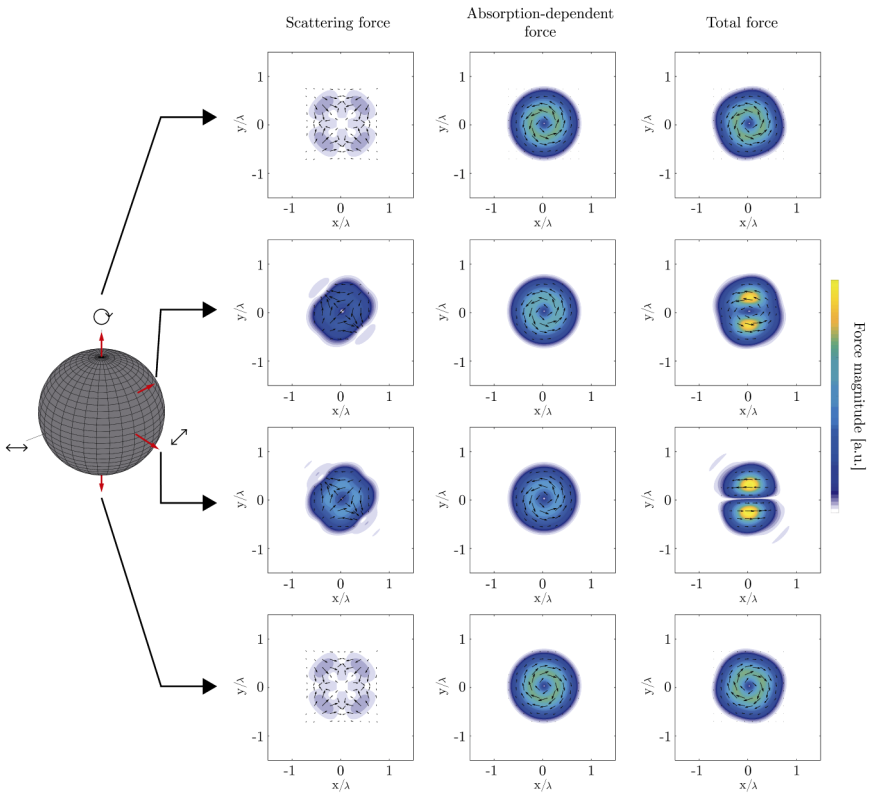

Fig. 5. Transverse optical radiation force density of a tightly focused LG_0^0 beam having different polarization states at the focal plane of an objective lens with numerical aperture of 0.95. The colormap indicates the force magnitude, whereas the arrows indicate the force direction.

Optics EXPRESS

the polarization state moves along different latitude lines of the Poincare sphere By changing the polarization state from linear to elliptical and then to circular - going from equator to poles - an absorption-dependent contribution that is pointing in the azimuthal direction appears. The direction of this force is directly related to the helicity of the polarization state. Moreover, the absorption-dependent force overcomes the scattering force for the case of purely circular polarization states.

Similarly, we numerically calculate the induced optical forces exerted due to a tightly focused LG_0^1, Laguerre Gauss mode with azimuthal index of +1, when it carries different uniform polarization states. The results of numerical calculations are shown in Fig. 6. In contrast to the previous case, i.e. induced force due to LG_0^0, an absorption-dependent component of the force in the azimuthal direction exists for the case of a uniform linear polarization. It must be noticed that, as in the case of a fundamental Gaussian beam, the absorption-dependent force overcomes the scattering component for the case of circular polarization. However, the optical radiation force density for both circular polarization states is different due to the generated spin-orbit coupling [48] during the tight focusing process. When the helicity and the topological charge of the optical vortex have the same sign, the direction of the force is uniform in the transverse plane. While, when the signs are opposite to each other, an inversion on the force's direction happens at a certain distance r from the beam axes.

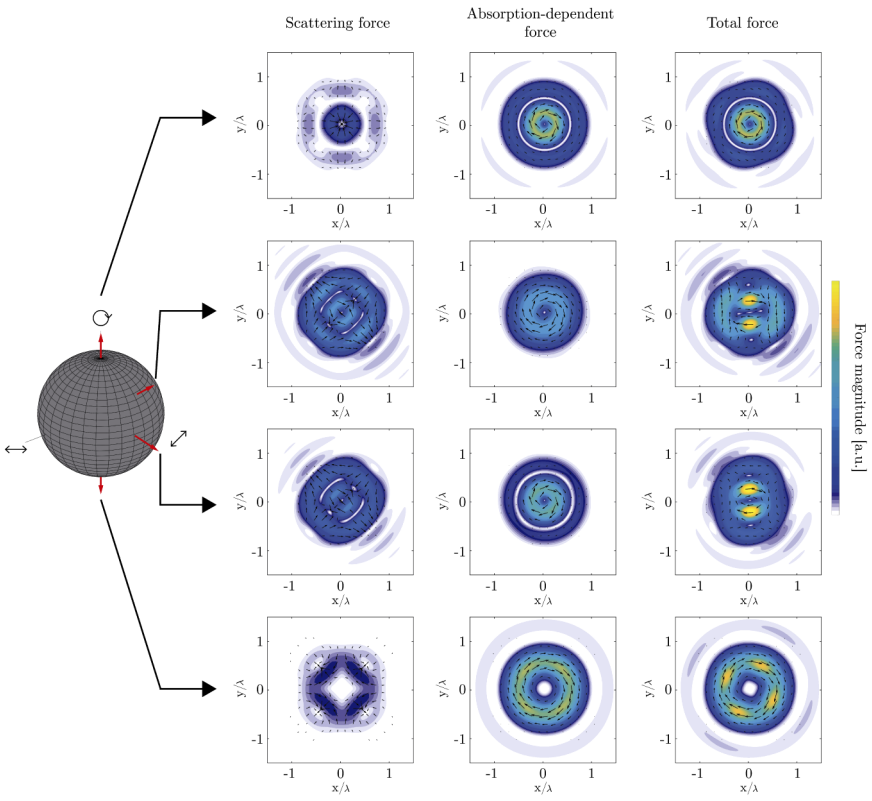

Fig. 6. Transverse optical radiation force density of a tightly focused LG_0^1 beam carrying different polarization states at the focal plane of an objective lens with numerical aperture of 0.95. The colormap indicates the force magnitude, whereas the arrows indicate the force direction.

Optics EXPRESS

As a next step, we calculate the induced force density for tightly focused CV beams. The results of numerical simulations are shown in Fig. 7 and Fig. 8 for CV beams with $\ell = 1$ and $\ell = -1$, respectively. As in the paraxial counterpart, see Fig. 1 and Fig. 2, the absorption-dependent contribution is zero for all values of δ. Note that as δ increases, the induced force density in the transverse plane experiences a counter-clockwise rotation of $\delta/2$, while the direction of the force varies according to δ. In particular, the optical radiation force density for $\ell_1 = -\ell_2 = 1$, if formed by two rings with opposite directions, leading to extrusion or compression of the azo-polymer film when $\delta = 0$ and $\delta = \pi$, respectively. During the transition ($0<\delta<\pi$), the material experiences a torsion, whose direction depends on the sign of δ. It must be noted that the force density of the CV beams exhibits the same type of symmetry as its corresponding intensity distribution.

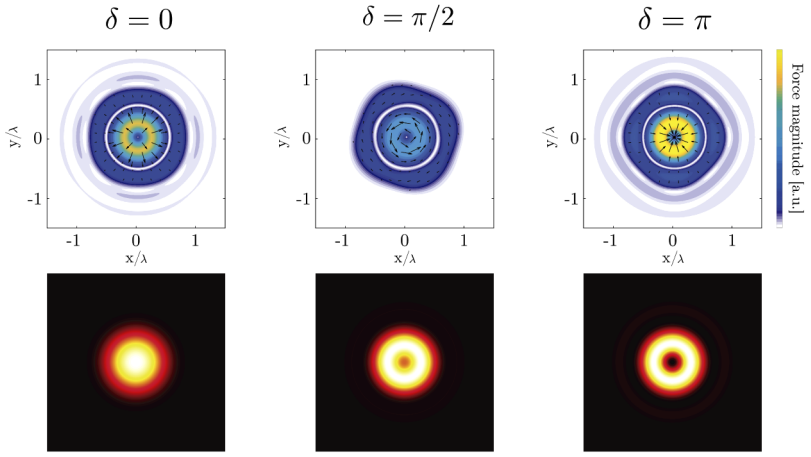

Fig. 7. Transverse optical radiation force density of a tightly focused CV beam with $\ell = 1$ for various values of $\delta = 0, \pi/2, \pi$ at the focal plane. The colormap indicates the force magnitude, whereas the arrows indicate the force direction. The lower row shows the corresponding intensity profile at the focal plane.

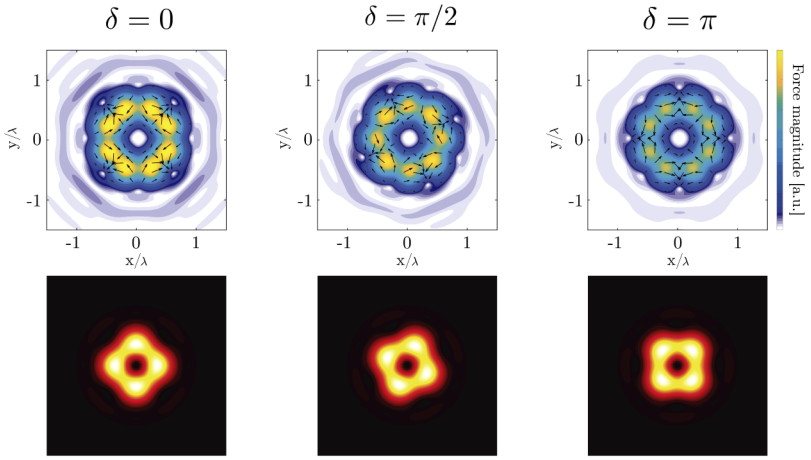

Fig. 8. Transverse optical radiation force density of a tightly focused CV beam with $\ell = -1$ for various values of $\delta = 0, \pi/2, \pi$ at the focal plane. The colormap indicates the force magnitude, whereas the arrows indicate the force direction. The lower row shows the corresponding intensity profile at the focal plane.

Optics EXPRESS

Finally, we completed our analysis by calculating the optically induced radiation force density for tightly focused FP beams, namely lemon and star beams. The results of numerical simulation are shown in Fig. 9. As in the case of the CV beams, the total force density preserves the symmetry exhibited by the intensity distribution of the field in the focal plane. The absorption-dependent force contribution for both cases of lemon and star topologies is formed by an as single ring, whose direction depends on the sign of η – the force is clockwise for the case of a lemon topology ($\eta = 1/2$) and counter-clockwise for the case of the star topology ($\eta = -1/2$). Notice that, for the case of the star topology, it is possible to identify four points (one is located at the centre and the other three are located around the beam centre) were the surface experiences torsion around a region of total null force.

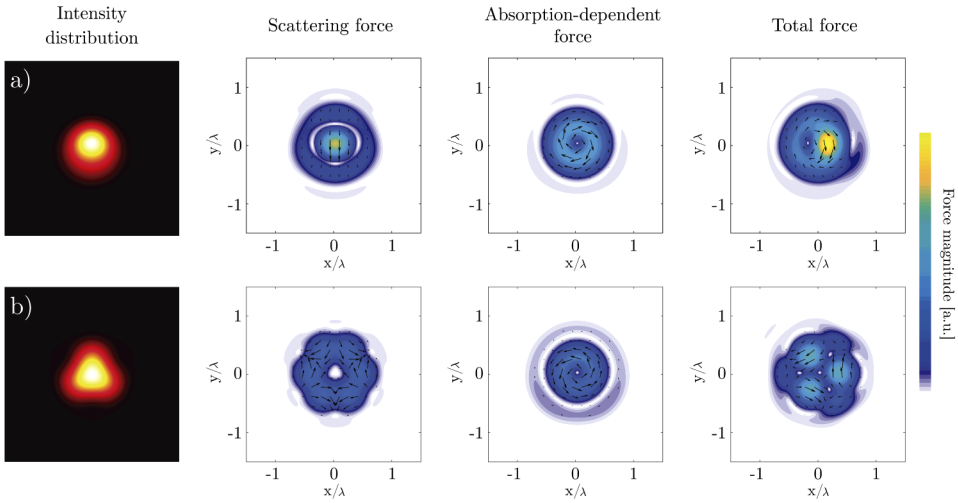

Fig. 9. Transverse optical radiation force density of a tightly FP beam for the a) lemon, and b) star polarization topologies at the focal plane. The colormap indicates the force magnitude, whereas the arrows indicate the force direction. The first column shows the corresponding the intensity profile on the focal plane.

4. Conclusion

We have theoretically derived an analytical expression for the optically induced force generated by the superposition of optical vortices possessing opposite circular polarization states in the paraxial regime on a surface of an absorptive-scatter medium. We have shown the optical radiation forces for space-varying polarized optical beams, and explored the effect of the inhomogeneous polarization distribution when the intensity profile is kept invariant. In particular, for the case of a cylindrical vector beam when $\ell = 1$, it is shown that the exerted torque on the azo-polymer can be varied independently of the value of χ_i. Moreover, we have studied the induced force for three types of Full-Poincaré beams, namely lemon, star and monstar topologies. Finally, the non-paraxial case of tightly focused spatially structured polarized beams was explored numerically. It is evident that the use of spatially-variant polarised beams in the generation of much more complicated landscapes on the surface of an azo-polymer film is possible. We believe this work will be of interest in the applications of nanostructuring of azo-benzene materials, and would be of interest for exploring physics of light-matter interaction in the linear regime.

Optics EXPRESS

Funding

Canada Research Chairs; Ontario Early Researcher Award (ERA); Natural Sciences and Engineering Research Council of Canada.

Acknowledgements

The authors would like to thank Alicia Sit and Hugo Larocque for fruitful discussions and thoughtful feedback. This work was supported by Canada Research Chairs (CRC), Ontario's Early Researcher Award (ERA), and Natural Sciences and Engineering Research Council (NSERC).

Disclosures

The authors declare that there are no conflicts of interest related to this article.

References

1. H. Rubinsztein-Dunlop, A. Forbes, M. V. Berry, M. R. Dennis, D. L. Andrews, M. Mansuripur, C. Denz, C. Alpmann, P. Banzer, T. Bauer, E. Karimi, L. Marrucci, M. Padgett, M. Ritsch-Marte, N. M. Litchinitser, N. P. Bigelow, C. Rosales-Guzmán, A. Belmonte, J. P. Torres, T. W. Neely, M. Baker, R. Gordon, A. B. Stilgoe, J. Romero, A. G. White, R. Fickler, A. E. Willner, G. Xie, B. McMorran, and A. M. Weiner, "Roadmap on structured light," J. Opt. **19**(1), 013001 (2017).
2. S. Franke-Arnold, L. Allen, and M. Padgett, "Advances in optical angular momentum," Laser Photonics Rev. **2**(4), 299–313 (2008).
3. R. Chen, K. Agarwal, C. J. Sheppard, and X. Chen, "Imaging using cylindrical vector beams in a high-numerical-aperture microscopy system," Opt. Lett. **38**(16), 3111–3114 (2013).
4. K. Zhanghao, X. Chen, W. Liu, M. Li, Y. Liu, Y. Wang, S. Luo, X. Wang, C. Shan, H. Xie, J. Gao, X. Chen, D. Jin, X. Li, Y. Zhang, Q. Dai, and P. Xi, "Super-resolution imaging of fluorescent dipoles via polarized structured illumination microscopy," Nat. Commun. **10**(1), 4694 (2019).
5. B. Ndagano, I. Nape, M. A. Cox, C. Rosales-Guzman, and A. Forbes, "Creation and detection of vector vortex modes for classical and quantum communication," J. Lightwave Technol. **36**(2), 292–301 (2017).
6. A. E. Willner, H. Huang, Y. Yan, Y. Ren, N. Ahmed, G. Xie, C. Bao, L. Li, Y. Cao, Z. Zhao, J. Wang, M. P. J. Lavery, M. Tur, S. Ramachandran, A. F. Molisch, N. Ashrafi, and S. Ashrafi, "Optical communications using orbital angular momentum beams," Adv. Opt. Photonics **7**(1), 66–106 (2015).
7. G. Gibson, J. Courtial, M. J. Padgett, M. Vasnetsov, V. Pas'ko, S. M. Barnett, and S. Franke-Arnold, "Free-space information transfer using light beams carrying orbital angular momentum," Opt. Express **12**(22), 5448–5456 (2004).
8. J. Wang, J.-Y. Yang, I. M. Fazal, N. Ahmed, Y. Yan, H. Huang, Y. Ren, Y. Yue, S. Dolinar, M. Tur, and A. E. Willner, "Terabit free-space data transmission employing orbital angular momentum multiplexing," Nat. Photonics **6**(7), 488–496 (2012).
9. F. Bouchard, A. Sit, F. Hufnagel, A. Abbas, Y. Zhang, K. Heshami, R. Fickler, C. Marquardt, G. Leuchs, R. W. Boyd, and E. Karimi, "Quantum cryptography with twisted photons through an outdoor underwater channel," Opt. Express **26**(17), 22563–22573 (2018).
10. M. Erhard, R. Fickler, M. Krenn, and A. Zeilinger, "Twisted photons: new quantum perspectives in high dimensions," Light: Sci. Appl. **7**(3), 17146 (2018).
11. V. Garcés-Chávez, D. McGloin, H. Melville, W. Sibbett, and K. Dholakia, "Simultaneous micromanipulation in multiple planes using a self-reconstructing light beam," Nature **419**(6903), 145–147 (2002).
12. F. G. Mitri, R. X. Li, L. X. Guo, and C. Y. Ding, "Optical tractor Bessel polarized beams," J. Quant. Spectrosc. Radiat. Transfer **187**, 97–115 (2017).
13. J. Baumgartl, M. Mazilu, and K. Dholakia, "Optically mediated particle clearing using Airy wavepackets," Nat. Photonics **2**(11), 675–678 (2008).
14. S. Zhang, J. Zhou, and Y.-X. Ren, "Ray optics analysis of optical forces on a microsphere in a (2 + 1)D Airy beam," OSA Continuum **2**(2), 378–388 (2019).
15. F. G. Mitri, "Pulling and spinning reversal of a subwavelength absorptive sphere in adjustable vector Airy light-sheets," Appl. Phys. Lett. **110**(18), 181112 (2017).
16. L. Wang, "Optical forces on submicron particles induced by full Poincaré beams," Opt. Express **20**(19), 20814–20826 (2012).
17. M. F. Ferrer-Garcia and D. Lopez-Mago, "Newtonian orbits of nanoparticles interacting with structured light beams," J. Opt. **21**(12), 125403 (2019).
18. M. Alameer, A. Jain, M. G. Rahimian, H. Larocque, P. B. Corkum, E. Karimi, and V. R. Bhardwaj, "Mapping complex polarization states of light on a solid," Opt. Lett. **43**(23), 5757–5760 (2018).

Optics EXPRESS

19. M. G. Rahimian, F. Bouchard, H. Al-Khazraji, E. Karimi, P. B. Corkum, and V. R. Bhardwaj, "Polarization dependent nanostructuring of silicon with femtosecond vortex pulse," APL Photonics **2**(8), 086104 (2017).
20. F. Takahashi, K. Miyamoto, H. Hidai, K. Yamane, R. Morita, and T. Omatsu, "Picosecond optical vortex pulse illumination forms a monocrystalline silicon needle," Sci. Rep. **6**(1), 21738 (2016).
21. F. Takahashi, S. Takizawa, H. Hidai, K. Miyamoto, R. Morita, and T. Omatsu, "Optical vortex pulse illumination to create chiral monocrystalline silicon nanostructures," Phys. Status Solidi A **213**(4), 1063–1068 (2016).
22. K. Toyoda, F. Takahashi, S. Takizawa, Y. Tokizane, K. Miyamoto, R. Morita, and T. Omatsu, "Transfer of light helicity to nanostructures," Phys. Rev. Lett. **110**(14), 143603 (2013).
23. X. Wang, *Azo Polymers: Synthesis, Functions and Applications*, Soft and Biological Matter (Springer-Verlag, 2017), 1st ed.
24. D. Kim, S. Tripathy, L. Li, and J. Kumar, "Laser-induced holographic surface relief gratings on nonlinear optical polymer films," Appl. Phys. Lett. **66**(10), 1166–1168 (1995).
25. P. Rochon, E. Batalla, and A. Natansohn, "Optically induced surface gratings on azoaromatic polymer films," Appl. Phys. Lett. **66**(2), 136–138 (1995).
26. S. Bian, J. M. Williams, D. Y. Kim, L. Li, S. Balasubramanian, J. Kumar, and S. Tripathy, "Photoinduced surface deformations on azobenzene polymer films," J. Appl. Phys. **86**(8), 4498–4508 (1999).
27. S. Bian, L. Li, J. Kumar, D. Kim, J. Williams, and S. Tripathy, "Single laser beam-induced surface deformation on azobenzene polymer films," Appl. Phys. Lett. **73**(13), 1817–1819 (1998).
28. M. Watabe, G. Juman, K. Miyamoto, and T. Omatsu, "Light induced conch-shaped relief in an azo-polymer film," Sci. Rep. **4**(1), 4281 (2015).
29. A. Ambrosio, L. Marrucci, F. Borbone, A. Roviello, and P. Maddalena, "Light-induced spiral mass transport in azo-polymer films under vortex-beam illumination," Nat. Commun. **3**(1), 989 (2012).
30. K. Masuda, R. Shinozaki, Y. Kinezuka, J. Lee, S. Ohno, S. Hashiyada, H. Okamoto, D. Sakai, K. Harada, K. Miyamoto, and T. Omatsu, "Nanoscale chiral surface relief of azo-polymers with nearfield oam light," Opt. Express **26**(17), 22197–22207 (2018).
31. D. Barada, G. Juman, I. Yoshida, K. Miyamoto, S. Kawata, S. Ohno, and T. Omatsu, "Constructive spin-orbital angular momentum coupling can twist materials to create spiral structures in optical vortex illumination," Appl. Phys. Lett. **108**(5), 051108 (2016).
32. Y. Nakata, M. Yoshida, and N. Miyanaga, "Parallel fabrication of spiral surface structures by interference pattern of circularly polarized beams," Sci. Rep. **8**(1), 13448 (2018).
33. S. Hvilsted, C. Sánchez, and R. Alcalá, "The volume holographic optical storage potential in azobenzene containing polymers," J. Mater. Chem. **19**(37), 6641–6648 (2009).
34. M.-S. Ho, A. Natansohn, C. Barrett, and P. Rochon, "Azo polymers for reversible optical storage. 8. the effect of polarity of the azobenzene groups," Can. J. Chem. **73**(11), 1773–1778 (1995).
35. M.-S. Ho, A. Natansohn, and P. Rochon, "Azo polymers for reversible optical storage. 9. copolymers containing two types of azobenzene side groups," Macromolecules **29**(1), 44–49 (1996).
36. S. L. Oscurato, M. Salvatore, F. Borbone, P. Maddalena, and A. Ambrosio, "Computer-generated holograms for complex surface reliefs on azopolymer films," Sci. Rep. **9**(1), 6775 (2019).
37. Q. Zhan, "Cylindrical vector beams: from mathematical concepts to applications," Adv. Opt. Photonics **1**(1), 1 (2009).
38. A. M. Beckley, T. G. Brown, and M. A. Alonso, "Full Poincaré beams," Opt. Express **18**(10), 10777–10785 (2010).
39. V. Lucarini, K.-E. Peiponen, J. J. Saarinen, and E. M. Vartiainen, *Kramers-Kronig Relations in Optical Materials Research*, Springer Series in Optical Sciences 110 (Springer-Verlag, 2005), 1st ed.
40. I. Freund, "Polarization singularity indices in Gaussian laser beams," Opt. Commun. **201**(4-6), 251–270 (2002).
41. J. F. Nye, *Natural focusing and fine structure of light: caustics and wave dislocations* (CRC, 1999).
42. B. Khajavi and E. J. Galvez, "High-order disclinations in space-variant polarization," J. Opt. **18**(8), 084003 (2016).
43. B. Richards, E. Wolf, and D. Gabor, "Electromagnetic diffraction in optical systems, ii. structure of the image field in an aplanatic system," Proc. R. Soc. Lond. A **253**(1274), 358–379 (1959).
44. T. Bauer, P. Banzer, E. Karimi, S. Orlov, A. Rubano, L. Marrucci, E. Santamato, R. W. Boyd, and G. Leuchs, "Observation of optical polarization Möbius strips," Science **347**(6225), 964–966 (2015).
45. T. Bauer, P. Banzer, F. Bouchard, S. Orlov, L. Marrucci, E. Santamato, R. W. Boyd, E. Karimi, and G. Leuchs, "Multi-twist polarization ribbon topologies in highly-confined optical fields multi-twist polarization ribbon topologies in highly-confined optical fields," New J. Phys. **21**(5), 053020 (2019).
46. E. Otte, K. Tekce, and C. Denz, "Tailored intensity landscapes by tight focusing of singular vector beams," Opt. Express **25**(17), 20194 (2017).
47. L. Novotny and B. Hecht, *Principles of nano-optics* (Cambridge University, 2012), 2nd ed.
48. K. Y. Bliokh, E. A. Ostrovskaya, M. A. Alonso, O. G. Rodríguez-Herrera, D. Lara, and C. Dainty, "Spin-to-orbital angular momentum conversion in focusing, scattering, and imaging systems," Opt. Express **19**(27), 26132–26149 (2011).

Chapter 3

Does the electric field knot or not?

This chapter is based on the following papers:

1. **M. F. Ferrer-García**, A. D'Errico, H. Larocque, A. Sit and E. Karimi, "Polychromatic electric field knots", *Physical Review Research* **3**, 033226 (2021). DOI: https://doi.org/10.1103/PhysRevResearch.3.033226

Despite the advances in frequency spectrum modification, the polarization states of polychromatic beams have been barely studied. Inspired by the seminal work of Issac Freund regarding the bichromatic fields [46], the authors propose a method to generate knotted polarization curves. Here, the tip of the local electric field vector is *tied* by tight focusing polychromatic structured light. The detection of these structures can be achieved by analyzing the scattering from metal nanoparticles [47] or interferometric methods [48]. The formalism that describes the polychromatic focused fields is given in Section 3.1. The numerical implementation used in this work is provided in Appendix A.

3.1 Focusing polychromatic fields

Despite the typical assumption in structured light, most light sources are not strictly monochromatic. In recent years, advances in laser technology have allowed the generation and manipulation of intense pulses of light, lasting from nanoseconds to femtoseconds. The generation of these optical pulses arises from phase-matching various broadband spectral components by means of optical resonators [49] or interferometric methods [50, 51]. In

contrast to the typical continuous laser sources, it is almost impossible to separate the temporal and spatial components of an optical pulse since they interact with each other during propagation [52, 53]. To deal with the challenges in modeling the evolution of these spatiotemporal fields, it is convenient employing the angular spectrum representation of the electric field. In general, the polychromatic electric field in vacuum is given by

$$\mathbf{E}(\mathbf{r},t) = \int_{-\infty}^{\infty} \tilde{\mathbf{E}}(\mathbf{r},\omega) e^{-i\omega t} \mathrm{d}t, \tag{3.1}$$

where ω is the angular frequency and $\tilde{\mathbf{E}}(\mathbf{r},\omega)$ is the electric field of a single spectral component [54]. The angular representation allows us to write,

$$\tilde{\mathbf{E}}(\mathbf{r},\omega) = g(\omega)\tilde{\mathbf{U}}(\mathbf{r}), \tag{3.2}$$

where $g(\omega)$ is the spectral density and $\tilde{\mathbf{U}}(\mathbf{r})$ are frequency domain spatial distribution of the polychromatic field. As shown in fig. 3.1, we can expand the spectrum profile of the beam in a set of orthogonal functions, leading to the concept of temporal modes [55, 56]. The manipulation of these temporal modes opened a new unexplored degree of freedom for engineering more complicated fields.

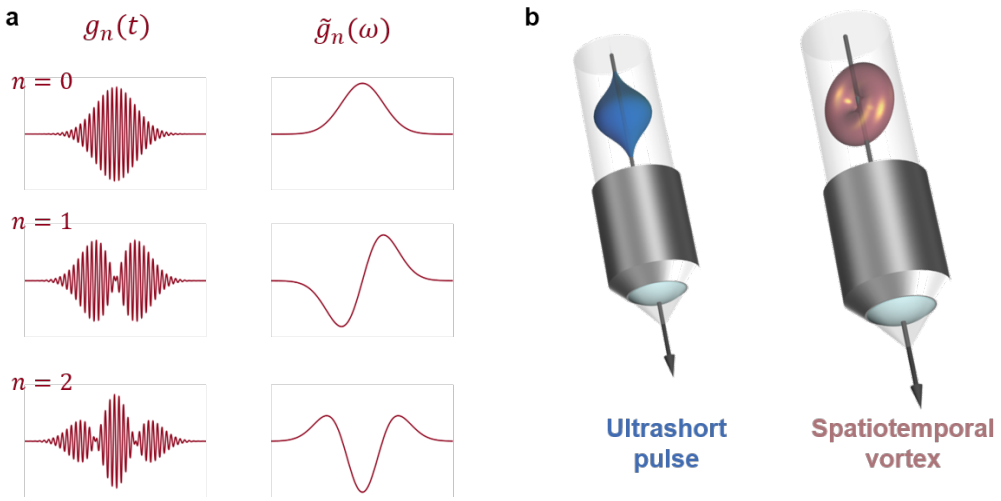

Figure 3.1: **Spatiotemporal modes a.** Example of an orthogonal basis used to describe temporal modes. The left and right columns depict schematics of the temporal pulses and their corresponding spectral densities, respectively. **b.** Different spatiotemporal structures.

Spatiotemporal optical vortices (STOV) arise from shaping the temporal distribution of an optical vortex [57, 58], such as the ones described in the previous chapter. In contrast to traditional optical vortices, the orbital angular momentum of a STOV is not only longitudinal, but it possesses a transverse component [59]. Nevertheless, technological advances allowed the generation of more exotic wave packets such as elusive toroidal electromagnetic rings [60, 61] or complex fields that simulate the behavior of topological quasiparticles [62]. Due to their properties, it is not surprising that the diffraction and propagation of temporally tailored fields, such as ultra-short pulses or STOVs, have been the subject of interest for many years [52, 63, 64]. Particularly, the study of the behavior after undergoing thorough focusing has received a considerable amount of attention due to the increase in the instant power at the focus [65]. It has been shown that few-cycle pulses experience limited diffraction when using specific microscope objectives [66]. The manipulation of the spatiotemporal structure can induce effects on the spectrum, deformation on the wavefront, and shift the location of the intensity peak on the focal volume [67–69]. Meanwhile, intricate generation of spatiotemporal phase singularities due to spin-orbit coupling has been observed when STOVs are tightly focused by a high numerical aperture lens [70, 71].

The expression for the electric field vector of a single spectral component near the focus of an aplanatic system can be obtained by substituting Eq. (3.2) into the Richards-Wolf diffraction integral in Eq. (2.3). Thus, it can be written,

$$\tilde{\mathbf{E}}_f(\rho,\varphi,z,\omega) = -\frac{if\omega}{2\pi c}g(\omega)\int_0^{\alpha}\sin\theta\,\mathrm{d}\theta\,e^{ikz\cos\theta}\int_0^{2\pi}\mathbf{A}(\phi,\theta)e^{ik\rho\sin\theta\cos(\varphi-\phi)}\,\mathrm{d}\phi, \tag{3.3}$$

where the time-dependent focal field can be obtained from Eq. (3.1).

3.2 Brief introduction to Knot Theory

Among the plethora of topics in three-dimensional topological elements, links and knots stand out due to their simplicity: one can take a rope or a piece of paracord and start "experimenting" with these topological objects. While knots and links have been present as motifs and symbols for a long time, it was Carl Friedrich Gauss who decided first that they were more than just a mere curiosity. Despite never providing formal proof, he introduced the concept of linking numbers, i.e., the total number of crossings of a knot, and its calculation would be the result of a simple integral [72]. The first use of knots in physics can be attributed to the joint work of Lord Kelvin and Peter G. Tait. After learning about

the stability of smoke vortex rings propagation in air, they proposed that atoms could be understood as vortexes in the aether [73]. While their theory was proven to be incorrect, the interest in knots and links to explain physical phenomena has grown since then. In the last decades, low-dimensional elements found applications in a wide range of fields in physics: describing the tangles in DNA chains [74], determining the chirality of chemical compounds [75], calculating expectation values for some quantum gravity models [76], explaining entaglement [77], among others.

3.2.1 Knots and Links

More formally, classical knots can be defined as non-self-intersecting closed curves embedded in three dimensions. Under this definition, the simplest knot is an untangled curve known as the trivial knot or unknot. Typically, knots are depicted using planar diagrams, i.e., particular projections onto a 2-dimensional space. These projections follow two basic rules: no more than two points can be superposed and must correspond to crossings or vertexes. On the diagram, an undercrossing line is indicated by the deletion of a segment, see Figure 3.2-a.

Two knots are equivalent if and only if there is a smooth continuous deformation that takes one knot to the other. Here, a *smooth* deformation implies that the curve can not self-intersect at any point of the deformation process [23], e.g., any nontrivial knot cannot be deformed into an unknot without the curve crossing itself at least once. In fact, Reidermeister proved that all knot deformations can be summarized into a sequence of three moves that correspond to ambient isotopy [78], as shown in Fig. 3.2-b. However, identifying the type of knot when given an arbitrary curve is an open question for the knot theorists [79]. To do so, mathematicians have developed the concept of a *topological invariant*. An invariant is a function that takes a set of knots and returns another object (integers, polynomials, groups, etc). An equivalent class of knots holds the invariant value [80]. In the context of distinguishing knots, we should introduce the work of James Waddell Alexander II as the first polynomial invariant, posteriorly extended by John Conway. In this case, the knot invariant constructs and assigns a polynomial with integer coefficients to different types of knots using a skein relation [81]. However, Alexander's polynomial fails to differentiate the chirality of a knot: a knot K and its mirror image K^* hold the same value. In 1984, a new invariant, heavily inspired by the algebra of braid groups, was introduced: the Jones polynomial. In contrast to the former invariant, the Jones polynomial fails to identify the type of knot uniquely, but it can distinguish the handedness of an oriented knot [80].

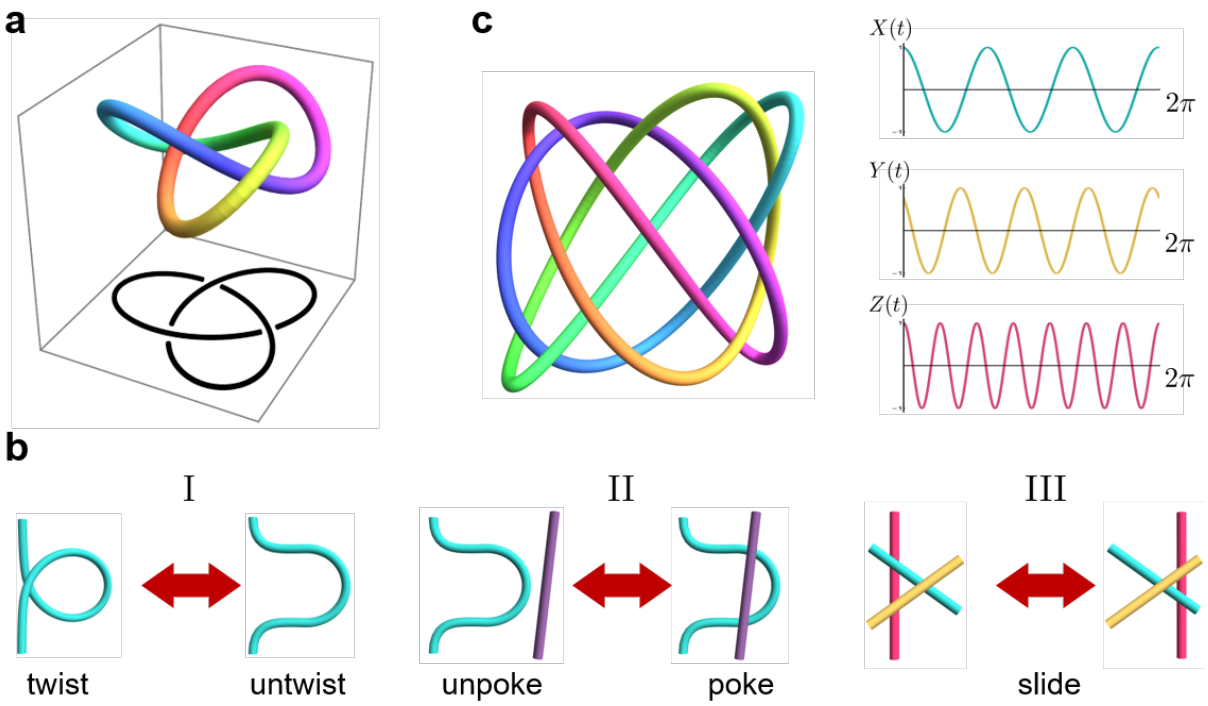

Figure 3.2: **Knots and their concept.** **a.** A trefoil knot and one of its corresponding planar representations. **b.** Schematics of the Redeimeister moves. It is possible to show that any link deformation can be decomposed into these local moves. **c.** Example of a Fourier knot and its decomposition in commensurable frequencies. A Fourier-(1,1,1) knot, as the one depicted here, is also called Lissajous Knot.

While knots can be represented by line segments intersecting at their endpoints [23], we focus our interest on the smooth continuous curves. In general, any curve in $\mathbb{R}^3$ can be constructed by a set of parametric equations $\mathcal{C}(t) = [X(t), Y(t), Z(t)]$, where x, y, z are smooth functions of a parameter t. In the context of knots and links, we are interested in the case the curve is periodic such that $\mathcal{C}(t) = \mathcal{C}(t + \tau)$, τ is the period. As a first approach, we have the case of knots generated by following trajectories on the surface of a torus [23]. A more interesting case occurs by recalling that any periodic smooth functions can be expressed by a Fourier series [45]. Therefore, each x, y, z can be expressed as a finite

series,

$$X(t) = \sum_{i=1}^{N_i} A_i^{(x)} \cos\Big(m_i^{(x)} t + \phi_i^{(x)}\Big), \tag{3.4a}$$

$$Y(t) = \sum_{j=1}^{N_j} A_j^{(y)} \cos\Big(m_j^{(x)} t + \phi_j^{(x)}\Big), \tag{3.4b}$$

$$Z(t) = \sum_{k=1}^{N_k} A_k^{(z)} \cos\Big(m_k^{(x)} t + \phi_k^{(x)}\Big), \tag{3.4c}$$

with i, j and k terms, respectively. Here $A_i^{(\cdot)}$, $m_i^{(x)}$ and $\phi_i^{(x)}$ are real numbers. A knot will be called a Fourier-(i, j, k) knot if it is described by an equation as given above (See Figure 3.2-c.

Polychromatic electric field knots

Manuel F. Ferrer-Garcia,[1,*] Alessio D'Errico,[1] Hugo Larocque,[2] Alicia Sit,[1] and Ebrahim Karimi[1,†]
[1]*Department of Physics, University of Ottawa, Advanced Research Complex, 25 Templeton, Ottawa, Ontario, Canada K1N 6N5*
[2]*Research Laboratory of Electronics, Department of Electrical Engineering and Computer Science, Massachusetts Institute of Technology, Cambridge, 02139 Massachusetts, USA*

(Received 6 April 2021; accepted 10 August 2021; published 8 September 2021)

The polarization of a monochromatic optical beam lies in a plane and, in general, is described by an ellipse, known as the polarization ellipse. The polarization ellipse in the tight-focusing (nonparaxial) regime forms nontrivial three-dimensional topologies, such as Möbius and ribbon strips as well as knots. The latter are formed when the dynamics of specifically structured polarization states are studied upon propagation. However, optical knots can also exist within another form: The electric field's tip can be made to locally oscillate along a knotted trajectory. We propose an intuitive technique to generate and engineer the path traced by the electric field vector of polychromatic beams to form different knots. In particular, we show examples of how tightly focused beams with at least three frequency components and different spatial modes can cause the tip of the electric field vector to follow, locally, a knotted trajectory. Our study may provide insight in designing current densities for structured polychromatic electromagnetic fields that interact with matter.

DOI: 10.1103/PhysRevResearch.3.033226

I. INTRODUCTION

The rapid advancements in the manipulation and control of electromagnetic radiation have allowed researchers to explore solutions of Maxwell's equations possessing rich topological features. The first structures that became the subject of extensive research were phase [1,2] and polarization singularities [3]. In particular, beams carrying a nonzero value of orbital angular momentum (OAM) [4] became of interest in many applications of classical and quantum optics. Optical beams with well-engineered spectra, polarization, and spatial and temporal structures are nowadays widely used in optical manipulation [5], microscopy [6–8], surface and material structuring [9], and classical and quantum communication [10,11]. Moreover, more complicated structures can be observed by analyzing an optical beam whose properties are not entirely defined within a two-dimensional plane, but within a three-dimensional volume. It is, indeed, predicted that the free-space trajectories of field dislocations can form closed loops [12,13] with nontrivial topologies, e.g., links and knots [14]. Recently, by exploiting the technology of spatial light modulators, beams exhibiting these features have been successfully engineered in the laboratory [13,15] and proposed as tools to encode prime numbers [16].

Advanced tools in nonlinear optics have improved our ability to structure the frequency spectrum of an electromagnetic field, with applications such as optical manipulation and atom trapping [17–20], along with the generation of structured electric currents in semiconductors [21]. Nevertheless, the polarization states of polychromatic fields have been barely studied. While in the monochromatic case the electric field vector describes an ellipse, more complicated curves occur when multiple waves with different temporal frequencies are superimposed. This new "zoo" of polarization states, as mentioned before, remains almost unexplored; the only accurately described cases are the ones in which two fields oscillate in the same plane. If the two frequencies follow the condition $\omega_2 = m\,\omega_1$, where m is a positive integer, the local electric field traces a quartic plane curve (Lissajous-like curves) [22].

In this paper, we aim to explore the behavior of structured polychromatic fields in the nonparaxial regime, where a non-negligible component of the electric field along the propagation direction is observed. Nonparaxial fields are typically obtained by tightly focusing paraxial beams with high numerical aperture (NA) lenses [23]. It has been previously shown that, under such conditions, polarization singularities in paraxial fields can be mapped to three-dimensional structures such as Möbius strips, twisted ribbons, and skyrmionic textures [24–27]. Recently, a general scheme has been proposed in which three-dimensional superpositions of plane waves with different frequencies can create an electric field wherein its tip locally traces a knotted curve [28]. Here, we adopt the methods developed in Ref. [28] in the context of focusing by aplanatic lenses. We explore different configurations in which the polarization structure of tightly focused polychromatic beams in the form of knotted polarization oscillations is generated by means of vector diffraction

*mferr010@uottawa.ca
†ekarimi@uottawa.ca

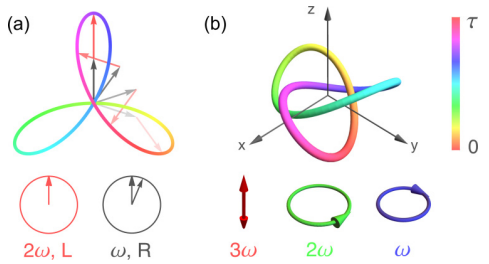

FIG. 1. (a) Paraxial polychromatic electric field (tip) tracing the planar quartic polarization curve $\mathcal{C}(t) = [\cos(t) + \sin(2t), -\sin(t) + \cos(2t), 0]$. Fundamental ($\omega$) and second-harmonic ($2\omega$) beams possess left- and right-handed polarization states, respectively. (b) Nonparaxial polychromatic electric field tracing the three-dimensional parametric curve $\mathcal{C}(t) = [\sin(3t), \cos(t) - 2\cos(2t), \sin(t) + 2\sin(2t)]$. The third harmonic ($3\omega$) is longitudinally polarized.

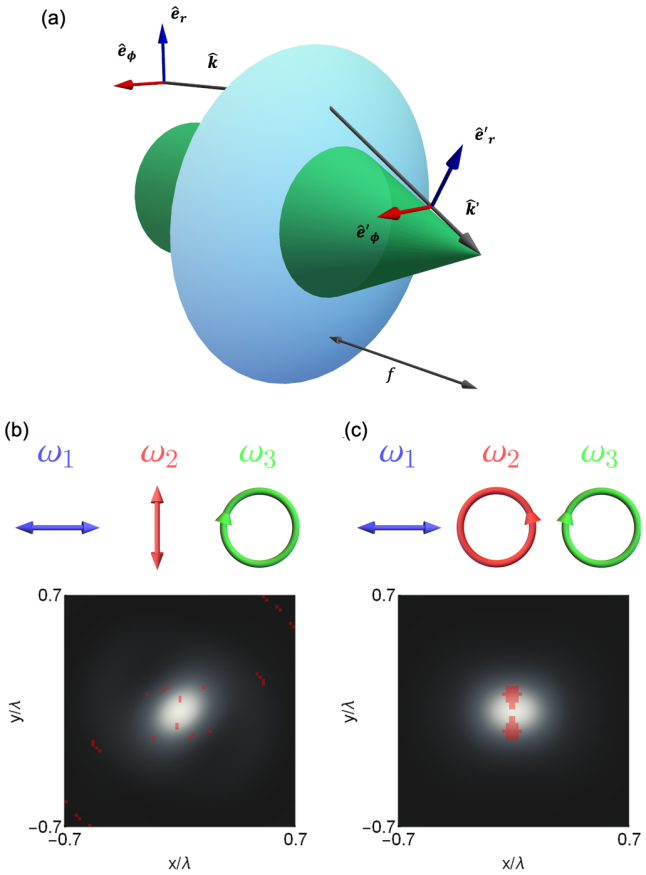

FIG. 2. (a) Schematic diagram of the coordinate system transformation used to calculate the tightly focused fields. (b) and (c) Spatial distribution of knotted polarization curves at the focal plane obtained by tightly focusing two cases of the field given by (3), superimposed with the total intensity for $\omega_2/\omega_1 = 2$ and $\omega_3/\omega_1 = 3$ while the relative amplitudes are $a_2/a_1 = a_3/a_1 = 2$. The red pins indicate the location of knotted polarization states. The corresponding polarization state for each frequency is shown above each panel.

of polychromatic beams through an aplanatic lens. Indeed, the knotted polarizations are ubiquitous once simple conditions on the different frequencies are imposed. We follow a heuristic approach to generate large populations of knotted polarizations in the focal plane, based on the knowledge of the tight focusing of vector vortex beams. In the provided examples, we localize and identify the knotted trajectories in different planes in the focal volume.

II. KNOTTED POLARIZATION CURVES

In this section we briefly outline the mathematical description of knotted curves traced by time-dependent vector fields. A more detailed treatment can be found in Ref. [28]. Let us start by considering a polychromatic electric field described by the superposition of N temporal Fourier components,

$$\mathbf{E}(\mathbf{r};t) = \sum_{n=1}^{N} \mathrm{Re}[\mathbf{A}_n(\mathbf{r})e^{-i\omega_n t}], \tag{1}$$

where $\{\omega_n\}$ is the set of optical frequencies, while $\mathbf{A}_n$ is the local complex amplitude. For each point in space, the tip of the electric field vector describes a closed three-dimensional curve $\mathcal{C}(t)$ for $t \in [0, 2\pi/\omega_p]$, where ω_p is the greatest common divisor of the set ω_n (see Fig. 1). In general, it is possible to construct a set of parametric equations such that $\mathcal{C}(t) = [X(t), Y(t), Z(t)]$, where $X(t)$, $Y(t)$, and $Z(t)$ are finite Fourier series with i, j, and k frequency components. The

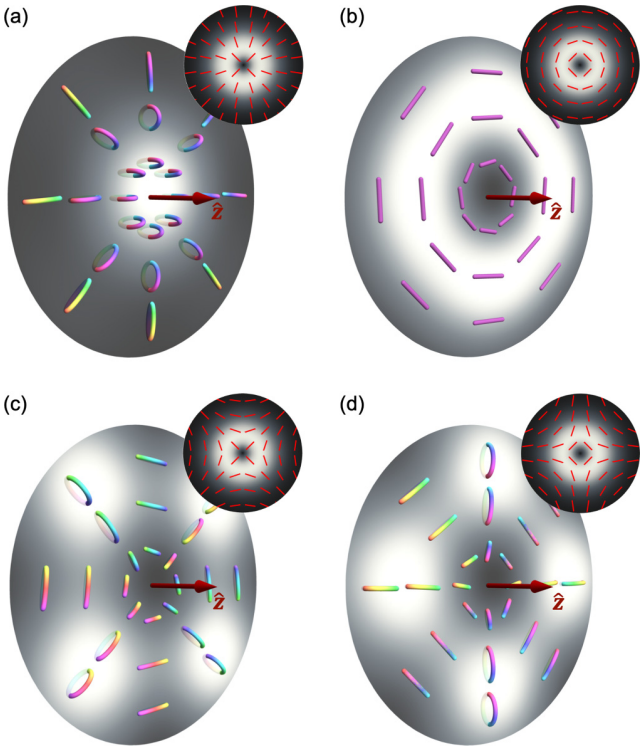

FIG. 3. Three-dimensional polarization distribution at the focal plane $z = 0$ for the tightly focused vector vortex beam: (a) $\mathbf{E}_\mathbf{v}(\mathbf{r};1,0)$, (b) $\mathbf{E}_\mathbf{v}(\mathbf{r};1,\pi)$, (c) $\mathbf{E}_\mathbf{v}(\mathbf{r};-1,0)$, and (d) $\mathbf{E}_\mathbf{v}(\mathbf{r};-1,\pi)$. Insets show the intensity and polarization distributions of the beams in the paraxial regime.

parametrized curve $\mathcal{C}(t)$ is defined as a Fourier-(i, j, k) knot [29]. These three-dimensional curves simplify to the well-known polarization ellipse for the case of monochromatic light ($N = 1$) and to the *Lissajous-like singularities* for the paraxial case, i.e., $Z(t) = 0$ [22]. Similarly, a nontrivial knot is defined as a curve that cannot be transformed through smooth deformations into a simple loop, also known as the *unknot*. Knots can thus be classified in terms of topological invariants, i.e., mathematical objects that label sets of curves which can be smoothly transformed into each other [30]. Any transition from one type of knot to another corresponds to passing through a self-intersecting curve. For the simplest case of a Fourier-(1,1,1) knot, the local electric field must have the form

$$\mathbf{e} = \sum_{m=1}^{3} \mathrm{Re}[a_m\, e^{-i\omega_m t}\, \hat{\mathbf{e}}_\mathbf{m}], \tag{2}$$

where $\{\hat{\mathbf{e}}_\mathbf{m}\}$ is the set of unit vectors that define a local orthogonal three-dimensional basis and $\{a_m\}$ are complex numbers related to the relative intensity and phase among the chromatic components. In addition, the frequencies $\{\omega_m\}$ must be proportional to three coprime numbers [30].

III. KNOTTING LIGHT BY TIGHT-FOCUSING STRUCTURED POLYCHROMATIC LIGHT

For paraxial beams, one can only create two-dimensional polarization curves (e.g., Lissajous figures); this is due to the electric field being confined in a plane orthogonal to the fixed propagation direction. However, knotted polarization curves can be achieved by interfering electric fields with different frequencies and different propagation directions; this creates the three oscillation directions needed for three-dimensional curves [28]. In contrast to direct interference, nonparaxiality can be achieved by tight focusing, where the desired dif-

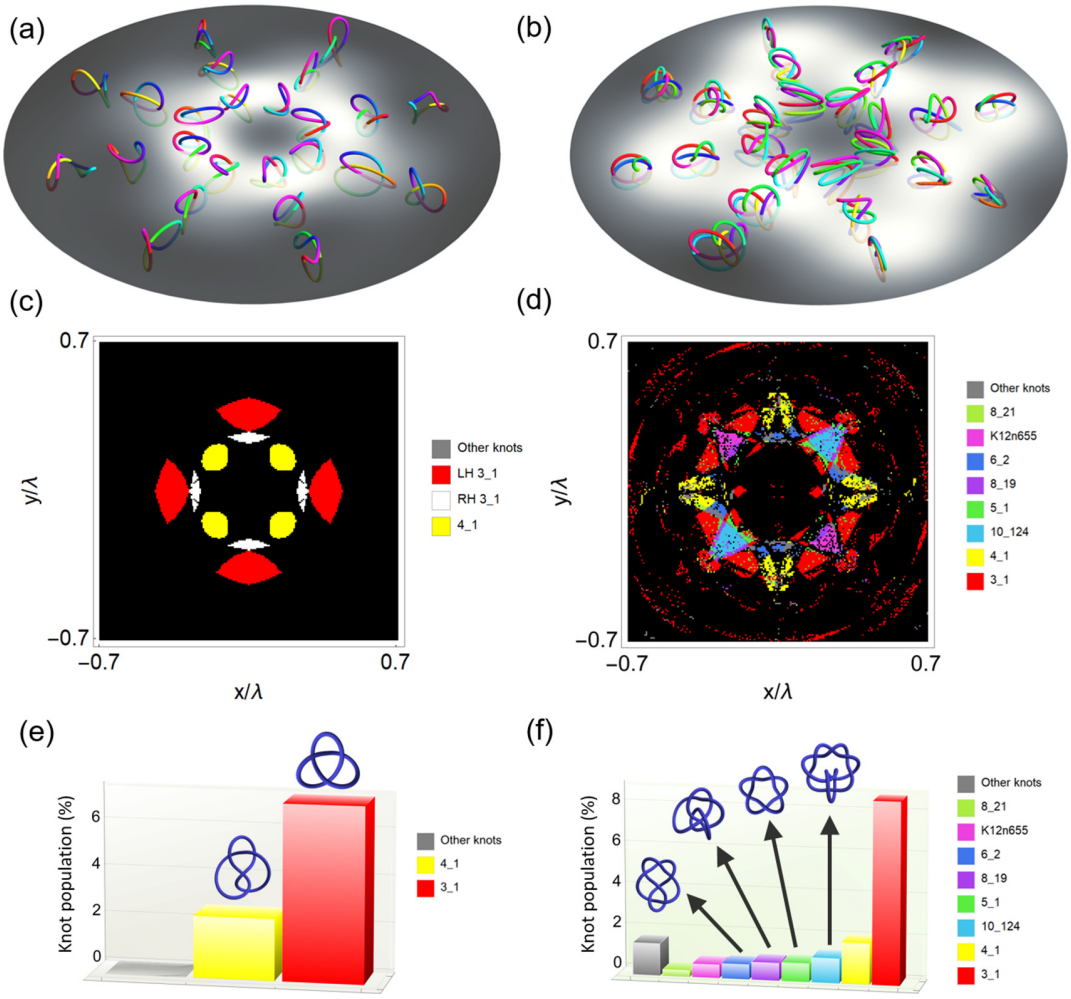

FIG. 4. Distribution of polarization curves (forming knots) at the focal plane obtained by tight-focusing the field given by (5). For (a), (c), and (e), $\omega_2/\omega_1 = 3$ and $\omega_3/\omega_1 = 2$, and for (b), (d), and (f), $\omega_2/\omega_1 = 3/2$ and $\omega_3/\omega_1 = 5/2$. In (a) and (b), some of the curves traced by the local electric field superimposed with the total intensity are shown. For (c) and (d), we performed a point-by-point classification of the knots traced by the local electric field. In (c) we also identified the chirality of the trefoil knots. Different colors correspond to different types of knots, as specified in the legend according to the standard nomenclature. LH, left handed; RH, right handed. Black is associated with unknots. The histograms (e) and (f) show the relative probability density of the different knot topologies within the considered region.

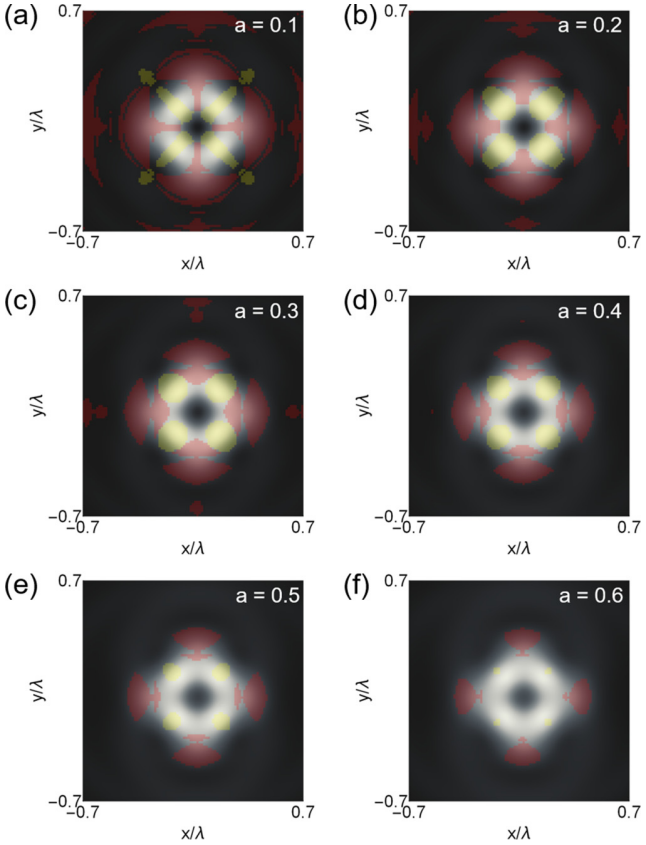

FIG. 5. Spatial distribution of polarization curves at the focal plane obtained by tight-focusing the field given by Eq. (5) when the frequencies follow the ratios $\omega_2/\omega_1 = 3$ and $\omega_3/\omega_1 = 2$ for different values of $a = a_1/a_2 = a_1/a_3$. Red and yellow markers correspond to trefoil and figure-eight knotted polarizations, respectively. Meanwhile, black markers are associated with unknots.

fering propagation directions—and, consequently, all three components of the electric field—naturally arise. The time-dependent fields at a plane in the focal volume are given by the the Richards-Wolf diffraction integral [23]. We calculated the components of the focused fields by numerical methods (see Appendix A). Here, we have considered that the focusing occurs in air due to a microscope objective with a high numerical aperture (NA = 0.95). From the obtained fields, the polychromatic polarization states can be constructed by the superposition of the different harmonic components. It is noteworthy that a plethora of complicated polarization curves is expected due to the nonuniform amplitude distribution arising from the tight focusing.

We then proceed to perform the identification and classification of the polarization curves. While some knots can be recognized by visual inspection, numerical tools were employed for a more systematic approach in order to classify the three-dimensional curves [31]. A set of 10 000 curves uniformly distributed within the numerical window at the plane of interest in the focal volume are considered in the classification. The identification of each curve is done by making use of the knot determinant and the Alexander polynomial, while its chirality is tested by calculating the Jones polynomial [30].

IV. RESULTS AND DISCUSSION

As a first example, let us start by considering the simplest possible case given as the superposition of three Gaussian beams with different polarization states and frequencies. Therefore it is possible to write such a superposition as

$$\mathbf{E}(\mathbf{r}, t) = e^{-r^2/w^2} \sum_{m=1}^{3} a_m \, e^{-i\omega_m t} \, \hat{\mathbf{e}}_\mathbf{m}, \tag{3}$$

where w stands for the waist parameter of a Gaussian beam, which we assumed to be equal for all three harmonic components. Figures 2(b) and 2(c) show two possible configurations for the electric field described by Eq. (3) where the frequencies are related by $\omega_2/\omega_1 = 2$ and $\omega_3/\omega_1 = 3$, corresponding to the first three coprime numbers. Knotted polarization states are present in both cases, but the populations of these exotic states are relatively small and only contain trefoil topologies. As expected, the spatial distribution of the knotted curves on the focal plane depends on the polarization states of the paraxial beams, i.e., larger regions are obtained when the beams with higher frequencies are circularly polarized.

Though we have been able to generate knotted polarization curves, their population is small and confined to extremely localized regions. In order to develop a strategy to generate larger populations of knotted states, it is convenient to recall the action of the lens on the input beam's polarization state. As shown in Fig. 2(a), the incident polarization state is decomposed using the triad $\{\mathbf{e}_r, \mathbf{e}_\phi, \mathbf{k}\}$ [23], representing the radial, azimuthal, and wave-vector unit vectors, respectively. In this scenario, a large longitudinal component of the focused field is generated from the radial component of the input field. This component is therefore instrumental in adding a third dimension to the oscillation of the electric field, which, as shown in Eq. (1), is necessary for generating a knotted curve. Meanwhile, the azimuthal contribution of the field remains practically unchanged. These features thereby motivate expressing the three frequency components in terms of beams that predominantly polarized along $\mathbf{e}_r$ and $\mathbf{e}_\phi$. For this reason, we opt to examine the three-dimensional patterns that arise from the tight focusing of vector vortex beams. In particular, we consider the class of vector vortex beams, in cylindrical coordinates $\mathbf{r} = (r, \phi, z)$ (at the lens input pupil plane), defined as

$$\mathbf{E}_\mathbf{v}(\mathbf{r}\,; \ell, \delta) = \frac{1}{\sqrt{2}} A_{|\ell|}(r)[e^{i\ell\phi} \, \hat{\mathbf{e}}_\mathbf{R} + e^{i\delta} e^{-i\ell\phi} \, \hat{\mathbf{e}}_\mathbf{L}]. \tag{4}$$

Here, $\{\hat{\mathbf{e}}_\mathbf{L}, \hat{\mathbf{e}}_\mathbf{R}\}$ are unit vectors for left- and right-handed circular polarization; the factors $\exp(\pm i\ell\phi)$, with ℓ being an integer, give the OAM content of each circular polarization component; and $A_{|\ell|}(r)$ specifies the complex radial amplitude distribution of the electric field. In our calculations, we considered the case of Laguerre-Gaussian modes, $A_{|\ell|}(\mathbf{r})e^{i\ell\phi} = \mathrm{LG}^0_\ell(r, \phi)$, with radial index $p = 0$ and topological charge ℓ. The three-dimensional polarization distributions at the focal plane $z = 0$ are shown in Fig. 3 for the cases of $|\ell| = 1$ and

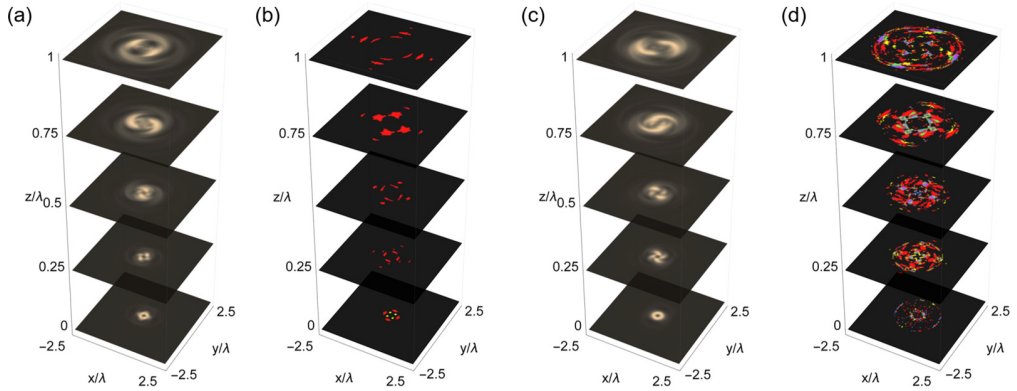

FIG. 6. Effect of propagation on total intensity and knotted polarization distribution for (a) and (b) $\omega_2/\omega_1 = 3$ and $\omega_3/\omega_1 = 2$ and (c) and (d) $\omega_2/\omega_1 = 3/2$ and $\omega_3/\omega_1 = 5/2$. Panels (a) and (c) show the total intensity distribution, while (b) and (d) display the knot positions and their types. The color coding in the knot distribution plots is the same as given in Fig. 4.

$\delta = \{0, \pi\}$ in (4). Note that, by considering a polychromatic superposition, i.e.,

$$\mathbf{E}(\mathbf{r}, t) = a_1\, e^{-i\omega_1 t}\, \mathbf{E}_{\mathbf{v}}(\mathbf{r}, 1, 0) + a_2\, e^{-i\omega_2 t}\, \mathbf{E}_{\mathbf{v}}(\mathbf{r}, -1, 0) + a_3 e^{-i\omega_3 t}\, \mathbf{E}_{\mathbf{v}}(\mathbf{r}, -1, \pi), \tag{5}$$

and focusing it, the curve traced by the local electric field vector takes the form of a Fourier-(3,3,3) knot in its more general form. Additionally, in order to maximize the region in which the longitudinal component of the field is non-negligible, we set $\omega_1 = \min(\{\omega_n\})$. This condition arises from the fact that at higher frequencies, the region where the beam amplitude is non-negligible becomes smaller (see Appendix A). Therefore knotted electric field curves are formed at the focal plane depending on the chosen temporal frequencies and the local relative phase and amplitudes of the chromatic components of the input beam.

As a first example of the proposed approach, let us consider the temporal frequencies in Eq. (5) to be related by $\omega_2/\omega_1 = 3$ and $\omega_3/\omega_1 = 2$, which correspond to the first three coprime numbers. In addition, we set $a_2/a_1 = a_3/a_1 = 2$ and consider the same waist parameter for the Laguerre-Gaussian modes. Figure 4(a) shows the the amplitude profile of the tightly focused field overlaid with the curves traced out by the resulting knotted polarization vectors. Figure 4(c) shows the regions in which different knotted structures are located on the focal plane. About 7.5% of the analyzed trajectories were identified as either left- or right-chiral trefoil knots (3_1), while 2.5% corresponded to figure-eight knots (4_1) [see Fig. 4(e)]. It should be noted that, by following a circular path around the origin, it is possible to observe the transition between unknots and knotted trajectories. It is worthy of emphasis that only the non-negligible longitudinal component arises from focusing $\mathbf{E}_{\mathbf{v}}(\mathbf{r}, 1, 0)$, while the remaining terms generate the transverse basis on the focal volume. Therefore we present a brief exploration on the effect of the relative amplitude of the longitudinal component. Figure 5 depicts the spatial distribution of knotted polarization states when the ratio between the relative amplitudes $a = a_1/a_2 = a_1/a_3$ is varied. In all the cases, only trefoils and figure-eight polarization knots are created. From these results, it becomes evident that the spatial distribution of the knotted polarization curves can be tailored by modifying the relative amplitude of the radial component of the superposition.

Similarly, we present the analysis of a case in which the superposition is composed of structured beams with higher harmonics of an arbitrary frequency. For instance, we consider the frequencies $\omega_2/\omega_1 = 3/2$ and $\omega_3/\omega_1 = 5/2$, where these values correspond to the next three lowest possible coprime numbers: 2, 3, and 5. As shown in Figs. 4(b), 4(d), and 4(f), about 25% of the analyzed trajectories are nontrivial knots, including the presence of trefoil, cinquefoil (5_1), and three-twist knots.

Heretofore, we have considered the existence of knotted polarization states exclusively on the focal plane ($z = 0$). A more complete analysis should include the evolution of the three-dimensional polarization distribution upon propagation in the focal volume. As shown in Fig. 6, knotted structures adiabatically follow the beam propagation. In Fig. 6(a), trefoil knots are present in a region that extends beyond the fundamental wavelength $\lambda = 2\pi c/\omega_{\min}$. Our calculations show that, since the longitudinal component of the electric field becomes negligible far from the focus, these polarization knots disappear at a distance $\Delta z = 2\lambda$ from the focal plane (not shown in the figure). Similarly, Fig. 6(b) shows the knot propagation for the case $\omega_2/\omega_1 = 3/2$ and $\omega_3/\omega_1 = 5/2$.

In summary, we have introduced a heuristic criterion to generate large and rich populations of locally knotted polarization curves by tight-focusing three structured beams at different frequencies. These structures can be generated and detected with the current techniques developed in nonlinear optics and nanophotonics, e.g., exploiting the recent advances in phase locking and independent manipulation of different harmonics [32] and, for what concerns the detection, by properly analyzing the scattering of the focused beams from metal nanoparticles [33]. In addition, interaction of these locally knotted fields with (semiconductor) materials might induce local three-dimensional magnetic behavior.

ACKNOWLEDGMENTS

37 The authors acknowledge the fruitful conversations with Dr. Sergey Nechayev. This work was supported by Canada Research Chairs (CRC), Canada First Excellence Research Fund (CFREF), and Ontario's Early Researcher Award.

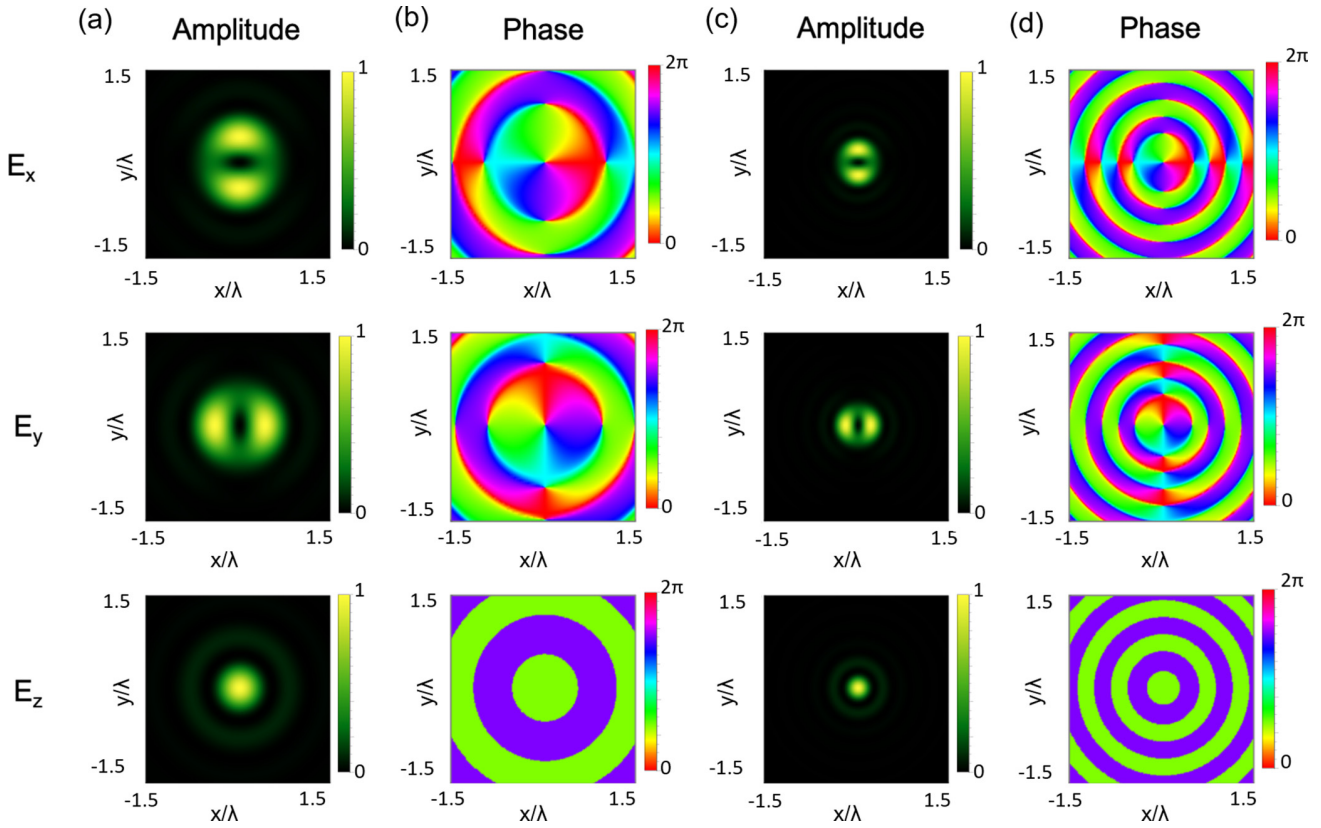

FIG. 7. Amplitude and phase distributions of the electric field components obtained by tightly focusing a LG_1^0 mode (with left circular polarization). (a) and (b), and (c) and (d), correspond to two different optical frequencies: (a) and (b) $\omega_1 = 2\pi c/\lambda$; (c) and (d) $\omega_2 = 2\omega_1$.

APPENDIX A: TIGHTLY FOCUSED POLYCHROMATIC LIGHT

The time-dependent electric field $\mathbf{E}_f(\rho, \varphi, z, t; \omega)$ at the focal plane of an aplanatic lens, with focal length f and a high numerical aperture (NA), is given by Richards and Wolf's diffraction integral [23],

$$\mathbf{E}_f(\rho, \varphi, z, t; \omega) = -\frac{if\omega}{2\pi c} e^{i\omega t} \int_0^{\Theta} \sin\theta \, d\theta e^{ikz\cos\theta} \int_0^{2\pi} \mathbf{A}(\phi, \theta, t; \omega) e^{ik\rho \sin\theta \cos(\varphi-\phi)} d\phi, \tag{A1}$$

where $k = \omega/c$ stands for the wave number, $\Theta = \arcsin(\mathrm{NA}/n)$ is the maximum angular aperture of the objective, n is the refractive index of the medium, and

$$\mathbf{A}(\phi, \theta) = \mathbf{T} \cdot \mathbf{E}_{\mathrm{in}}(\phi, \theta)$$

is the transformation of the initial beam $\mathbf{E}_{\mathrm{in}} = (U_x, U_y, 0)^T$ after the objective. The transformation matrix is given as

$$\mathbf{T} = \sqrt{\cos\theta} \begin{bmatrix} \cos\theta\cos^2\phi + \sin^2\phi & (\cos\theta - 1)\sin\phi\cos\phi & \sin\theta\cos\phi \\ (\cos\theta - 1)\sin\phi\cos\phi & \cos\theta\sin^2\phi + \cos^2\phi & \sin\theta\sin\phi \\ -\sin\theta\cos\phi & -\sin\theta\sin\phi & \cos\theta \end{bmatrix}. \tag{A2}$$

Similarly, it is possible to rewrite (A1) to be

$$\mathbf{E}_f(\rho, \varphi, z) = -\frac{if\omega}{2\pi c} e^{i\omega t} \sum_{m=0}^{\infty} \int_0^{\theta} \sin\theta \, d\theta e^{ikz\cos\theta} \times \int_0^{2\pi} \mathbf{A}(\phi, \theta) i^m \mathrm{J}_m(k\rho\sin\theta) e^{im(\varphi-\phi)} \, d\phi, \tag{A3}$$

where $\mathrm{J}_m(\cdot)$ stands for the mth-order Bessel function of the first kind. Therefore it is possible to construct a tightly focused polychromatic field as

$$\mathbf{E}(\rho, \varphi, z, t) = \sum_{m=1}^{N} \mathrm{Re}\left[a_m \mathbf{E}_f^m(\rho, \varphi, z, t; \omega_m)\right], \tag{A4}$$

where $\{\omega_m\}$ are complex numbers. We expect to find polarization knots in regions where the intensities of the three frequency components are comparable.

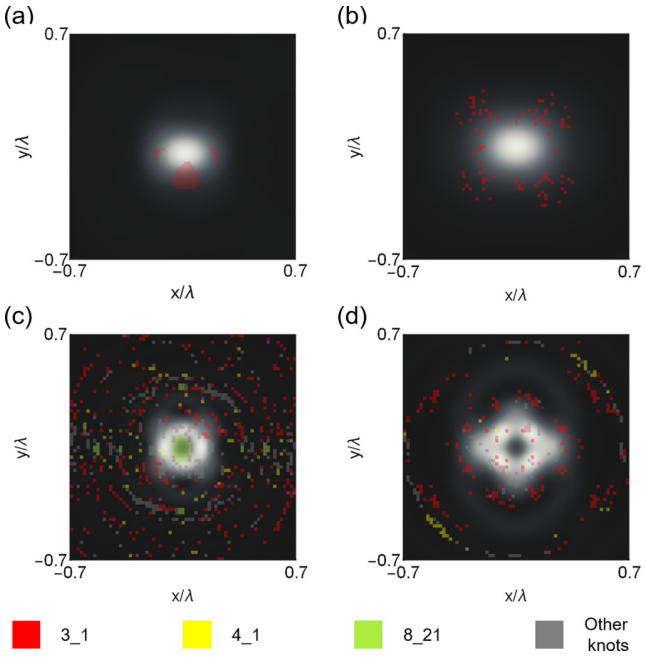

FIG. 8. Spatial distribution of knotted polarization curves at the focal plane obtained by tightly focusing the fields given by (a) Eq. (B1) for $\omega_2/\omega_1 = 2$ or $\omega_3/\omega_1 = 3$ when the Gaussian beams are circularly polarized and (b)–(d) Eq. (5) for $\omega_2/\omega_1 = 2$ and $\omega_3/\omega_1 = 3$ (b), $\omega_2/\omega_1 = 5$ and $\omega_3/\omega_1 = 3$ (c), and $\omega_2/\omega_1 = 4/3$ and $\omega_3/\omega_1 = 5/3$ (d).

It is thus useful to keep in mind that the spatial extension of a tightly focused beam decreases with the frequency, as illustrated in Fig. 7.

APPENDIX B: OTHER KNOT PATTERNS OBTAINED FROM DIFFERENT OPTICAL SUPERPOSITIONS

Following the analysis in Sec. IV, we present some other possible configurations. First, let us consider the superposition of two Gaussian beams with different polarization states and a radially polarized beam,

$$\mathbf{E}(\mathbf{r},t) = 2e^{-r^2/w^2}(\hat{\mathbf{e}}_1 e^{-\omega_2 t} + \hat{\mathbf{e}}_2 e^{-\omega_3 t}) + e^{-\omega_1 t}\mathbf{E}_{\mathbf{v}}(\mathbf{r},1,0), \tag{B1}$$

where $\{\hat{\mathbf{e}}_1, \hat{\mathbf{e}}_1\}$ are orthogonal polarization states. For the sake of simplicity, the temporal frequencies are related by $\omega_2/\omega_1 = 2$ or $\omega_3/\omega_1 = 3$. Figure 8(a) the knot distribution resulting from the tight focusing of Eq. (B1) when $\{\hat{\mathbf{e}}_1, \hat{\mathbf{e}}_1\}$ form the circular polarization basis. As in the case of the superposition of three Gaussian beams, a small population of knotted polarization states is generated. Meanwhile, nontrivial polarization curves are obtained when the Gaussian beams are linearly polarized. Figures 8(b)–8(d) depict the spatial distribution of three-dimensional curves obtained by tight-focusing the beam given in Eq. (5) for different sets of frequencies.

[1] J. F. Nye and M. V. Berry, Dislocations in wave trains, Proc. R. Soc. London, Ser. A **336**, 165 (1974).

[2] M. Soskin, V. Gorshkov, M. Vasnetsov, J. Malos, and N. Heckenberg, Topological charge and angular momentum of light beams carrying optical vortices, Phys. Rev. A **56**, 4064 (1997).

[3] M. R. Dennis, K. O'Holleran, and M. J. Padgett, Singular optics: Optical vortices and polarization singularities, Prog. Opt. **53**, 293 (2009).

[4] L. Allen, M. W. Beijersbergen, R. Spreeuw, and J. Woerdman, Orbital angular momentum of light and the transformation of Laguerre-Gaussian laser modes, Phys. Rev. A **45**, 8185 (1992).

[5] H. He, M. Friese, N. Heckenberg, and H. Rubinsztein-Dunlop, Direct Observation of Transfer of Angular Momentum to Absorptive Particles from a Laser Beam with a Phase Singularity, Phys. Rev. Lett. **75**, 826 (1995).

[6] R. Chen, K. Agarwal, C. J. Sheppard, and X. Chen, Imaging using cylindrical vector beams in a high-numerical-aperture microscopy system, Opt. Lett. **38**, 3111 (2013).

[7] K. Zhanghao, X. Chen, W. Liu, M. Li, Y. Liu, Y. Wang, S. Luo, X. Wang, C. Shan, H. Xie, J. Gao, X. Chen, D. Jin, X. Li, Y. Zhang, Q. Dai, and P. Xi, Super-resolution imaging of fluorescent dipoles via polarized structured illumination microscopy, Nat. Commun. **10**, 4694 (2019).

[8] S. W. Hell and J. Wichmann, Breaking the diffraction resolution limit by stimulated emission: Stimulated-emission-depletion fluorescence microscopy, Opt. Lett. **19**, 780 (1994).

[9] J. J. Nivas, S. He, A. Rubano, A. Vecchione, D. Paparo, L. Marrucci, R. Bruzzese, and S. Amoruso, Direct femtosecond laser surface structuring with optical vortex beams generated by a q-plate, Sci. Rep. **5**, 17929 (2015).

[10] A. E. Willner, H. Huang, Y. Yan, Y. Ren, N. Ahmed, G. Xie, C. Bao, L. Li, Y. Cao, Z. Zhao, J. Wang, M. P. J. Lavery, M. Tur, S. Ramachandran, A. F. Molisch, N. Ashrafi, and S. Ashrafi, Optical communications using orbital angular momentum beams, Adv. Opt. Photonics **7**, 66 (2015).

[11] F. Bouchard, A. Sit, F. Hufnagel, A. Abbas, Y. Zhang, K. Heshami, R. Fickler, C. Marquardt, G. Leuchs, R. W. Boyd, and E. Karimi, Quantum cryptography with twisted photons through an outdoor underwater channel, Opt. Express **26**, 22563 (2018).

[12] M. V. Berry and M. R. Dennis, Knotted and linked phase singularities in monochromatic waves, Proc. R. Soc. London, Ser. A **457**, 2251 (2001).

[13] M. R. Dennis, R. P. King, B. Jack, K. O'Holleran, and M. J. Padgett, Isolated optical vortex knots, Nat. Phys. **6**, 118 (2010).

[14] D. Sugic and M. R. Dennis, Singular knot bundle in light, J. Opt. Soc. Am. A **35**, 1987 (2018).

[15] H. Larocque, D. Sugic, D. Mortimer, A. J. Taylor, R. Fickler, R. W. Boyd, M. R. Dennis, and E. Karimi, Reconstructing the topology of optical polarization knots, Nat. Phys. **14**, 1079 (2018).

[16] H. Larocque, A. D'Errico, M. F. Ferrer-Garcia, A. Carmi, E. Cohen, and E. Karimi, Optical framed knots as information carriers, Nat. Commun. **11**, 5119 (2020).

[17] M. Feng, Quantum computing in cavity QED with cold trapped ions by bichromatic radiation, Phys. Rev. A **65**, 064301 (2002).

[18] M. Andersen, C. Ryu, P. Cladé, V. Natarajan, A. Vaziri, K. Helmerson, and W. D. Phillips, Quantized Rotation of Atoms from Photons with Orbital Angular Momentum, Phys. Rev. Lett. **97**, 170406 (2006).

[19] M. Bhattacharya, H. Uys, and P. Meystre, Optomechanical trapping and cooling of partially reflective mirrors, Phys. Rev. A **77**, 033819 (2008).

[20] I. Kozyryev, L. Baum, L. Aldridge, P. Yu, E. E. Eyler, and J. M. Doyle, Coherent Bichromatic Force Deflection of Molecules, Phys. Rev. Lett. **120**, 063205 (2018).

[21] S. Sederberg, F. Kong, F. Hufnagel, C. Zhang, E. Karimi, and P. B. Corkum, Vectorized optoelectronic control and metrology in a semiconductor, Nat. Photonics **14**, 680 (2020).

[22] I. Freund, Bichromatic optical Lissajous fields, Opt. Commun. **226**, 351 (2003).

[23] B. Richards and E. Wolf, Electromagnetic diffraction in optical systems, II. Structure of the image field in an aplanatic system, Proc. R. Soc. London, Ser. A **253**, 358 (1959).

[24] T. Bauer, P. Banzer, E. Karimi, S. Orlov, A. Rubano, L. Marrucci, E. Santamato, R. W. Boyd, and G. Leuchs, Observation of optical polarization Möbius strips, Science **347**, 964 (2015).

[25] T. Bauer, P. Banzer, F. Bouchard, S. Orlov, L. Marrucci, E. Santamato, R. W. Boyd, E. Karimi, and G. Leuchs, Multi-twist polarization ribbon topologies in highly-confined optical fields, New J. Phys. **21**, 053020 (2019).

[26] T. Bauer, S. N. Khonina, I. Golub, G. Leuchs, and P. Banzer, Ultrafast spinning twisted ribbons of confined electric fields, Optica **7**, 1228 (2020).

[27] S. Gao, F. C. Speirits, F. Castellucci, S. Franke-Arnold, S. M. Barnett, and J. B. Götte, Paraxial skyrmionic beams, Phys. Rev. A **102**, 053513 (2020).

[28] D. Sugic, M. R. Dennis, F. Nori, and K. Y. Bliokh, Knotted polarizations and spin in three-dimensional polychromatic waves, Phys. Rev. Research **2**, 042045(R) (2020).

[29] A. Stasiak and V. Katritch, *Ideal Knots*, Series on Knots and Everything Vol. 19 (World Scientific, Singapore, 1998).

[30] L. H. Kauffman, *Knots and Physics*, Series on Knots and Everything Vol. 1 (World Scientific, Singapore, 2001).

[31] A. J. Taylor and other SPOCK contributors, pyknotid knot identification toolkit, https://github.com/SPOCKnots/pyknotid (2017), accessed Dec. 1, 2020.

[32] H.-S. Chan, Z.-M. Hsieh, W.-H. Liang, A. Kung, C.-K. Lee, C.-J. Lai, R.-P. Pan, and L.-H. Peng, Synthesis and measurement of ultrafast waveforms from five discrete optical harmonics, Science **331**, 1165 (2011).

[33] T. Bauer, S. Orlov, U. Peschel, P. Banzer, and G. Leuchs, Nanointerferometric amplitude and phase reconstruction of tightly focused vector beams, Nat. Photonics **8**, 23 (2014).

Chapter 4

Encoding information in low-dimensional topological elements

This chapter is based on the following papers:

1. Larocque, Hugo, Alessio D'Errico, **Manuel F. Ferrer-Garcia**, Avishy Carmi, Eliahu Cohen, and Ebrahim Karimi. "Optical framed knots as information carriers." Nature Communications 11, no. 1 (2020): 5119.

2. **M. F. Ferrer-García**, A. Carmi, A. D'Errico, H., E. Cohen, Ebrahim Karimi, "Secure communication using low-dimensional topological elements", *arXiv*:2212.04350 (2022). DOI: https://doi.org/10.48550/arXiv.2212.04350

As a light beam carrying an optical vortex propagates in free space, the singularity traces a line in three dimensions. Therefore, it is possible to engineer light fields whose singular skeletons define closed non-trivial curves, such as links and knots [20, 82]. Based on the method in [83], it is possible to equip a framing, i.e. a continuous vector field, to the singular skeleton. This framing is given from the spatially-variant polarization structure imposed on the knotted field. The first part of this chapter presents the experimental methodology used to reconstruct an optical framed knot. Similarly, it introduces a prime-encoding scheme based on the non-surjective mapping between the framed knot and their framed braid representation. In the second part, the authors propose a challenge-response algorithm as an extension to the encoding mechanism previously described. The use of low-dimensional elements represents a reliable framework for communications due to their greater resilience to environmental distubances [84]. A brief introduction to knot theory

and the relationship with the braid groups is covered in Section 3.2. The supplementary information of the work here presented is contained in Appendix B.

4.1 The braid group

As mentioned, knots and links are related to another set of low-dimensional elements: braids. As shown in Figure 4.1-a, it is possible to imagine a braid in s-strands or a s-braid S as an object consisting of two parallel planes connected by a collection of s non-intersecting strands. For the sake of practicality, braids tend to be visualized using a two-dimensional projection such that every point on the projection corresponds to a maximum of two points from different strands, and all crossings occur at different locations.

In contrast to knots and links, the set of s-braids exhibits the structure of a group [85]. Then, $\mathcal{B}_s$ may be presented the set of generators $\sigma_1, \sigma_2, \ldots, \sigma_s$ and the relations between them,

$$\mathcal{B}_s = \left\langle \sigma_1, \ldots, \sigma_{s-1} \,\middle|\, \begin{array}{l} \sigma_{j+1}\sigma_j\sigma_{j+1} = \sigma_j\sigma_{j+1}\sigma_j, \\ \sigma_i\sigma_j = \sigma_j\sigma_i \end{array} \right\rangle, \tag{4.1}$$

where the last relation holds for $|i - j| > 1$. Thus, a particular realization of a specific realization of a s-braid S, or *word* can be expressed as a product of the generators. Geometrically, the generator σ_i corresponds to performing a crossing where the i-th strand goes over the $(i + 1)$-th strand (See Figure 4.1-b). In the same fashion, it is possible to define the inverse operation σ_i^{-1}. Note that if we ignore the braiding processes and only focus on the initial and final positions, our s-braids determine a permutation of s elements. Therefore, it is possible to say that $\mathcal{B}_s$ is homomorphic to the symmetric group S_s [85].

Despite their apparent differences, Alexander's braiding theorem states every link can be obtained from the closure of a braid, i.e. every link is combinatorially equivalent [86]. A braid is said to be closed when each strand's corresponding top and bottom ends are attached to each other (See Figure 4.1-a). Although, it must be noted that the closure mapping is surjective: a link may admit multiple braid representations, even from different braid groups. A stronger and more definitive relation between links and braids is given by the Markov theorem [87]: given two braids S_n and S'_m in the braid groups $\mathcal{B}_n$ and $\mathcal{B}_m$, their closure leads to equivalent links if and only if one of the braids can be transformed into the other one by applying a sequence of these operations:

1. *Conjugation*: Consider two braids $S, G \in \mathcal{B}_n$. We can define the conjugated braid $B = GSG^{-1}$ such that when it is closed, B and B^{-1} cancel each other out.

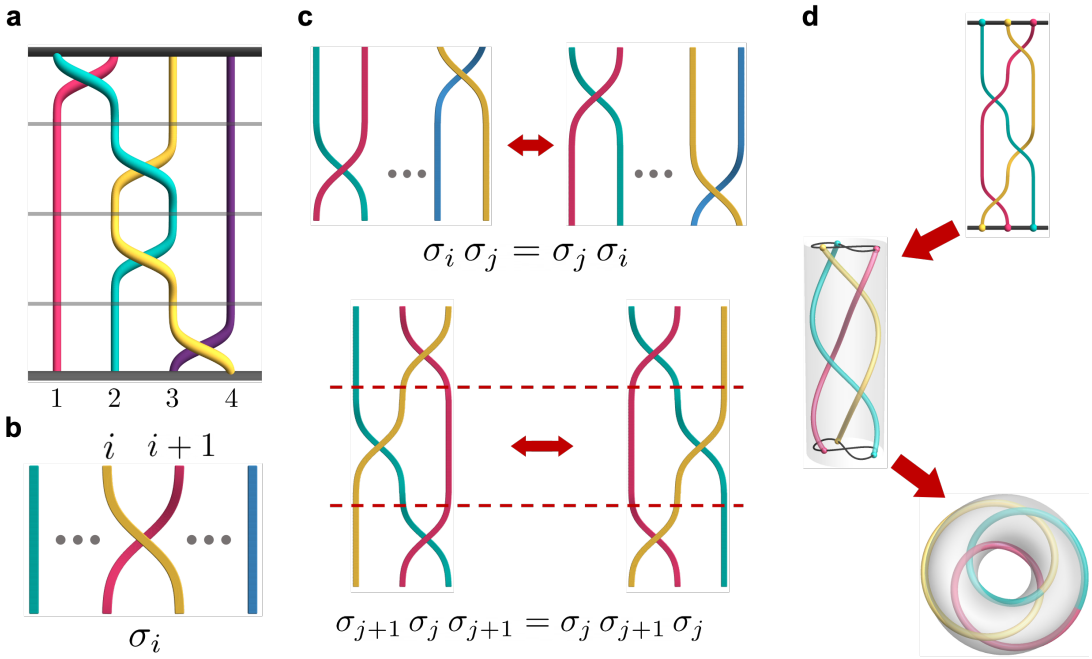

Figure 4.1: **Braids and their properties a.** Example of a braid on four strands. Notice that the output of the braiding operation represents a permutation of the input state. **b.** Geometrical representation of the group generator σ_i. Any element of the braid group can be expressed in terms of σ_i and its inverse operation σ_i^{-1} ando c **c.** Defining relations for the representation of the group $\mathcal{B}_s$. The first relation establishes the commutativity of the crossing for non-adjacent strands when $|i-j| > 1$. The second one shows the equivalence of braids can be accomplished by applying crossing operators from both sides. **d.** Depiction of Alexander's theorem for a braid on three strands.

2. *Markov move*: replacing a braid $S_n \in \mathcal{B}_n$ by $S_n\,\sigma_n^{\pm 1} \in \mathcal{B}_{n+1}$. Geometrically, this is visualized as adding a strand to the right of the braid and crossing it once with the adjacent strand. It should be noted that the inverse operation $S_n\,\sigma_n^{\pm 1} \in \mathcal{B}_{n+1}$ by $S_n \in \mathcal{B}_n$ is also admissible.

Additionally, the braid group $\mathcal{B}_s$ admits a local representation on a tensor space $V^{\otimes}$, where V is a vector space. This can be accomplished by the mapping $\psi_s : \mathcal{B}_s \to \mathrm{End}(V^{\otimes})$,

$$\psi_s(\sigma_j) = \mathbb{1}^{\otimes(j-1)} \otimes R \otimes \mathbb{1}^{\otimes(s-j-1)} = R_j, \tag{4.2}$$

where $\mathbb{1}$ stands as the identity element, $\mathrm{End}(\cdot)$ implies an endomorphism, and R is a linear

mapping $R : V \otimes V \to V \otimes V$ that satisfies the Yang-Baxter equation

$$(R \otimes \mathbb{1})(\mathbb{1} \otimes R)(R \otimes \mathbb{1}) = (\mathbb{1} \otimes R)(R \otimes \mathbb{1})(\mathbb{1} \otimes R). \tag{4.3}$$

Note that unitary solutions to the Yang-Baxter equations can be regarded as quantum gates, giving us a link between a braiding operation and an entanglement operator acting on a composite system [77].

4.1.1 Framed Knots and Framed braids

Heretofore, we have discussed simple low-dimensional elements, such as classical knots and links. Now, let us extend the definition of a knot by equipping the curve with a continuous non-vanishing vector field V normal to it at all points, called framing. As a result of this composition, we obtained a new type of topological element called a framed knot. For the sake of simplicity, let us ignore the magnitude of the vector field since we are only interested in its structure. Therefore, a framed knot (K, V) can be visualized as a tangled ribbon whose ends have been glued together after an even number m of half-twists. In practice, m stands for the framing integer and allows us to define the equivalence class of the V. It must be noted that the ribbons obtained from framed knots are orientable surfaces [88]. Therefore, framed knots are a particular case of the more general concept of knotted ribbons.

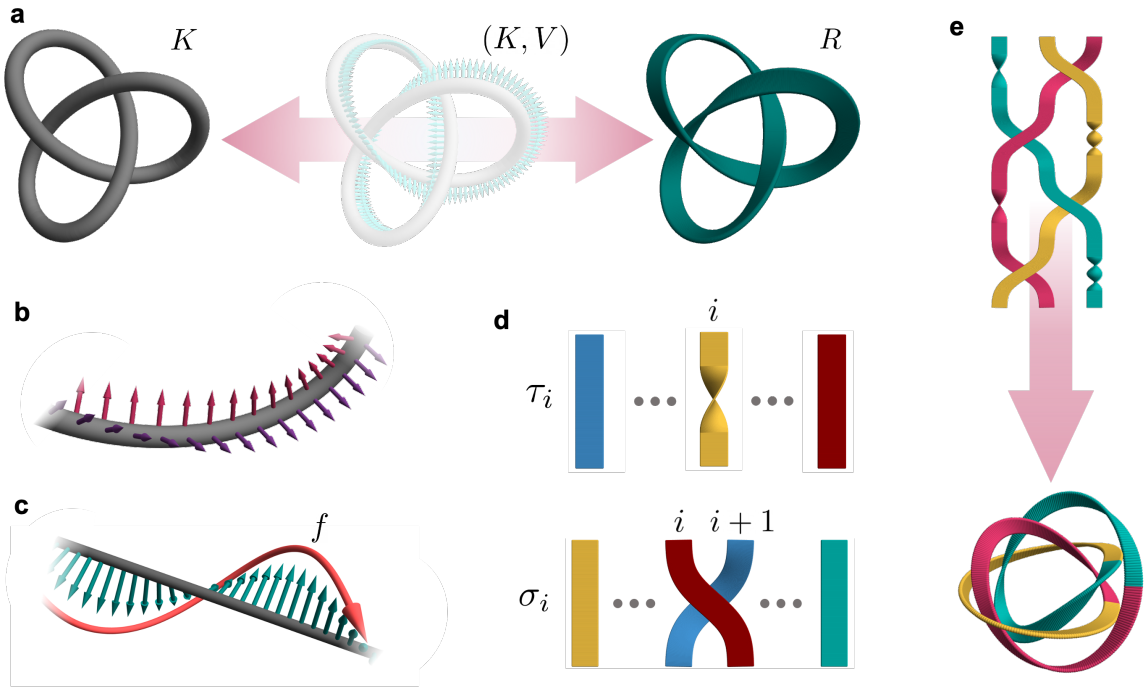

Figure 4.2: **Framed knots and their representation a.** A framed knot (K, V) is obtained by equipping a knot K with the vector field V. They represent a subset of the knotted ribbons since a framed knot always produces an orientable surface. **b.** It is possible to define a local frame such that it exists on the transverse plane to the curve. **c.** The number of twists on a framing defines a topological invariant, called the framing number f. Two framings belong to the same equivalent class if both have identical framing numbers. **d.** It is possible to extend Alexander's theorem to the case of framed braids. However, by closing the braid representation, the distribution of twists per strand is lost.

Similarly, it is possible to equip a vector field for each strand in a braid, defining a framed braid representation for a framed knot (K, V). A twist on a particular strand is taken into account by introducing τ_i as the generator of a half-twist on the i-th strand (See Figure 4.2-b). Hence, a framed s-braid allows the presentation [89]

$$\mathcal{FB}_s = \left\langle \sigma_1, \ldots, \sigma_{s-1}, \tau_1, \ldots, \tau_s \;\middle|\; \begin{array}{l} \sigma_{j+1}\sigma_j\sigma_{j+1} = \sigma_j\sigma_{j+1}\sigma_j, \\ \tau_i\tau_j = \tau_j\tau_i, \\ \tau_{j+1}\sigma_j = \sigma_j\tau_j,\ \sigma_j\tau_{j+1} = \tau_j\sigma_j \\ \sigma_i\sigma_j = \sigma_j\sigma_i,\ \tau_i\sigma_j = \sigma_j\tau_i \end{array} \right\rangle, \tag{4.4}$$

where σ_i is the braiding generator inherited from the unframed braid representation. It

must be noted that the framed braid group $\mathcal{FB}_s$ also admits a representation in a composite vector space $\mathcal{V}^{\otimes n} \otimes \mathcal{V}^{\otimes n}$, composed by both the framing and braiding corresponding spaces. As a result of this new complex structure, the definition of the braiding operator needs to be modified. It is straightforward to see that R_j acts as a swap gate on the framing space while it generates entanglement on the braided space. Explicitly, it assumes the form

$$\begin{aligned} R_j = &\left[\mathbb{1}^{\otimes(j-1)} \otimes \mathrm{SWAP} \otimes \mathbb{1}^{\otimes(n-j-1)}\right] \\ &\otimes \left[\mathbb{1}^{\otimes(j-1)} \otimes R \otimes \mathbb{1}^{\otimes(n-j-1)}\right]. \end{aligned} \tag{4.5}$$

Similarly, it is required to build a representation T_j for the half-turn twist generator τ_i. First, let us define $|k\rangle$ as the k-th strand in a framed s-braid. Consequently, a framed s-braid adopts the representation

$$F = \sum_{k}^{s} \alpha^{d_k} |k\rangle\langle k|, \tag{4.6}$$

where α is a real positive number and d_k is the number of half twists along the k-strand while considering that $d_k = -\infty$ for untwisted strands. Thus, the twisting operator corresponding to τ_j is given by the self-adjoint

$$T_j = \left(\sum_{k \neq j} |k\rangle\langle k| + \alpha |j\rangle\langle j|\right) \otimes \mathbb{1}^{\otimes n}. \tag{4.7}$$

It can be easily verified that R_j and T_j thus defined satisfy the relations of $\mathcal{FB}_s$.

nature COMMUNICATIONS

ARTICLE

https://doi.org/10.1038/s41467-020-18792-z OPEN

Optical framed knots as information carriers

Hugo Larocque[1,2✉], Alessio D'Errico[1], Manuel F. Ferrer-Garcia[1], Avishy Carmi[3], Eliahu Cohen[4] & Ebrahim Karimi[1✉]

Modern beam shaping techniques have enabled the generation of optical fields displaying a wealth of structural features, which include three-dimensional topologies such as Möbius, ribbon strips and knots. However, unlike simpler types of structured light, the topological properties of these optical fields have hitherto remained more of a fundamental curiosity as opposed to a feature that can be applied in modern technologies. Due to their robustness against external perturbations, topological invariants in physical systems are increasingly being considered as a means to encode information. Hence, structured light with topological properties could potentially be used for such purposes. Here, we introduce the experimental realization of structures known as framed knots within optical polarization fields. We further develop a protocol in which the topological properties of framed knots are used in conjunction with prime factorization to encode information.

[1] Department of Physics, University of Ottawa, Ottawa, ON, Canada. [2] Research Laboratory of Electronics, Department of Electrical Engineering and Computer Science, Massachusetts Institute of Technology, Cambridge, MA, USA. [3] Center for Quantum Information Science and Technology, Faculty of Engineering Sciences, Ben-Gurion University of the Negev, Beersheba, Israel. [4] Faculty of Engineering, Institute of Nanotechnology and Advanced Materials, Bar Ilan University, Ramat Gan, Israel. ✉email: hlarocqu@mit.edu; ekarimi@uottawa.ca

Structured light—optical fields with shaped spatial and temporal features[1]—provides a viable platform for the realization of a variety of topological structures. The creation of such structures mostly draws from concepts related to singular optics[2,3], i.e., the study of discontinuities in optical wavefields. Such discontinuities, which can be present in features such as optical phase[4] or polarization[5], are known as optical singularities and can be employed to produce optical beams of varying complexity from those carrying a single singularity[6] to more exotic wavefields forming structures such as topological bands and knots. The latter include Möbius strips[7–10], multi-twist ribbons[11], knots within scalar optical fields[12–14], knotted topologies within bichromatic fields[15], and knots in polarization fields, which include both knotted electromagnetic field lines[16–20] and knotted polarization singularities[21]. These structured optical fields carrying topological features have found numerous applications in modern science. Most notably, optical beams with a single singularity, which include orbital angular momentum modes, have been extensively employed in high-dimensional quantum information[22] along with both classical[23] and quantum communications[24]. Knots, which are generally described as topologically classified arrangements of some closed filament[25], have also emerged as a promising framework to enable new forms of technologies. This promise is mostly attributed to knots having a braid representation, which is a cornerstone of topological quantum information[26–30]. However, in spite of their significant potential, knots created within optical fields[12–15,21] are mostly investigated in experiments within the framework of information theory in a similar way to simpler optical beams carrying a single singularity[31]. They are more than often treated as two-dimensional transverse optical modes, as opposed to a three-dimensional object defined by prospectively more useful topological invariants. This shortcoming arguably arises from a current lack of overlap between the fields of topological quantum information and singular optics—that is, optical topologies that can currently be realized in the laboratory cannot be readily used as a platform for existing topological information protocols and vice-versa.

In this article, we introduce and experimentally demonstrate the generation and observation of structures in optical polarization wavefields forming framed knots. We then use the latter as information carriers by means of a protocol devised to encode topological information through the conjoined usage of prime factorization and the knots' own topological invariants.

Results

Framed C-lines. Knots ubiquitously describe how looped threads are arranged in space. For this reason, when analyzed within a physical framework, knots are typically found within fields defined by regions that unambiguously form curves in three-dimensional space. These knotted curves have been demonstrated in systems such as the vortices of fluids[32], the intensity nulls of scalar optical fields[12–14], and within the C-lines of optical polarization fields[21]. C-lines specifically consist of curves of pure circular polarization in monochromatic electromagnetic fields[33]. One of their most distinguishing features relates to the structure of the polarization field in their close proximity. Namely, they are enclosed by polarization ellipses with a major axis that rotates by integer multiples of π along a closed contour surrounding the C-line. This trait is in display in Fig. 1a, b. For the case of paraxial optical beams, polarization is confined within the plane transverse to the beam's propagation, e.g., the xy plane. As shown in Fig. 1a, this restriction constrains the plane over which this polarization axis rotation can be traced. Non-paraxial beams, however, can feature polarization vectors whose normal is not perpendicular to the beam's propagation. As displayed in Fig. 1b, this normal vector in turn dictates the plane in which the axis of the ellipse completes a half rotation around the C-line. The presence of these rotations consists of the key structural feature considered while defining the framed knots reported in this work.

A framed knot in three-dimensional space is a knot, i.e., a looped curve, equipped with a vector field called a framing. The framing is nowhere tangent to the knot and is characterized by a number, the framing integer, which is the linking number of the image of the ribbon with the knot. In other words, it counts the number of times the vector field twists (2π rotations) around the knot. Knotted ribbons generalize framed knots to an odd number of half-twists, e.g., knotted Möbius bands. Given the above definition, we define the framing of a closed C-line by the axis of the adjacent polarization ellipse whose axis is perpendicular to the C-line's tangent. This concept is illustrated in Fig. 1a, b, where we embolden the color of the polarization ellipse surrounding the C-line whose axis is perpendicular to its tangent, thereby defining its framing. In the rare case where all axes are perpendicular at a certain point of the C-line, the polarization vector defining the framing can be interpreted as the one enforcing its continuity with the least amount of twisting. This concept in turn defines the framing attributed to a knotted C-line. As illustrated in Fig. 1c, the latter may be constructed from a knotted field, $\mathbf{E}^k$, defined by a circularly polarized component, E_-^k, with knotted phase singularities, and a longitudinally polarized component, E_z^k, ensuring that $\mathbf{E}^k$ satisfies Maxwell's equations[34]. By superposing $\mathbf{E}^k$ with a plane wave with the opposite polarization helicity, E_+^p, knotted C-lines arising from the singular structure of $\mathbf{E}^k$ are created. As shown in Fig. 1d, e, increasing the amplitude of E_+^p with respect to that of E_z^k molds the resulting C-line into the knot formed by the phase singularities of E_-^k. Further discussions involving the dynamics of this process are provided in Supplementary Note 1. Note that E_z^k is negligible for paraxial beams, which are the main experimental focus of this work. Hence, for such beams, the C-line aligns with the aforementioned knotted vortices regardless of the amplitude of E_+^p[21].

Braid representation. In addition to their well-discernible three-dimensional structures, knots can also be represented by mathematical objects called braids. Geometrically, braids consist of intertwined arrangements of strands that do not turn back on ground that is already covered. Due to Alexander's theorem, every knot can be expressed as a closed braid. For instance, the trefoil knot shown in Fig. 2a can be expressed as the closure of the braid shown in Fig. 2b. The concept illustrated in these diagrams can be further extended to knots and braids formed in three-dimensional space. For example, the trefoil knot embedded in the torus shown in Fig. 2c can be obtained through a stereographic projection of the braid enclosed in the cylinder shown in Fig. 2d[14,35]. One way to perform this projection is to express this braid as the zeros of a complex field. This field is explicitly written as a function of the complex coordinates (u, v), which relate to the spatial coordinates, (x, y, h), in which the braid is embedded through $u = x + iy$ and $v = \exp(ih)$. This braided field can in turn be transformed into its corresponding knot with a stereographic projection defined by

$$u = \frac{\rho^2 + z^2 - 1 + 2iz}{\rho^2 + z^2 + 1}, \quad v = \frac{2\rho e^{i\varphi}}{\rho^2 + z^2 + 1}, \tag{1}$$

where (ρ, φ, z) are the cylindrical coordinates of the three-dimensional space in which the knot is now embedded. In essence, this projection wraps the braid defined over (x, y, h) into a knot in (ρ, φ, z) by connecting its two ends, thereby effectively mapping the h coordinate to φ[14]. Further discussions on how the

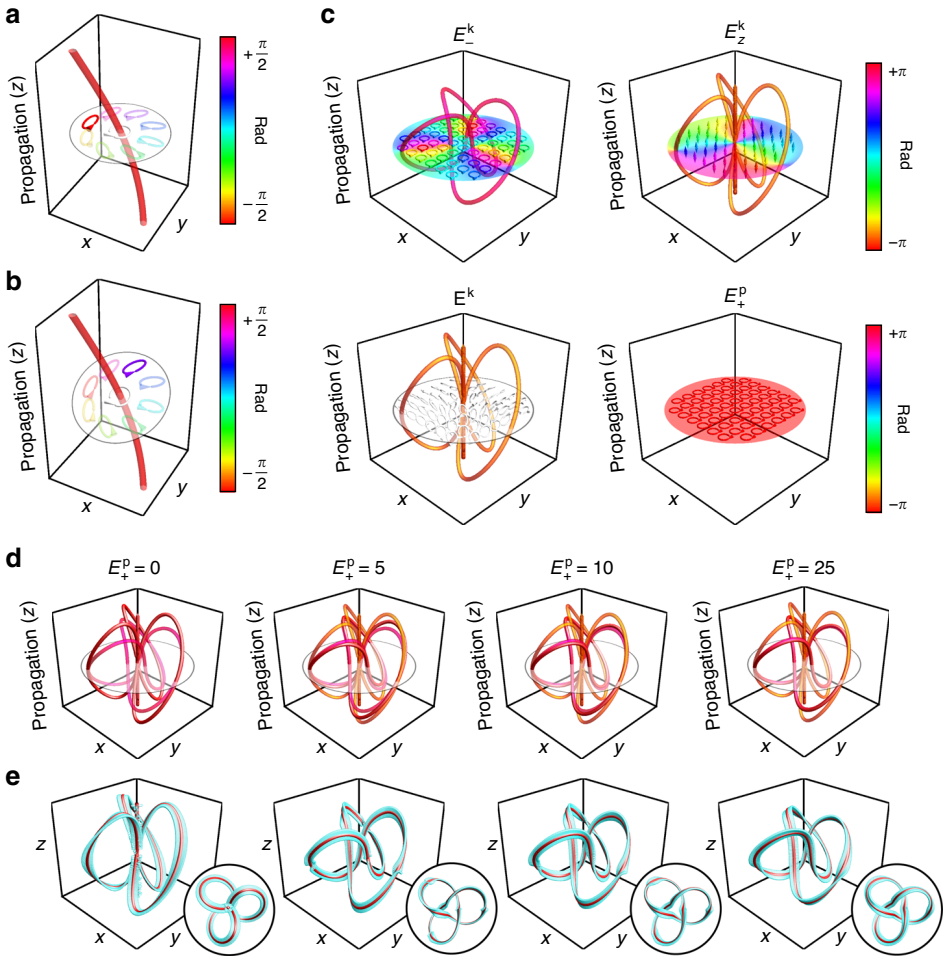

Fig. 1 Construction of framed knotted C-lines. Depiction of the polarization field in the proximity of a C-line when the normal of the polarization ellipse is **a** and is not **b** parallel to the beam's direction of propagation. Polarization ellipses with an axis perpendicular to the C-lines are displayed in bold colors and determine the orientation of the line's framing when it forms a closed loop. **c** Vector components of a framed optical knot, which include a circular component with knotted intensity nulls, E_-^k, accompanied by a longitudinal field, E_z^k, with nulls determined by the topology of E_-^k. These two components form a nonuniform polarization field $\mathbf{E}^k$ which can be shaped into a framed knotted C-line by means of a perturbing plane wave E_+^p. **d** Trajectory of the resulting knotted C-lines (red) overlaid onto the trajectories formed by the intensity nulls of E_-^k (pink) and E_z^k (orange) for various plane wave amplitudes. **e** Framed knot structures arising from the superpositions shown in **c** where the knotted C-line is shown in red and its frame is shown in cyan.

coordinates of each space map onto one another are provided in "Methods."

The above projection is heavily relied on when constructing knotted optical fields. In particular, a scalar optical field can be constructed by first matching its field along the $z = 0$ plane to that of the complex knot resulting from the projection of a braid as prescribed by Eq. (1). When this optical field is paraxial, then its formulation at subsequent z planes can be obtained by means of paraxial propagation methods[14]. This method can then be further extended to describe paraxial-knotted C-lines[21] and full vectorial solutions to the optical wave equation[34]. For instance, the knotted field E_-^k in Fig. 1c is fundamentally constructed based on the closure of a braid embedded within the zeros of a complex field[34].

Because of its wide usage in obtaining knots from braids, we have opted to use the projection defined in Eq. (1) to obtain structures with properties that can more easily be related to the braid representations of the optical-framed knots considered in this work. Namely, we consider the torus $\mathcal{T}_2$ obtained from the projection of the cylinder $\mathcal{C}$ enclosing the three-dimensional representation of the corresponding braid. Then, we scale the dimensions of our knots such that their structure fits within the proximity of $\mathcal{T}_2$. We later apply the coordinate transformation provided in "Methods" on those of a curve formed by a knotted C-line. This transformation effectively cuts the knot along a given azimuthal angle and unwraps it, thereby mapping the φ coordinate of the knot to the h coordinate of the space where the braid is defined. During this process, the orientation of the knot's frame is assured to be locally preserved. To illustrate this procedure, we apply it on the framed optical trefoil knot shown in Fig. 2e. The resulting unwrapped structure is displayed in Fig. 2f. From this transformation, information such as the twisting angle in the knots' braid representations can be extracted. Here, the twisting angle consists of the azimuthal orientation of the ribbon in the frame where the normal is aligned to the unwrapped knot's tangent. For instance, the twisting angle in each strand of the unwrapped knot shown in Fig. 2f can be found in Fig. 2g.

Prime encoding scheme. Given the ability to extract the twisting angle of an optical-framed knot, we propose the following scheme exploiting these structures as information carriers. The use of this method relies on a pair of numbers (α, β) where α is a positive integer, and β is a number both related to α and to the topological structure of the framed knot. The latter is given by

$$\beta = \prod_{\{k|d_k \neq -\infty\}} p_k^{\left(\alpha^{d_k - M}\right)}, \qquad (2)$$

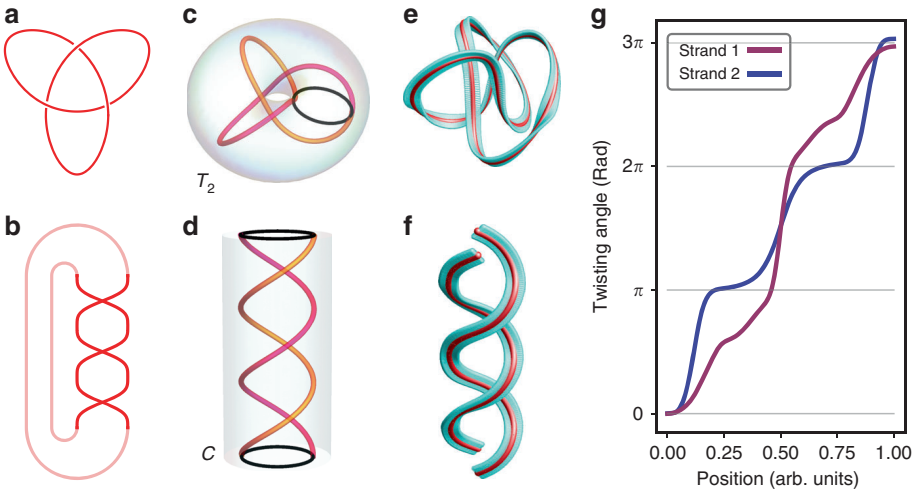

Fig. 2 Braid representation of knots. The diagram of a trefoil knot (**a**) along with its corresponding braid (**b**). Both ends of the braid diagram are connected to illustrate how its closure yields the knot in **a**. A trefoil knot (**c**) obtained from the stereographic projection of the braid in **d**. The projection effectively connects both ends of the braid, highlighted by a black outline, thereby transforming the two strands of the braid into a knot and the enclosing cylinder, $\mathcal{C}$, into a torus, $\mathcal{T}_2$. **e, f** An optical-framed knot (**e**) and its unwrapped form (**f**) obtained by applying a coordinate transformation on the curve formed by the knot while preserving the local orientation of the knot's frame. **g** Extracted twisting angle of the frame of the two strands in the structure shown in **f**.

where k refers to a strand in a braid representation of the considered framed knot. d_k is the number of half-twists along the kth strand exhibiting half-twists, i.e., $d_k = -\infty$ for untwisted strands. p_k is a prime number assigned to the kth strand. Finally, $M = \sum_k d_k$ consists of the total number of half-twists in the knot's frame. Further discussions exploring how α and β relate to braiding and twisting in framed braids are provided in Supplementary Notes 2 and 3. With these variables, we define the natural number

$$N_{\alpha,\beta}(M) \overset{\text{def}}{=} \beta^{(\alpha^M)} = \prod_{\{k|d_k\neq-\infty\}} p_k^{\left(\alpha^{d_k}\right)}, \tag{3}$$

whose prime factorization can be seen to be determined by the considered braid representation. Further details regarding this decomposition are provided in Supplementary Note 3.

The above representation of the framed knot and one of its braids may therefore be exploited for encoding and decoding topologically protected information as follows. Alice would like to send Bob a message which is here obtained as an output of a certain program running on some initial inputs, the set of numbers, d_k, $k = 1, 2, \ldots, n$. Running the program with this set is expected to yield Alice's message.

Alice conceives her program and its inputs as a framed braid. She identifies an operation with a sequence of crossings in the braid's planar diagram while the initial inputs are taken as the number of half-twists per strand. Alice has her program completely specified by the n-strand framed braid representation of a knotted ribbon K_A. To maintain some degree of privacy, she would like to send Bob K_A rather than the original framed braid. As further discussed in Supplementary Note 3 and implied in Fig. 3, she takes note of the fact that K_A may be complicated such as to conceal the original framed braid.

She then proceeds by performing the following steps. She first chooses a positive integer α. She then determines the framed braid representation of K_A. Doing so involves allocating the number of half-twists in K_A to different strands of the braid, i.e., setting d_k such that $M_A = \sum_k d_k$. Following this step, she assigns prime numbers p_k to strands exhibiting half-twists. Finally, she determines the number β according to Eq. (2). Once this allocation is completed, Alice proceeds by sending Bob her knotted ribbon K_A and the pair of numbers (α, β) in real time. Upon receiving these, Bob computes $N_{\alpha,\beta}(M_A)$ whose prime factorization unfolds d_k. To prevent the latter from being retrieved as an unordered set of integers, Alice and Bob rely on a previously adopted convention clarifying how the extracted d_k is assigned to distinct strands of the encoded braid. Bob can now recover the framed braid that was originally considered by Alice. For illustrative purposes, we summarize this protocol in Fig. 3.

Experimental generation. Motivated by this encoding scheme, we proceed with its application to paraxial-knotted C-lines generated in the following experiments. Such structures can be created by means of the folded Sagnac interferometer used in ref. [21], which is shown in Fig. 4a for convenience. This apparatus separates a uniformly polarized light beam into two orthogonally polarized components, each of which modulated by a spatial light modulator (SLM). The latter displays holograms in which both the intensity and the phase of the target optical field is encrypted[36]. One component is modulated to produce a beam featuring knotted optical vortices[14], such as E_-^k shown in Fig. 1c in the limit where non-paraxial effects are negligible. The other is modulated to form a large Gaussian beam that uniformly covers the entirety of the knotted component, thereby effectively taking the role of the plane wave E_+^p in Fig. 1c. Upon exiting the interferometer, the two beams are coherently added, thereby converting the knotted phase vortices of E_-^k into paraxial-knotted C-lines[21]. The knot and its frame can then be reconstructed with polarization tomography measurements[37] enabling one to obtain the field's polarization profile.

We use the above apparatus to produce both framed trefoil and cinquefoil knots. The holograms displayed on the SLM for this purpose are displayed in Fig. 4b along with the amplitude and phase of the fields that they are designed to generate. The latter are given in Eqs. (4) and (5) for the cases of the trefoil and cinquefoil knots, respectively,

$$\psi_{a,b,s}^{\text{Tref}}(\varrho,\varphi) = \left[1 - \varrho^2 - 4(a^2-b^2)\varrho^3 - \varrho^4 + \varrho^6 - 2(a-b)^2\varrho^3 e^{-3i\varphi} - 2(a+b)^2\varrho^3 e^{3i\varphi}\right] e^{-(\varrho/s)^2/2}, \tag{4}$$

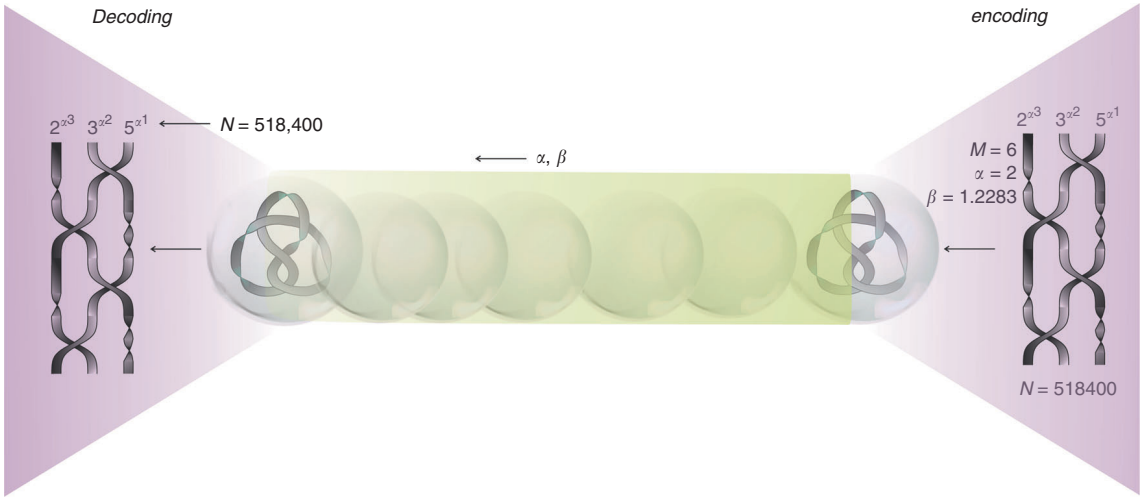

Fig. 3 Prime encoding scheme of framed braids. A framed braid on the right encodes a message—the output of a certain program specified by the planar diagram of the braid. In particular, the braid representation can be linked, as discussed below, to the prime factorization of a large integer N. An operation in such a program is identified with a sequence of crossings. Its inputs are taken as the number of half-twists per strand. To maintain privacy, the closure of the braid, i.e., the framed knot/knotted ribbon (in the case of even/odd number of half-twists, respectively), is transmitted instead of the braid itself. This allows the sender to complicate the message, if desirable, by adding an arbitrary number of Reidemeister-II and -III moves. The unique framed braid representation may be recovered on the receiver's end by transmitting two additional numbers, α and β, alongside with the knotted object. In this example, we chose for a simple elucidation $\alpha = 2$ and the first three primes $p_1 = 2$, $p_2 = 3$, $p_3 = 5$, one per strand in the braid (to showcase the scheme in the richer case of three strands, we preferred here the figure-eight knot, rather than the double-strand trefoil and cinquefoil knots). The corresponding numbers of half-twists in our example are $d_1 = 3$, $d_2 = 2$, and $d_3 = 1$, giving a total of $M = 6$ half-twists in the resulting framed knot. This is the topological invariant to be transmitted. The number β is subsequently computed according to Eq. (2). Once received (on the left) the framed knot can be associated with the previously encoded integer N; the number of half-twists M and the pair α and β are substituted into Eq. (3) to yield N, which here equals 518, 400. The prime factorization of N results from the actual number of half-twists per strand in the braid representation, $518,400 = 2^{2^3} \cdot 3^{2^2} \cdot 5^{2^1}$.

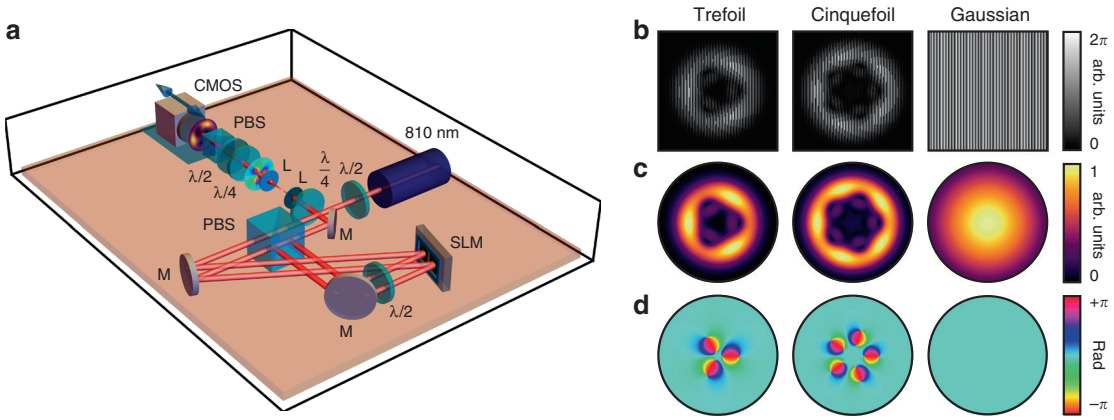

Fig. 4 Experimental generation of optical-framed knots. a Experimental apparatus used to generate optical-framed knots. An 810-nm laser produces light whose polarization is adjusted by a half-wave plate ($\lambda/2$) and later fed into a folded Sagnac interferometer. In the interferometer, the two polarized components are individually modulated by a spatial light modulator (SLM) and then coherently recombined to form an optical-framed knot. The latter is imaged using a 4f system, and then reconstructed by means of polarization tomography relying on a sequence of optical elements that include a quarter-wave plate ($\lambda/4$), a half-wave plate, a polarizing beam splitter (PBS), and a CMOS camera. Figure legend: mirror (M), L (lens). **b** Holograms used to generate framed knots, where knotted fields (trefoil and cinquefoil) are imprinted on the right-handed circular component of the optical field, and a Gaussian field is written on the left-handed component. **c** Amplitude and **d** phase of the fields generated by the corresponding holograms.

$$\psi^{\mathrm{Cinq}}_{a,b,s}(\varrho,\varphi) = \big(1+\varrho^2-2\varrho^4-16(a^2-b^2)\varrho^5 - 2\varrho^6+\varrho^8+\varrho^{10}-8(a-b)^2\varrho^5 e^{-5i\varphi} - 8(a+b)^2\varrho^5 e^{5i\varphi}\big]\, e^{-(\varrho/s)^2/2}, \quad (5)$$

where ϱ is a scaled and dimensionless version of the cylindrical radial coordinate, φ is the azimuthal coordinate, and a, b, s are parameters that determine the shape of the knot. For the trefoil knot, we considered parameters of $a = 1$, $b = 0.5$, and $s = 1.2$, whereas for the cinquefoil knot, we used $a = 0.5$, $b = 0.24$, and $s = 0.65$. These fields are obtained based on stereographic projection methods explored in ref. [35] and are further discussed in Supplementary Note 4. As discussed in the latter, the selected parameters enable the creation of shorter knots. Furthermore, as emphasized in Supplementary Note 5, the frame of these knots is less disrupted by noise in the position of the C-lines arising from experimental imperfections. The framed knots of these fields expected from theory are shown in Fig. 5a, whereas the knots generated in our experiments can be found in Fig. 5b. Aside from minor perturbations that arise where the C-lines are born and

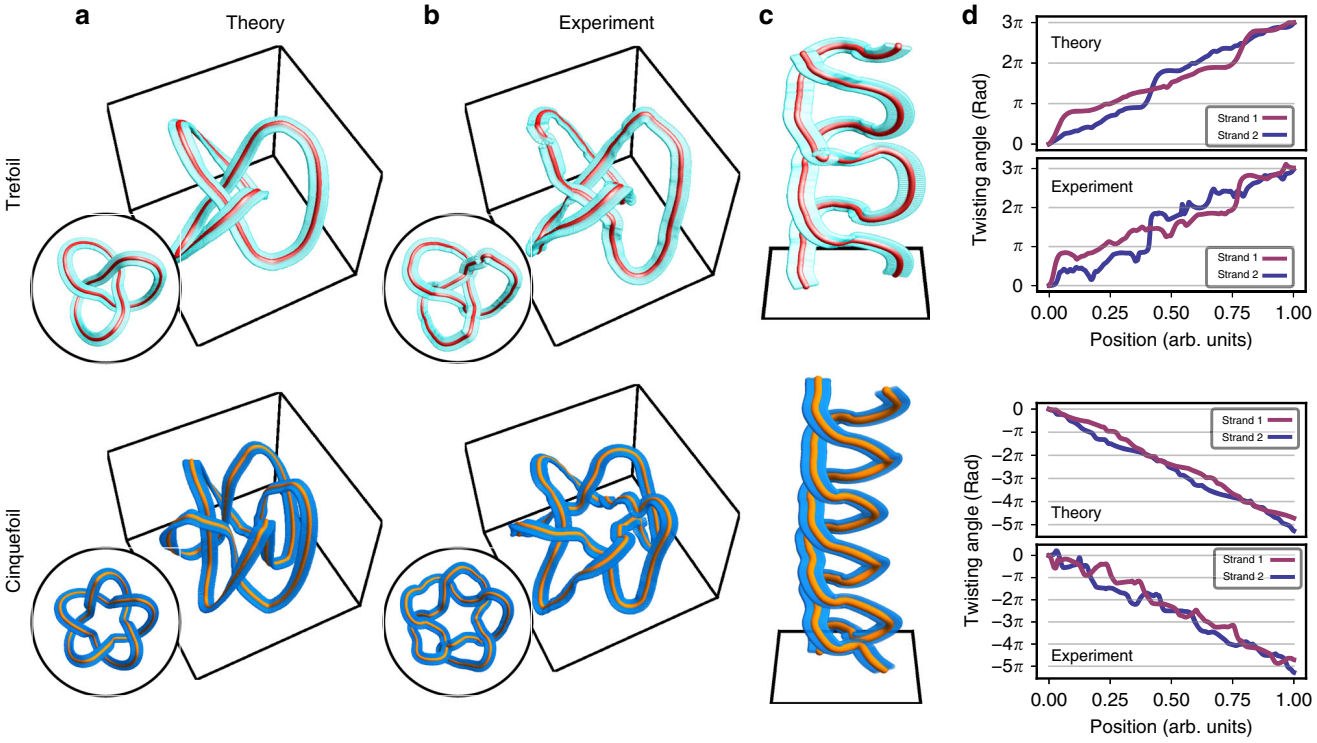

Fig. 5 Trefoil and cinquefoil optical-framed knots. a Optical-framed knots expected from theory attributed to the holograms displayed in Fig. 4. **b** Framed knots reconstructed from tomographic measurements of the beams generated by these holograms. **c** Unwrapped versions of the knots shown in **b**. **d** Twisting angle of the braid shown in **c** along with the values expected from theory.

annihilated at the knot's extremities, we observe that the knots' frames are in fairly good agreement with what is expected from theory. The unwrapped form of our experimental knots based on Eq. (1) is shown in Fig. 5c. We plot the corresponding twisting angle of these unwrapped knots along with the one expected from theory in Fig. 5d, where we observe once more that both strands in the structure are endowed with the same number of half-twists.

At this point, it is worth accentuating that the quantity of interest in Fig. 5d consists of the total twisting angle in the unwrapped knot. It might be tempting to treat the latter as one of the knot's braid representations. However, due to the knot's unwrapping, the number of half-twists in each strand may not exactly amount to an integer. Both ends of the braid are mapped from an azimuthal cross-section of the measured knot. Therefore, if the orientation of the frame at this cross-section is not the same for all parts of the knot, then the twisting angle of the strands in the unwrapped knot will not strictly amount to integer multiples of π. However, the sum of the twisting angles in each strand will amount to such a multiple given that the knot is a closed structure. This physical trait, in conjunction with the aforementioned (α, β) pair, in turn allows us to formulate the properties of the braid under consideration, which, for our purposes, consists of a purely algebraic entity. By taking this consideration into account and following the scheme outlined in Fig. 3, the knotted structures illustrated in Fig. 5 along with a given choice of (α, β) can be used to encode a braid representation of these knots.

Discussion

The above generation and detection schemes can be extended to deal with non-paraxial optical knots. In practice, this extension would be achieved through the use of tight-focusing lenses and more sophisticated forms of polarization tomography[38]. As implied in Fig. 1, one could prospectively exercise further control over the C-line's frame with the presence of a stronger longitudinal polarization in the electric field. Furthermore, non-paraxial methods would enable the generation of knots with a more manageable longitudinal extent. Indeed, a wealth of structures, including the trefoil and cinquefoil knots investigated here, are predicted to form over a distance comparable to the optical field's wavelength[34].

In practice, the act of sending information encoded within knotted C-lines by means of the scheme presented in this work could be achieved with an apparatus similar to the one presented in Fig. 4. The act of encoding information would be performed with the folded Sagnac interferometer enclosing the SLM and potentially other optics. Once the optical field is imbued with its knotted properties, it is then transmitted to a location where it can be decoded by means of an imaging system consisting of the two lenses shown in the setup. Finally, information is decoded from the field by means of the reconstruction techniques presented in this work, i.e., polarization tomography, to reconstruct the knot followed by a coordinate transformation to extract the corresponding braid. One could argue that the entirety of this information could be extracted from a single plane measurement of the field's properties, which would then enable the knot's reconstruction based on its theoretical propagation as prescribed by the optical wave equation. However, as alluded to in several parts of this work, sources of experimental imperfections such as aberrations, which have long been known to affect the topology of structured light beams[39], may potentially complicate such an approach. Namely, a full account of the aberrations and errors introduced by our interferometric setup would be needed to enable a full field reconstruction. This complication thereby encourages the use of the more direct reconstruction approach reported here.

To summarize, we introduced a construct for framed knots within optical polarization knots. This construct relies on the presence of knotted C-lines within the considered wavefield. Due to the singular nature of the axis of the polarization ellipse surrounding these lines, a frame can be assigned to the knot based on

its trajectory and the oscillation plane of the polarization ellipse along the C-line. Through the use of a coordinate transformation along with an encoding scheme relying on the braid representation of framed knots, we demonstrate how paraxial-knotted C-lines produced in experiments can be employed as information carriers. More specifically, we have shown that the braid representation of framed knots can be employed for encoding and decoding topologically invariant information such as the number of half-twists, as demonstrated above, being related to the prime factorization of large integers. It is expected that other topological invariants like the Alexander and Jones polynomials could consist of other encoded properties. The full potential of this scheme could be investigated by its application to more sophisticated knotted structures[35], such as experimentally generated figure-eight knots[21]. In addition, further engineering of the knot's frame through the use of non-paraxial structures[34,40] could be used to apply different numbers of half-twists within the knot. The generation of these more complex topologies may also be of interest in other applications relying on framed knots, such as quantum money[41,42]. On a more fundamental level, the methods outlined here may be of interest in quantifying and encoding the topological properties of more complex types of knots such as those that could be formed by the singularities in knotted tangles within random polarization fields[43] or speckle fields[5,44].

Methods

Coordinate mapping for the braid extraction of knots. To unwrap the considered knots, we rely on the stereographic projection discussed in the main text. Based on the dependence of the complex variables (u, v) on the spatial coordinates of the space in which the braid and knot are defined, which are respectively denoted as (x, y, h) and (ρ, φ, z), one can establish the following relation between both sets of coordinates

$$x \mapsto \frac{\rho^2 + z^2 - 1}{\rho^2 + z^2 + 1}, \tag{6}$$

$$y \mapsto \frac{2z}{\rho^2 + z^2 + 1}, \tag{7}$$

$$h \mapsto \varphi, \tag{8}$$

where (x, y, h) and (ρ, φ, z) refer to Cartesian and cylindrical coordinate systems, respectively.

Generation of optical-framed knots. The generation of the knotted structures presented in this work relies on the method used in ref. [21]. As illustrated in Supplementary Fig. 1, an 810-nm laser is first coupled to free space where it later goes through a half-wave plate and a polarizing beam splitter (PBS) to modulate its intensity. It then goes through another half-wave plate in order to put the beam in an equal superposition of horizontal and vertical polarization components. The beam then goes through a folded Sagnac interferometer, which first separates each component with a PBS. In the interferometer, each polarization component is individually modulated by a SLM (Holoeye, Pluto Series) with the holograms shown in Fig. 4b. A half-wave plate is inserted within the interferometer to ensure that both components have the polarization that allows them to be modulated by the SLM. One of these components acquires a profile with knotted phase vortices[14] whereas the other acquires a large Gaussian profile. The two parts of the beam are then recombined at the exit of the interferometer where they are converted to circular polarizations by means of a half-wave plate (not shown in Fig. 4a) followed by a quarter-wave plate. In practice, this conversion can be achieved with only a quarter-plate as shown in Fig. 4a. However, we opted for the inclusion of the half-wave plate as it compensated for the effects of our dielectric mirrors on our beam's polarization, which needed to be introduced in our setup due to spatial constraints. As shown in ref. [21], converting the two polarizations to the circular polarization basis enables the conversion of knotted phase vortices into knotted C-lines.

The holograms provided in Eqs. (4) and (5) are expressed in terms of a dimensionless radial coordinate $\varrho = \rho/w_0$, where ρ is the radial coordinate and w_0 is a scaling parameter. The w_0 values used to generate the knots shown in Fig. 4 were 0.35 mm for the trefoil knot and 0.42 mm for the cinquefoil knot.

Measurement procedure. We reconstruct the polarization field formed by the knotted C-lines by means of tomographic polarization measurements[37] at 40 planes spread out across the longitudinal extent of the knot. These measurements include six polarization projections along the horizontal, vertical, diagonal, anti-diagonal, left- and right-handed circular polarizations. As shown in Supplementary Fig. 1 and depicted in Fig. 4a, the polarization projections are performed with a quarter-wave plate, followed by a half-wave plate, and then a PBS. The projections themselves correspond to the average of six frames recorded with a CMOS camera (Thorlabs DCC1645C).

Our choice of w_0 resulted in knots with an experimental longitudinal extent of 66 and 58 cm for the trefoil and cinquefoil knots, respectively. Measurement planes were separated by 1.5 cm while acquiring data for the trefoil knot whereas they were separated by 2 cm for the cinquefoil knot.

Framed knot reconstruction. Sources of image degradation in the polarization measurements, such as speckles of dust on the camera, are first removed by making the recorded measurements go through a non-aggressive low-pass filter. The processed images are then used to extract the beam's first, second, and third Stokes parameters, s_1, s_2, and s_3. The latter are employed to reconstruct the polarization profile of the knotted field at 40 planes transverse to the beam's propagation. As performed in ref. [21], the location of the C-lines along these planes is then determined by finding contour intersections in the phase of the field formed by $s_1 + is_2$. The transverse locations of the C-lines at each plane are then connected to provide the knot formed by the beam's polarization field. In order to smooth out numerical noise arising from the discretization of the CMOS images used to obtain the knot, a Gaussian filter with a width of 1 pixel is applied on the knot's transverse coordinates, i.e., x and y. Spline interpolation is then used to estimate the knot's location outside of the considered transverse planes. The orientation of the frame of the knot is then extracted by taking the cross product between the gradient of the knot's coordinates and the normal vector of the C-line's oscillation plane. For the paraxial knots considered in our experiments, this orientation corresponds to the direction of propagation of the beam. More detailed discussions regarding the data processing involved in the reconstruction of the framed knot are provided in Supplementary Note 6.

Data availability

The data that support the findings of this study are available from the corresponding author upon reasonable request.

Code availability

The code producing the figures is available from the corresponding author upon reasonable request.

Received: 17 December 2019; Accepted: 8 September 2020;
Published online: 09 October 2020

References

1. Rubinsztein-Dunlop H. et al. Roadmap on structured light. *J. Opt.* **19**, 013001 (2016).
2. Dennis, M. R., O'Holleran, K. & Padgett, M. J. Singular optics: optical vortices and polarization singularities. in *Progress in Optics,* Vol. 53 (ed. Wolf, E.), 293–363 (Elsevier, Amsterdam, 2009).
3. Soskin, M., Boriskina, S. V., Chong, Y., Dennis, M. R. & Desyatnikov, A. Singular optics and topological photonics. *J. Opt.* **19**, 010401 (2017).
4. Nye, J. F. & Berry, M. V. Dislocations in wave trains. *Proc. Roy. Soc. A* **336**, 165–190 (1974).
5. Flossmann, F., Kevin, O., Dennis, M. R. & Padgett, M. J. Polarization singularities in 2D and 3D speckle fields. *Phys. Rev. Lett.* **100**, 203902 (2008).
6. Allen, L., Beijersbergen, M. W., Spreeuw, R. & Woerdman, J. Orbital angular momentum of light and the transformation of Laguerre-Gaussian laser modes. *Phys. Rev. A* **45**, 8185–8189 (1992).
7. Freund, I. Optical möbius strips in three-dimensional ellipse fields: I. lines of circular polarization. *Opt. Commun.* **283**, 1–15 (2010).
8. Freund, I. Multitwist optical möbius strips. *Opt. Lett.* **35**, 148–150 (2010).
9. Bauer T. et al. Observation of optical polarization möbius strips. *Science* **347**, 964–966 (2015).
10. Bauer, T., Neugebauer, M., Leuchs, G. & Banzer, P. Optical polarization möbius strips and points of purely transverse spin density. *Phys. Rev. Lett.* **117**, 013601 (2016).
11. Bauer T. et al. Multi-twist polarization ribbon topologies in highly-confined optical fields. *New. J. Phys.* **21**, 053020 (2019).
12. Berry, M. V. & Dennis, M. R. Knotted and linked phase singularities in monochromatic waves. *Proc. R. Soc. A* **457**, 2251–2263 (2001).
13. Leach, J., Dennis, M. R., Courtial, J. & Padgett, M. J. Knotted threads of darkness. *Nature* **432**, 165–165 (2004).
14. Dennis, M. R., King, R. P., Jack, B., O'Holleran, K. & Padgett, M. J. Isolated optical vortex knots. *Nat. Phys.* **6**, 118–121 (2010).

15. Pisanty E. et al. Knotting fractional-order knots with the polarization state of light. *Nat. Photon.* **13**, 569–574 (2019).
16. Ranada, A. F. Topological electromagnetism. *J. Phys. A* **25**, 1621 (1992).
17. Ranada, A. F. & Trueba, J. L. Electromagnetic knots. *Phys. Lett. A* **202**, 337–342 (1995).
18. Irvine, W. T. & Bouwmeester, D. Linked and knotted beams of light. *Nat. Phys.* **4**, 716–720 (2008).
19. Irvine, W. T. Linked and knotted beams of light, conservation of helicity and the flow of null electromagnetic fields. *J. Phys. A* **43**, 385203 (2010).
20. Kedia, H., Bialynicki-Birula, I., Peralta-Salas, D. & Irvine, W. T. Tying knots in light fields. *Phys. Rev. Lett.* **111**, 150404 (2013).
21. Larocque H. et al. Reconstructing the topology of optical polarization knots. *Nat. Phys.* **14**, 1079–1082 (2018).
22. Erhard, M., Fickler, R., Krenn, M. & Zeilinger, A. Twisted photons: new quantum perspectives in high dimensions. *Light: Sci. Appl.* **7**, 17146 (2018).
23. Wang, J. et al. Terabit free-space data transmission employing orbital angular momentum multiplexing. *Nat. Photon.* **6**, 488–496 (2012).
24. Sit A. et al. High-dimensional intracity quantum cryptography with structured photons. *Optica* **4**, 1006–1010 (2017).
25. Adams, C. C. The knot book: an elementary introduction to the mathematical theory of knots (American Mathematical Soc., 2004).
26. Freedman, M. H., Kitaev, A. & Wang, Z. Simulation of topological field theories by quantum computers. *Commun. Math. Phys.* **227**, 587–603 (2002).
27. Freedman, M., Kitaev, A., Larsen, M. & Wang, Z. Topological quantum computation. *Bull. Am. Math. Soc* **40**, 31–38 (2003).
28. Kitaev, A. Y. Fault-tolerant quantum computation by anyons. *Ann. Phys.* **303**, 2–30 (2003).
29. Garnerone, S., Marzuoli, A. & Rasetti, M. Quantum geometry and quantum algorithms. *J. Phys. A* **40**, 3047–3066 (2007).
30. Nayak, C., Simon, S. H., Stern, A., Freedman, M. & Sarma, S. D. Non-abelian anyons and topological quantum computation. *Rev. Mod. Phys.* **80**, 1083–1159 (2008).
31. Romero J. et al. Entangled optical vortex links. *Phys. Rev. Lett.* **106**, 100407 (2011).
32. Kleckner, D. & Irvine, W. T. Creation and dynamics of knotted vortices. *Nat. Phys.* **9**, 253–258 (2013).
33. Nye, J. F. & Hajnal, J. The wave structure of monochromatic electromagnetic radiation. *Proc. R. Soc. A* **409**, 21–36 (1987).
34. Sugic, D. & Dennis, M. R. Singular knot bundle in light. *J. Opt. Soc. Am. A* **35**, 1987–1999 (2018).
35. Bode, B., Dennis, M. R., Foster, D. & King, R. P. Knotted fields and explicit fibrations for lemniscate knots. *Proc. R. Soc. A* **473**, 20160829 (2017).
36. Bolduc, E., Bent, N., Santamato, E., Karimi, E. & Boyd, R. W. Exact solution to simultaneous intensity and phase encryption with a single phase-only hologram. *Opt. Lett.* **38**, 3546–3549 (2013).
37. Cardano F. et al. Polarization pattern of vector vortex beams generated by q-plates with different topological charges. *Appl. Opt.* **51**, C1–C6 (2012).
38. Bauer, T., Orlov, S., Peschel, U., Banzer, P. & Leuchs, G. Nanointerferometric amplitude and phase reconstruction of tightly focused vector beams. *Nat. Photon.* **8**, 23–27 (2014).
39. Leach, J., Yao, E. & Padgett, M. J. Observation of the vortex structure of a non-integer vortex beam. *New J. Phys.* **6**, 71 (2004).
40. Maucher, F., Skupin, S., Gardiner, S. & Hughes, I. Creating complex optical longitudinal polarization structures. *Phys. Rev. Lett.* **120**, 163903 (2018).
41. Farhi, E., Gosset, D., Hassidim, A., Lutomirski, A. & Shor, P. Quantum money from knots. In *Proc. 3rd Innovations in Theoretical Computer Science Conference*, 276–289 (2012).
42. Aaronson S. et al. Quantum money. *Commun. ACM* **55**, 84–92 (2012).
43. Taylor, A. J. & Dennis, M. R. Vortex knots in tangled quantum eigenfunctions. *Nat. Commun.* **7**, 12346 (2016).
44. Padgett, M. J., O'Holleran, K., King, R. P. & Dennis, M. R. Knotted and tangled threads of darkness in light beams. *Contemp. Phys.* **52**, 265–279 (2011).

Acknowledgements

This work was supported by Ontario's Early Research Award (ERA), Canada Research Chairs (CRC), and Canada First Research Excellence Fund (CFREF) Program. H.L. acknowledges the support of the Natural Sciences and Engineering Research Council of Canada (NSERC).

Author contributions

H.L. designed the holograms used to generate the knots. H.L. and A.DE. performed the experiment. H.L. and A.DE. analyzed the data. H.L. and M.F.F-.G. performed the numerical simulations. A.C. and E.C. developed the prime encoding protocol. A.C., E.C., and E.K. supervised all aspects of the project. All authors discussed the results and contributed to the text of the manuscript.

Competing interests

The authors declare no competing interests.

Additional information

Supplementary information is available for this paper at https://doi.org/10.1038/s41467-020-18792-z.

Correspondence and requests for materials should be addressed to H.L. or E.K.

Peer review information *Nature Communications* thanks Ching Hua Lee and the other, anonymous, reviewers for their contribution to the peer review of this work. Peer reviewer reports are available.

Reprints and permission information is available at http://www.nature.com/reprints

Publisher's note Springer Nature remains neutral with regard to jurisdictional claims in published maps and institutional affiliations.

Secure communication using low dimensional topological elements

Manuel F. Ferrer-Garcia,[1] Avishy Carmi,[2] Alessio D'Errico,[1] Hugo Larocque,[3] Eliahu Cohen,[4] and Ebrahim Karimi[1]

[1]*Nexus for Quantum Technologies, University of Ottawa, Ottawa, K1N 6N5, ON, Canada*
[2]*Center for Quantum Information Science and Technology and the Faculty of Engineering Sciences, Ben-Gurion University of Negev, Beersheba, Israel*
[3]*Research Laboratory of Electronics, Massachusetts Institute of Technology, Cambridge, MA 02139, USA*
[4]*Faculty of Engineering and the Institute of Nanotechnology and Advanced Materials, Bar-Ilan University, Ramat Gan, Israel*

Low-dimensional topological objects, such as knots and braids, have become prevalent in multiple areas of physics, such as fluid dynamics, optics and quantum information processing. Such objects also now play a role in cryptography, where a framed knot can store encoded information using its braid representation for communications purposes. The greater resilience of low-dimensional topological elements under deformations allows them to be employed as a reliable framework for information exchange. Here, we introduce a challenge-response protocol as an application of this construction for authentication. We provide illustrative examples of both procedures showing how framed links and braids may help to enhance secure communication.

I. INTRODUCTION

Alexandre-Théophile Vandermonde was intrigued by knots and discussed their topological features in 1771. Later, in 1833, Carl Friedrich Gauss showed that the numerical invariant called today the linking number (representing the number of times that each curve winds around the other) can be calculated by an integral. Lord Kelvin's[1] attempt to develop a theory of fluids and solids based on microscopic vortex knots further stimulated the efforts to develop a rigorous mathematical theory of knots, links and braids. After Kelvin's atomic theory was abandoned, the research on knots developed separately from physics as a purely mathematical subject, with remarkable achievements as topology was extensively developed in the 20th century[2]. Nowadays, knot theory has already reappeared in several areas of physics. Knot theory offers novel calculating tools, e.g. for exactly evaluating the partition function in vertex models[3] of statistical physics, in quantum field theory, especially concerning the study of Chern-Simons actions, of interest in both high energy and condensed matter physics[4], in topological fluid dynamics[5], for instance, in the study of energy minimization of linked vortex tubes[6], in quantum information theory, particularly concerning topological quantum computation[7–9], in electromagnetism, where knotted solutions of the Maxwell's equations have been discovered[10–12], and in optics[13,14]. Knots and braid structures can be observed in a large variety of physical systems. They emerge from vortex lines in fluids, including cholesteric liquid crystals[15] and Bose-Einstein condensates[16], or from the interference of acoustic[17,18] or optical waves in three-dimensions[19], or when appropriate boundary conditions are imposed on paraxial light beams[13,20]. Knots and braidings can be observed or engineered in complex molecular structures, as proteins or DNA chains[21].

The topological nature of these structures hints at their use for robust information distribution and manipulation. Candidate applications range from the above-mentioned topological quantum computing with non-Abelian anyons, to implementation of quantum money[22], to alternative encodings of classical information. We proposed the latter in Ref.[23], where we showed how specific optical paraxial beams are physical realizations of knotted ribbons (or framed knots). On such structures, numbers can be associated, not only with braiding operations, but also with the ribbon's twisting. From this representation, we proposed a prime encoding scheme. Alternative physical implementations based on nested knots generated from polychromatic optical fields have been proposed[24]. Here, we review the prime encoding in knotted ribbons scheme in more detail and generalize it to a full "RSA-like" key-distribution protocol.

Geometrically, it is possible to describe a braid in s-strands, or s-braid, as a collection of s non-intersecting strings joining two parallel planes. In physics, these low-dimensional topological elements have become relevant in the context of anyon-based topological quantum computing[25]. While braids are fascinating mathematical objects by themselves, we focus our interest on their connection with knots and links. Figure 1 illustrates that by tying the endpoints of the strands in a braid, one or more closed-knotted curves are obtained. Inversely, Alexander's braiding theorem states that every knot or link can be represented by the closure of a braid[26]. It must be noted that the closure mapping is surjective: a knot may admit multiple different – although equivalent – braid representations. A framed knot is an extension of classical knots, which arise from equipping the curves with a vector field normal to the curve at any point. This vector field is allowed to twist – 2π-rotations – around the curve[28]. Therefore, we can visualize a framed knot as a tangled ribbon whose ends have been glued together after being twisted several times. As in the previous case, i.e. knots, it is possible to construct a framed braid representation for any framed knot or link. However, we encounter an irreducible arbitrariness in the construction of the braid representation. There is more than one way to specify a framing for a braid from which a particular knotted ribbon is formed.

In this Article, we introduce the use of low-dimensional elements – framed knots and their corresponding braid representation – as a reliable platform for secure communications. Low-dimensional elements exhibit greater resilience to environmental disturbances than conventional data structures[29]. Therefore, the information content – the myriad of topological invariants – is generally insensitive to many deformations occurring when topological objects are material-

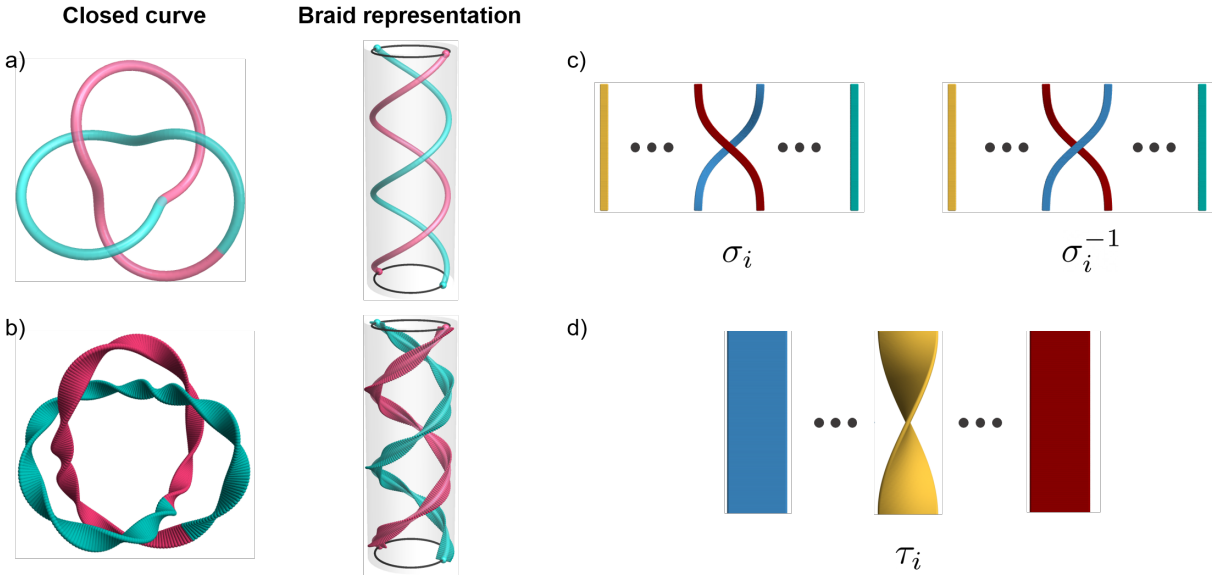

Figure 1. **Brief description of braids and knots. a.** A classical knot can be understood as a possible configuration of a tangled string in space. The closure of a braid representation can yield any classical knot. **b.** A framed knot (K, V) is visualized as a knotted ribbon with an even number of twists, and thus, framed knots are always orientable surfaces. **c.** The set of braid representations with s strands forms the Artin braid group $\mathcal{B}_s$ under the braiding operator σ_i[27], which indicates the position exchange of the i-th and $(i+1)$-th strands in the braid. **d.** For a framed-knot, it is necessary to define another operator, τ_i, to represent a single half-twist in the i-th strand.

ized and handled. We further develop the encoding of prime numbers using the braid representation and the half-twists per strand. The privacy of our message is achieved when the knot is closed. Therefore, our protocol relies not only on the difficult endeavor of prime factorization but also on the non-unique framed braid representation admitted by a knot.

II. ENCODING PRIME NUMBERS IN A FRAMED BRAID

A framed knot (K, V) is obtained when we equip a knot K with a continuous non-vanishing vector field V normal to the curve at all points, referred to as *framing*. Thus, it is possible to define an equivalent class for a framed knot using the framing integer M, i.e. the total number of half-twists. Since a framed knot (K, V) may admit multiple braid representations, the braid representation is not unique, and the closure of a framed braid may act as an operation to encode information. Nevertheless, the message can be recovered only if the receiver is able to reconstruct the correct braid representation.

Let us start by considering a framed s-braid representation, in which each strand is identified by an index k. We can define d_k as the number of half-twists along the k-th strand exhibiting half-twists. If we assign a *distinct* prime number p_k to each strand in our braid, then the framed s-braid as a whole captures the prime factorization of a natural number,

$$N = \prod_{\{k|d_k \neq -\infty\}} p_k^{(\alpha^{d_k})}, \tag{1}$$

where α is a real number chosen arbitrarily, (we point out that α is not related to any feature of the knot), and we assign $d_k = -\infty$ for untwisted strands. Note that the framing integer of the underlying framed knot obtained by the closure of the braid is given by $M = \sum_{\{k|d_k \neq -\infty\}} d_k$. In addition, we introduce a second quantity, which will be needed to construct the topological invariant of the braid representation,

$$\beta = \prod_{\{k|d_k \neq -\infty\}} p_k^{(\alpha^{d_k - M})}, \tag{2}$$

which permits us to write the number of twists in the braid representation as

$$M = \log_\alpha \left(\sum_{\{k|d_k \neq -\infty\}} \alpha^{d_k} \log_\beta p_k \right). \tag{3}$$

Using these expressions, Eqs. (1), (2) and (3), we can rewrite the natural number N as

$$N_{\alpha,\beta}(M) = \beta^{(\alpha^M)}. \tag{4}$$

In the latter expression, it becomes evident that N is determined exclusively by the total number of twists in the framed knot, M, and the pair (α, β). Therefore, $N_{\alpha,\beta}(M)$ is a topological invariant of the knotted ribbon. By comparing Eq. (1) and Eq. (4), it comes to light that the prime factorization of $N_{\alpha,\beta}(M)$ encodes the number of half-twists per strand in the frame braid representation of the knotted ribbon.

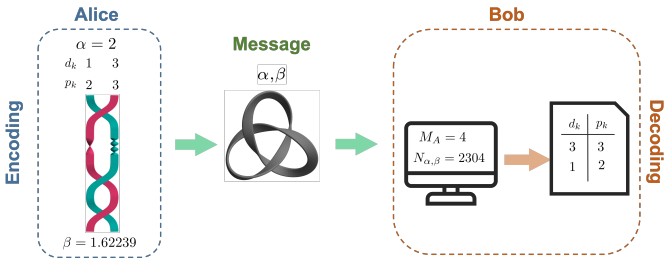

Figure 2. **Encoding mechanism of prime numbers in framed braids.** Alice generates both the set of twists per strand and the prime numbers associated with each strand. After choosing α, she computes β and closes her braid, obtaining the knot K_A. Then, she sends her message composed of the pair of numbers (α, β) alongside the framed knot. Then Bob proceeds to calculate the natural number $N_{\alpha,\beta}(M)$ and computes its prime factorization. The number of half-twists per strand can be obtained by employing Eq. (1).

III. SHARING INFORMATION USING KNOTTED RIBBONS

Given the relationship between the braid representation of a framed knot and the prime factorization, we propose the following scheme to share information *securely*. A protocol sketch is depicted in Fig. 2. Let us consider a scenario where Alice decides to send a message to Bob. The message is computed from initial inputs, i.e., a set of integers d_k where $k = 1, 2, \ldots, s$. In our case, Alice's message is encoded using a framed s-braid such that $\{d_k\}$ represent the half-twist number per strand. The procedure followed by Alice, illustrated in Fig. 2, can be summarized as follows:

1. Alice determines the set of numbers d_k that she wants to send to Bob. Therefore, the number of strands s in her braid representation is given by the length of $\{d_k\}$. In our example, the corresponding integers are $d_1 = 1$ and $d_2 = 3$, , leading to the total number of half-twists $M = 4$.

2. Alice allocates different prime numbers p_k to each of the strands in the braid. For the sake of simplicity, we have used the first two prime numbers $p_1 = 2$ and $p_2 = 3$.

3. Then, she applies multiple braiding operators and closes the framed braid to obtain the knotted ribbon K_A. In this case, we opted for a trefoil knot.

4. At the same time, she chooses a positive number α and computes β using Eq. (2). In our example, we set $\alpha = 2$, yielding to a $\beta = 2^{2^{-3}} \cdot 3^{2^{-1}} \approx 1.62239$.

Then, Alice sends a package containing the K_A and the pair (α, β) to Bob. Upon receiving these, Bob computes $N_{\alpha,\beta}(M)$ using Eq. (4) and its prime factorization. From here, Bob can retrieve $\{d_k\}$ and reconstruct an equivalent framed s-braid to the one sent by Alice. In our example, $N_{\alpha,\beta}(M) = 2304$ and its prime factorization yields $2304 = 2^8 \cdot 3^2$.

Before continuing, it is useful to emphasize some subtleties in the protocol. First, it must be noted that the type of knot obtained from the closure of the generated braid has no impact on the encoding mechanism. However, the privacy of the encoding arises from the fact that a framed knot may admit multiple equivalent braid representations. If an eavesdropper intercepts the message, they should guess the number of braids and the way the half-twists are distributed among them. Alongside this, our encoding protocol exploits the difficulty of the prime factorization task, which has been a hard problem to solve on a classical computer. This implies that, when the prime numbers are sufficiently large, there is no efficient general algorithm that can perform the computation[30].

IV. CHALLENGE-RESPONSE PROTOCOL USING FRAMED LINKS

Before continuing with an additional application, let us explore some properties of the topological invariant $N_{\alpha,\beta}(M)$ in the context of linked knots. We consider two framed knots, K_A and K_B, whose total number of half-twists is M_A and M_B, respectively. Then, suppose we connect the two knots forming the framed link $K_A \& K_B$ (See Figure 3). A natural question arises at this stage: how does the topological invariant $N_{\alpha,\beta''}(M_{A\&B})$ of the link relates to the ones from the individual knots $N_{\alpha,\beta}(M_A)$ and $N_{\alpha,\beta'}(M_B)$? It can be readily verified using Eq. (1) that the number associated with the framed link can be written as

$$N_{\alpha,\beta''}(M_{A\&B}) = N_{\alpha,\beta}(M_A) N_{\alpha,\beta'}(M_B) \tag{5}$$

as long $N_{\alpha,\beta}(M_A)$ and $N_{\alpha,\beta'}(M_B)$ are co-prime. This is possible if and only if a different prime factor is assigned to each strand in the individual knots forming the link.

In this spirit, we assume that both Alice and Bob can generate and reconstruct framed knots. Now, Bob is trying to access a service managed by Alice. For security reasons, Alice challenges Bob to perform some non-trivial calculations. If Bob's response is valid, Alice grants access to him. For that reason, the challenge-response authentication protocol goes as follows.

- Alice generates and sends K_A and the pair (α, β) to Bob. For the sake of simplicity, we assume she chooses a braid with 2 strands and assigns the first two prime numbers $p_1^A = 2$ and $p_2^A = 3$, correspondingly. In addition, she allocates $d_1^A = 3$ and $d_2^A = 1$ half-twists on the framed strands and closes the braid to create a trefoil knot K_A. Here, $\alpha = 2$, while the computation of β yields 1.62239.

- Subsequently, Bob computes $N_{\alpha,\beta}(M_A) = 2304$ from which he can obtain the prime factors in Alice's framed braid, p_k^A, $k = 1, 2, \ldots$.

- To generate his response knot K_B, Bob generates two new sets of numbers; the first one is a set of prime numbers $\{p_1^B = 5, p_2^B = 7\}$ that are different from the ones provided by Alice and follow the condition

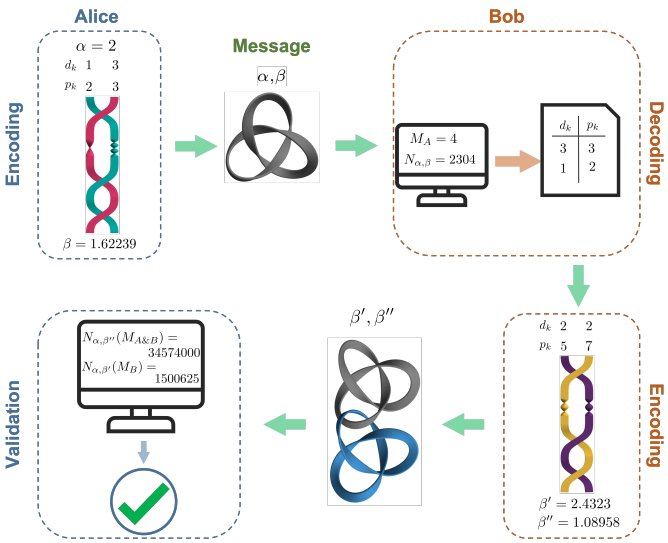

Figure 3. **Challenge-response algorithm.** After Bob requests access to a service, Alice sends a message that contains a framed knot K_A and the pair of numbers (α, β). Upon reception, Bob reconstructs Alice's braid representation. From here, he builds his own braid representation and makes sure that he assigns prime factors different from the ones sent by Alice. Before closing his braid, he links his knot K_B to K_A, generating the link $K_A\&K_B$. Subsequently, he generates the message containing the link $K_A\&K_B$ and the pair (β', β''), which are calculated using Eq.(2) from K_B and $K_A\&K_B$, respectively. Alice calculates the topological invariant $N_{\alpha,\beta''}(M_{A\&B})$ for the link and N_B and verifies if Bob's answer is correct using Eq.(5).

$p_j^B < N_{\alpha,\beta}(M_A)$, the second set of numbers corresponds to the number of twists per strand in his braid representation. Here, he chooses $d_1^B = d_2^B = 2$.

- Based on this, he generates his knot K_B and computes the corresponding $\beta' = 2.4323$. Before sending his answer to Alice, he creates the link $K_A\&K_B$ and calculates β" = 1.0895. Finally, Bob's answer to the challenge is a package that includes β', β" and the link $K_A\&K_B$.

According to Eq. (5), Alice should be able to compute $N_{\alpha,\beta'}(M_B)$ as $N_{\alpha,\beta''}(M_{A\&B})/N_{\alpha,\beta}(M_A)$. To verify that this number is indeed co-prime to $N_{\alpha,\beta}(M_A)$, she might attempt to divide it by any of her factors. This approach may nevertheless be time-consuming for large integers (the time complexity for calculating the totient function $\varphi(x)$ is currently known to scale no better than $\sqrt{x}$). Alternatively, Bob could include an integer defined as

$$\gamma = b^{\varphi(N_{\alpha,\beta'}(M_B))} \bmod N_{\alpha,\beta''}(M_{A\&B})$$

where b is co-prime to $N_{\alpha,\beta''}(M_{A\&B})$, $\varphi(x)$ is Euler's totient function and mod stands for the modulus function. Computing the totient function $\varphi(x)$ may be time consuming for a large x. Nevertheless, it is readily computed given x's prime factors, i.e., $\varphi(x) = \prod_{k=1}^{n}(p_k^{j_k} - 1)$, where $x = \prod_{k=1}^{n} p_k^{j_k}$. This alludes to the role of Alice and Bob's totient functions, $\varphi(N_{\alpha,\beta}(M_A))$ and $\varphi(N_{\alpha,\beta'}(M_B))$, as private keys in the above protocol. Indeed, these numbers are not exchanged, and they are kept on the respective participant sides throughout their interaction. Alice's quick check at the end of the protocol is based on two basic results in number theory: Fermat's little theorem states that

$$b^{\varphi(x)} = 1 \bmod x$$

for b coprime to x. The totient function is a multiplicative function, meaning that $\varphi(x \cdot y) = \varphi(x)\varphi(y)$ for x coprime to y. Therefore, for any two coprime numbers x and y whose product is coprime to b,

$$\left(b^{\varphi(x)}\right)^{\varphi(y)} = 1 \bmod xy.$$

The methods described above allow Alice and Bob to maintain a secure information exchange using framed links. The authentication protocol complements and strengthens a natural extension of the previously introduced scheme of employing structured light in the form of a framed knot as information carriers[23]. Employing two linked framed knots, referred to as a framed link, thus allows to establish an authentication protocol between two parties. Mathematically, the security behind the protocols lies at the heart of a mathematical task believed to be hard, which is similar in essence to Rivest-Shamir-Adleman (RSA) encryption.

V. CONCLUSIONS

Our encoding protocols only utilize the number of twists in the framed braid and exclude its crossings. In conjunction with framed knots being able of representing multiple framed braids, this feature adds considerable flexibility in constructing the knot to be sent with the set of numbers (N, α, β). Hence, this resulting degree of freedom might prove to be essential in scenarios where the knot must be generated in a physical system bounded by certain laws, such as fluid dynamics[31] or optical diffraction[13,20,23], which might make generating some knots harder than others. The main contribution of this Article is a challenge-response authentication protocol based on framed links whose security relies on solving a classically hard computational problem. Optical vortex knots are indeed an interesting realization of these structures. Experimental realization of relatively simple knot structures (Hopf links, trefoils, cinquefoil, and figure-8 knots) have been reported[20,23]. Schemes for generating more complex optical knots based on the Milnor polynomial[13] have been theoretically proposed and used for the above-mentioned structures. Complex optical vortex knots may be more challenging to generate due to limited resolution of modern spatial light modulators, but an in-depth study in this direction has not been carried so far. Regardless of the specific realization, the topological nature of these structures suggests how they might be robust to a large class of imperfections that can be met in optical communication systems (imperfect optics, turbulence, finite apertures). The linked knot structures, necessary for the validation in the challenge-response protocol, may be generated by generalizing current techniques used for optical knots, for example encoding the two knots on different

frequencies or polarisations and independently shifting their position in space in such a way to introduce a link in the singular skeleton. The results of this work may help identifying what are the families of optical fields needed for knot-based secure communication.

VI. ACKNOWLEDGMENTS

This work was supported by the High Throughput and Secure Networks Challenge Program at the National Research Council of Canada, the Canada Research Chairs (CRC), and Canada First Research Excellence Fund (CFREF) Program. This research was also supported by Grant No. FQXi-RFP-CPW-2006 from the Foundational Questions Institute and Fetzer Franklin Fund, a donor-advised fund of Silicon Valley Community Foundation. E.C. was supported by the Israeli Innovation Authority under Projects No. 70002 and No. 73795, by the Pazy Foundation, by the Israeli Ministry of Science and Technology, and by the Quantum Science and Technology Program of the Israeli Council of Higher Education.

DECLARATIONS

The authors declare no competing financial interests. Correspondence and requests for materials should be addressed to A.C. (avcarmi@bgu.ac.il) or E.K. (ekarimi@uottawa.ca).

[1] L. Kelvin. On vortex atoms. In *Proc. R. Soc. Edin*, volume 6, pages 94–105, 1867.

[2] M. Atiyah. Quantum physics and the topology of knots. *Reviews of Modern Physics*, 67(4):977, 1995.

[3] Y. Akutsu and M. Wadati. Knots, links, braids and exactly solvable models in statistical mechanics. *Communications in Mathematical Physics*, 117(2):243–259, 1988.

[4] E. Witten. Quantum field theory and the jones polynomial. *Communications in Mathematical Physics*, 121(3):351–399, 1989.

[5] V. I. Arnold. Topological methods in hydrodynamics. *Vladimir I. Arnold-Collected Works*, pages 433–454, 1992.

[6] H. Moffatt. Some topological aspects of fluid dynamics. *Journal of Fluid Mechanics*, 914, 2021.

[7] N. E. Bonesteel, L. Hormozi, G. Zikos, and S. H. Simon. Braid topologies for quantum computation. *Physical Review Letters*, 95(14):140503, 2005.

[8] A. Stern and N. H. Lindner. Topological quantum computation–from basic concepts to first experiments. *Science*, 339(6124):1179–1184, 2013.

[9] V. Lahtinen and J. Pachos. A short introduction to topological quantum computation. *SciPost Physics*, 3(3):021, 2017.

[10] A. F. Ranada. Knotted solutions of the Maxwell equations in vacuum. *Journal of Physics A: Mathematical and General*, 23(16):L815, 1990.

[11] C. Hoyos, N. Sircar, and J. Sonnenschein. New knotted solutions of maxwell's equations. *Journal of Physics A: Mathematical and Theoretical*, 48(25):255204, 2015.

[12] A. M. Valverde, L. D. Angulo, M. R. Cabello, S. G. García, J. J. Omiste, and J. Luo. Numerical simulation of knotted solutions for Maxwell equations. *Physical Review E*, 101(6):063305, 2020.

[13] M. R. Dennis, R. P. King, B. Jack, K. Oholleran, and M. J. Padgett. Isolated optical vortex knots. *Nature Physics*, 6(2):118–121, 2010.

[14] J. Leach, M. R. Dennis, J. Courtial, and M. J. Padgett. Vortex knots in light. *New Journal of Physics*, 7(1):55, 2005.

[15] D. Seč, S. Čopar, and S. Žumer. Topological zoo of free-standing knots in confined chiral nematic fluids. *Nature Communications*, 5(1):3057, 2014.

[16] D. S. Hall, M. W. Ray, K. Tiurev, E. Ruokokoski, A. H. Gheorghe, and M. Möttönen. Tying quantum knots. *Nature Physics*, 12(5):478–483, 2016.

[17] D. Sugic, M. R. Dennis, F. Nori, and K. Y. Bliokh. Knotted polarizations and spin in three-dimensional polychromatic waves. *Physical Review Research*, 2(4):042045, 2020.

[18] R. D. Muelas-Hurtado, K. Volke-Sepúlveda, J. L. Ealo, F. Nori, M. A. Alonso, K. Y. Bliokh, and E. Brasselet. Observation of polarization singularities and topological textures in sound waves. *arXiv preprint arXiv:2210.03976*, 2022.

[19] M. F. Ferrer-Garcia, A. D'Errico, H. Larocque, A. Sit, and E. Karimi. Polychromatic electric field knots. *Physical Review Research*, 3(3):033226, 2021.

[20] H. Larocque, D. Sugic, D. Mortimer, A. J. Taylor, R. Fickler, R. W. Boyd, M. R. Dennis, and E. Karimi. Reconstructing the topology of optical polarization knots. *Nature Physics*, 14(11):1079–1082, 2018.

[21] N. C. Lim and S. E. Jackson. Molecular knots in biology and chemistry. *Journal of Physics: Condensed Matter*, 27(35):354101, 2015.

[22] E. Farhi, D. Gosset, A. Hassidim, A. Lutomirski, and P. Shor. Quantum money from knots. In *Proceedings of the 3rd Innovations in Theoretical Computer Science Conference*, pages 276–289, 2012.

[23] H. Larocque, A. D'Errico, M. F. Ferrer-Garcia, A. Carmi, E. Cohen, and E. Karimi. Optical framed knots as information carriers. *Nature Communications*, 11(1):5119, 2020.

[24] L.-J. Kong, W. Zhang, P. Li, X. Guo, J. Zhang, F. Zhang, J. Zhao, and X. Zhang. High capacity topological coding based on nested vortex knots and links. *Nature Communications*, 13(1):2705, 2022.

[25] C. Nayak, S. H. Simon, A. Stern, M. Freedman, and S. D. Sarma. Non-abelian anyons and topological quantum computation. *Reviews of Modern Physics*, 80(3):1083, 2008.

[26] J. W. Alexander. A lemma on systems of knotted curves. *Proceedings of the National Academy of Sciences of the United States of America*, 9(3):93, 1923.

[27] V. V. Prasolov and A. B. Sosinskiĭ. *Knots, links, braids and 3-manifolds: an introduction to the new invariants in low-dimensional topology*. Number 154. American Mathematical Soc., 1997.

[28] M. Elhamdadi, M. Hajij, and K. Istvan. Framed knots. *The Mathematical Intelligencer*, 42(4):7–22, 2020.

[29] N. Dehgan, A. D'Errico, T. Jaouni, and E. Karimi. Effects of aberration on vortex knots. *in preparation*, 2022.

[30] S. Arora and B. Barak. *Computational complexity: a modern approach*. Cambridge University Press, 2009.

[31] D. Kleckner and W. Irvine. Creation and dynamics of knotted vortices. *Nature physics*, 9(4):253–258, 2013.

Chapter 5

Topological transition of the measurement-induced geometric phases

This chapter is based on the following papers:

1. **M. F. Ferrer-García**, K. Snizhko, A. D'Errico, A. Romito, Y. Gefen and E. Karimi, "Topological transitions of the generalized Pancharatnam-Berry phase", *Science advances*, **9**(47), eadg6810.(2023).

In 1932, Von Neuman proposed that the result of a measurement depends on the initial state of the measurement device if we assume that the device also behaves quantum mechanically [90]. Therefore, the procedure of measurement induces quantum back-action noise, increasing the uncertainty of our final state. Despite the apparent drawback that it may present, it is possible to take advantage of the back-action if the influence of measurement is small or *weak* [91]. The work in this chapter is the extension of work introduced in [92]. Here, the authors investigate the existence of a topological transition on the geometric phase as a function of the measurement strength in a photonics platform. The supplementary information of this manuscript can be found in Appendix C.

5.1 The geometric phase

Before defining the concept of a geometrical phase, it is convenient to understand the phenomena of parallel transport anholonomy. To illustrate this concept in a digestible

manner, let us consider a vector $\mathbf{a}$ tangent to the surface of the unit sphere $\mathcal{S}$ at the point $\hat{\mathbf{r}}$. Similarly, we define a closed loop $\mathcal{C}$ on the sphere. As shown in Figure 5.1, if the frame containing $\mathbf{a}$ and $\hat{\mathbf{r}}$ is not allowed to rotate during the transport along $\mathcal{C}$, it becomes apparent that $\mathbf{a}$ does not return to its original direction after completing the circuit. In the previous example, the angle α between the initial and final direction of $\mathbf{a}$ defines an anholonomy: the failure of a variable to return to its initial value when the system returns to its initial space [93].

In physics, the concept of anholonomy (typically known as holonomy for mathematicians) is not novel. Undoubtedly, the most familiar example in classical mechanics is the change in the direction of the swing of Foucault's pendulum after a day [94]. In 1984, Sir Michael Berry reported that the wavefunction of a quantum system that undergoes an adiabatic cyclic change exhibits an additional phase term besides the one arising from its temporal evolution. In contrast to the latter dynamical phase, the geometric phase depends on the path taken by the system on its parameter space [95]. Examples of geometrical phases can be found in the context of condensed matter physics [96].

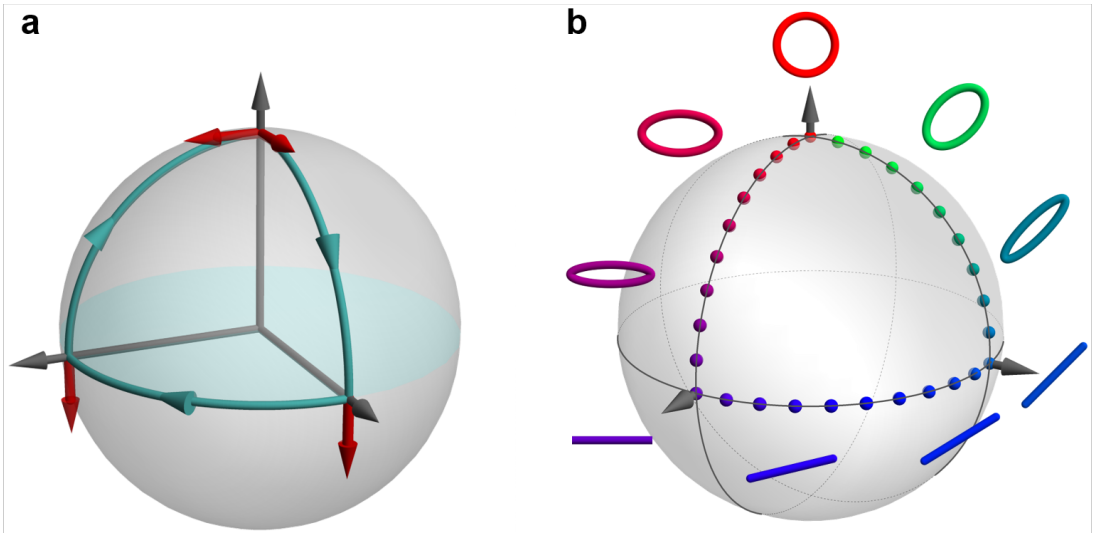

Figure 5.1: **Geometric Phase a.** Parallel transport of a vector on a curved surface. Starting at the Northpole of the sphere, and keeping the frame fixed at every point of the closed trajectory, the final state does not correspond to the initial state. **b.** Evolution of the polarization ellipse as we follow a close trajectory on the Poincaré sphere.

In optical systems, it is possible to identify several geometric phase manifestations,

such as the case of a trajectory-dependent phase acquired as the beam follows a three-dimensional path [97–99] or in the cycle of transformation of photonic squeezed states [100–102]. However, one of the first observations of a geometric phase in optics was predicted by Pancharatnam years before Berry's discovery. While studying the interference pattern at the output of a birefringent crystal, he defined the phase difference between two different polarization states $|e_a\rangle$ and $|e_b\rangle$ as $\phi = \mathrm{Arg}\,\langle e_b|e_a\rangle$, where we have adopted Dirac's notation for reasons of convenience. As introduced in Section 1.1.1, these polarization states can be mapped to localized points on the Poincaré sphere (PS). Taking advantage of the Jones formalism, it is possible to define a transformation operator $\hat{U}$ such that $|e_a\rangle \rightarrow \hat{U}\,|e_a\rangle = |e_b\rangle$, which translates as a displacement along a geodesic on the sphere. Therefore, we can define a protocol in which the beam of light returns to its original polarization state after a sequence of N transformations

$$|e'_a\rangle = \prod_{n=1}^{N} U_n\,|e_a\rangle\,. \tag{5.1}$$

During this process, the evolution of the polarization state traces a trajectory on the PS with a subtended solid angle Ω. Pancharatnam proved that by following a cyclic transformation protocol, the phase difference $\mathrm{Arg}\,\langle e'_a|e_a\rangle$ was equal to half the solid angle Ω spanned on the PS [33].

5.2 A brief introduction to quantum measurement theory

Bayesian statistical interference is the foundation of classical measurement theory. In this classical domain, the information about a variable x is contained in the associated probability distribution $P(x)$ [103]. However, while similar, the notion of measurement in the quantum realm implies making some adjustments due to its intrinsic complex nature. In general, a quantum state is described by a wave function [104]

$$|\Psi\rangle = \sum_m c_m\,|\psi_m\rangle\,, \tag{5.2}$$

where $|\psi_m\rangle$ are all the possible states in which the system can be, and c_m are the corresponding coefficients in the superposition, such that the probability of occurrence is given by $p(x) = |c_m|^2$. A measurement on a quantum system is described by a set of operators $\{A_n\}$ that satisfy the condition

$$\sum_n A_n^\dagger A_n = I,$$

where $(\cdot)^\dagger$ defines the Hermitian conjugate of an operator and I is the identity. If we consider that a system is in a state $|\Psi\rangle$ before the measurement, the action of an operator A yields the transformation

$$|\Psi\rangle \rightarrow \frac{A\,|\Psi\rangle}{\sqrt{\langle\Psi|\,A^\dagger A\,|\Psi\rangle}} = |\Psi_A\rangle\,. \tag{5.3}$$

It is often said that applying a measurement on a system "collapses" the wave functions since it takes an arbitrary input state and returns a state that is consistent with the measurement. The expected value of an operator A for a state $|\Psi\rangle$ given by,

$$\langle A\rangle = \langle\Psi|\,A\,|\Psi\rangle\,. \tag{5.4}$$

5.2.1 Weak measurements

In reality, a physical measurement implies that the quantum system interacts with a measuring device, commonly known as the *meter*. While the nature of this device is typically assumed to be classical, nothing prevents us from also considering the meter as a quantum-mechanical system. Thus, as the state system of our interest is collapsed, the state of the meter also changes [90]. However, as a direct result of Heisenberg's uncertainty principle, it is possible to learn about an observable of one component by perturbing the other and performing a measurement on the composite quantum system.

Following the measurement postulate described above and applying some modifications, it could be possible to exploit its disadvantage as an opportunity to obtain information from the state of the quantum system [105,106]. To illustrate this measurement procedure, let us consider a composite quantum state $|\Psi\rangle = |\varphi\rangle \otimes |\phi(q)\rangle$. Here, $|\varphi\rangle$ stands as the state of the system we are interested in, while the second one is the initial state of the measuring device, given by

$$|\varphi(q)\rangle = C\int_{-\infty}^{\infty} |q_d\rangle \exp\left[-\frac{q_d^2}{4w_q^2}\right] dq_d, \tag{5.5}$$

where q is the canonical position, and w_q is the standard deviation of the Gaussian distribution of the measuring device. The Hamiltonian of standard measurement procedure is [90]

$$H = gA \otimes p_d, \tag{5.6}$$

where A is the observable of interest, p_d refers to the momentum operator of the measuring device, i.e., the canonical conjugate of its position q, and g is a normalized coupling strength

during the interaction time. Then, we can write the evolution of the initial system as

$$e^{-i\int H dt}\,|\varphi\rangle \otimes |\phi(q)\rangle \to \sum_j a_j e \otimes |a_j\rangle\,, \tag{5.7}$$

where we have expanded the initial system using the basis of eigenstates of A. Notice that the state of the measuring device experienced shifts by a_j for each component. From here, it is possible to distinguish two regimes [105]:

1. When the waist w_q of the distribution is smaller than the differences $q - a_j$, the measurement's output yields a superposition of Gaussian distributions, each correlated with a different eigenstate of A. Therefore, a single postselection step on q indicates the value of A.

2. On the other hand, if $w_q \gg |q - a_j|$ for any a_j, the resultant superposition of Gaussian distributions is similar to the input distribution. Thus, the measurement of a single system is not capable of describing the system since $w_q \gg \langle A\rangle$. Nevertheless, by repeating the experiment on an ensemble of N identically prepared states, we are able to reduce the uncertainty of the complete set of measurements while keeping the expected value $\langle A\rangle$ unchanged.

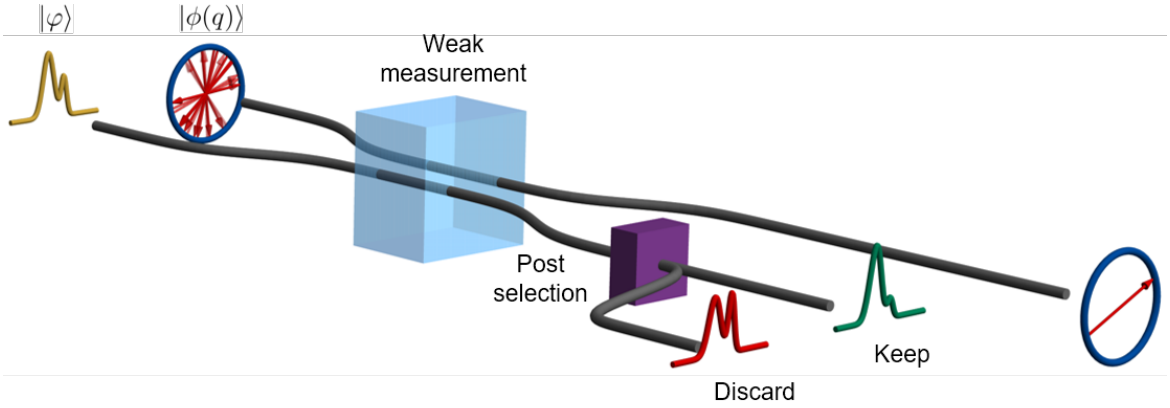

Figure 5.2: **Post-selected weak measurements.** Initially, the quantum system of interest in the state $|\varphi\rangle$ is coupled to a the measuring device. The latter is assumed to exhibit a quantum-mechanical nature described by $|\phi(q)\rangle$. Counterintuitively, the uncertainty on the state of our measuring device is assumed to be large. Then, the composite state $|\Psi\rangle = |\varphi\rangle \otimes |\phi(q)\rangle$ evolves according to the Hamiltonian given by Eq. (5.6). A projective measurement is used to collapse the wave function. If the post-selected state coincides with the desired output, the measurement device's readout is kept. Otherwise, the readout is discarded.

PHYSICS

Topological transitions of the generalized Pancharatnam-Berry phase

Manuel F. Ferrer-Garcia[1], Kyrylo Snizhko[2,3,4], Alessio D'Errico[1]*, Alessandro Romito[5], Yuval Gefen[2], Ebrahim Karimi[1]

Distinct from the dynamical phase, in a cyclic evolution, a system's state may acquire an additional component, a.k.a. geometric phase. Recently, it has been demonstrated that geometric phases can be induced by a sequence of generalized measurements implemented on a single qubit. Furthermore, it has been predicted that these geometric phases may exhibit a topological transition as a function of the measurement strength. We demonstrate and study this transition experimentally by using an optical platform where the qubit is represented by the polarization of light and the weak measurement is performed by means of coupling with the spatial degree of freedom. Our protocol can be interpreted in terms of environment-induced geometric phases, whose values are topologically determined by the environment-system coupling strength. Our results show that the two limits of geometric phase induced by sequences of either weak or projective measurements are topologically distinct.

INTRODUCTION

When a quantum state undergoes a cyclic evolution, the phase acquired is given by the well-known dynamical component and an additional contribution, associated with the geometrical features of the path followed by the state. This additional contribution is known as the geometric phase. The general framework for the emergence of a geometric phase has been pointed out first by Berry (*1*) in the context of adiabatic quantum evolution. A specific realization of this phase had been earlier considered by Pancharatnam (*2*) in his study of generalized interference theory. Pancharantnam's theory shows how geometric phases can be acquired in a nonadiabatic cyclic evolution, noting that these are given by the area enclosed by the respective trajectory of the system in the state space. The Pancharantnam phase can be observed following a sequence of running projective measurements, each of a different observable, where the last measurement projects on the initial state (*3*–*5*). Geometric phases have found applications in several fields of physics (*6*), in particular, in optics (*7*–*10*) and condensed matter physics (*11*–*15*). The Berry phase is a key theme for understanding topological phases of matter (*15*). For instance, the Berry phase plays the role of a topological invariant in one-dimensional chiral symmetric systems (*16*, *17*) and serves as the fundamental building block in the definition of other topological invariants, such as Chern numbers (*18*). Going beyond Hamiltonian dynamics, the emergence of geometric phases has been predicted and observed in the context of non-Hermitian evolution (*19*–*21*); these phases were further shown to emerge following a sequence of weak measurements (*22*, *23*). Further pursuing the latter theme, a major theoretical development has revealed that dynamics comprising multiple measurements may assign topological features to geometric phases. In particular, the limits of weak and strong measurement are topologically distinct (*23*–*25*). This prediction has recently been confirmed using a superconducting qubit platform (*26*). That study has implemented postselection on each individual measurement. This aligns with the original theoretical proposal (*23*–*25*), yet it leaves the question open: To what extent is the predicted topological transition a feature of the specific laid-down protocol?

The experiment reported here not only uses a platform different from that of (*26*) (namely, an optical platform) but also introduces a conceptually different protocol: rather than exercising postselection on each individual detector's readout, here, we implement postselection on a joint readout of all measurements of the run. We find that a topological phase transition also takes place under such generalized conditions, with distinct values of the topological number characterizing the respective limits of projective and infinitely weak measurements. Our experimental procedure consists of a sequence of measurements, each implemented by a set of optical elements. The key optical element is a polarization-sensitive beam displacer (BD), which is used to execute a weak measurement of the polarization state of a laser beam. Using additional elements [quarter-wave plates (QWPs) and compensating wave plates (CWPs)] serves to tune the measurement to a specific observable. The strength of the measurement is determined by the ratio of the beam width and the difference of transverse displacements of orthogonal polarizations. The detector's readout is, in fact, the polarization degree of freedom of the photon, which, in turn, could be viewed as the system, while the transverse position can be viewed as the environment. Our protocol could then be interpreted as an environment inducing a geometric phase, highlighting the dual nature of detector/environment. Last, we investigate the robustness of the observed topological properties with respect to setup imperfections.

RESULTS

Theoretical overview

We consider a class of processes where N measurements are performed on a quantum system, as shown in Fig. 1A. Each step is a postselected measurement associated with the polarization state

[1]Nexus for Quantum Technologies, University of Ottawa, Ottawa, K1N 5N6 ON, Canada. [2]Department of Condensed Matter Physics, Weizmann Institute of Science, Rehovot 76100, Israel. [3]Institute for Quantum Materials and Technologies, Karlsruhe Institute of Technology, 76021 Karlsruhe, Germany. [4]Université Grenoble Alpes, CEA, Grenoble INP, IRIG, PHELIQS, 38000 Grenoble, France. [5]Department of Physics, Lancaster University, Lancaster LA1 4YB, UK.
*Corresponding author. Email: aderrico@uottawa.ca

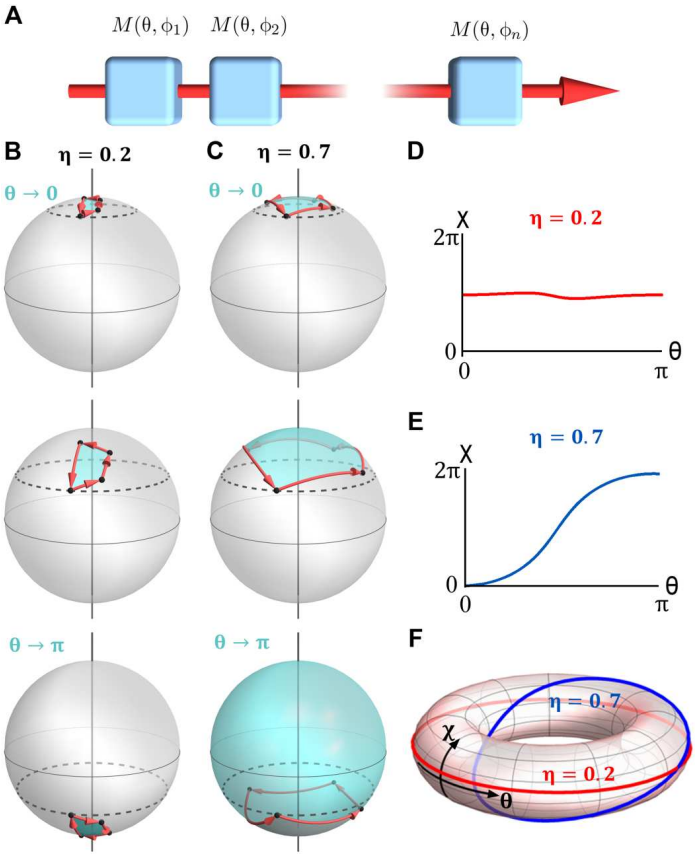

Fig. 1. Measurement-induced phase and its topological transition. (**A**) The state trajectory of a system is determined by a series of *N* measurements along different directions (θ, ϕ). (**B** and **C**) The state trajectory on the Bloch sphere for a sequence of three measurements with strength η = 0.2 (B) and η = 0.7. (C) Different rows represent different values of θ. The black dashed line corresponds to θ, at which the measurements are performed. The black points connected by red arrows denote the system state trajectory, as induced by the measurements. The colored portion of the Bloch sphere is the solid angle subtended by the respective trajectory. The accumulated geometric phase on each trajectory is plotted in (**D** and **E**) as a function of θ. At both points θ = 0 and π, χ mod 2π = 0, making these values of θ equivalent. Hence, the curves can be mapped onto a torus (**F**), which highlights the topological distinction between the cases η = 0.2 and η = 0.7.

$|\theta, \phi\rangle$, where θ and ϕ stand for the polar and azimuthal coordinates on the Bloch sphere, respectively. We can define a sequence of measurements (θ, ϕ_n) for a fixed value of $\theta \in [0, \pi]$ while the azimuth is spanned in discrete steps $\phi_n = 2\pi n/(N + 1)$. Let us denote the acquired geometric phase $\chi_\eta(\theta)$, where $\eta \in [0, \infty)$ is introduced to indicate the strength of the measurement. It can be shown that $\Delta\chi_\eta = \chi_\eta(\pi) - \chi_\eta(0) = 2\pi m$, where *m* is an integer; see Supplementary Materials for more details.

As illustrated in Fig. 1B, for infinitely weak measurements, $\eta \to 0$, the effect of each measurement is vanishingly small. Therefore, $\chi(\theta) = 0$ for any value of θ, implying that $\Delta\chi_{\eta\to 0} = 0$. However, in the limit of projective measurements, strong measurement, one observes that $\Delta\chi_{\eta\to\infty} = 2\pi$, as shown in Pancharatnam's geometric-phase theory (*2*). An example of the latter case, strong measurement limit, is illustrated in Fig. 1C: When θ = 0, the measurement sequence does not change the projected state. Thus, the trajectory on the Bloch sphere shrinks to a single point independently of the measurement strength. In consequence, the enclosed area—and the geometrical phase—is zero. For $\theta \to 0$, the state follows a loop close to the initial projected state, acquiring a small geometric phase. As $\theta \to \pi$, the state follows a similar loop close to the south pole of the Bloch sphere, thus the enclosed geometric phase is close to 2π. This gives $\Delta\chi_{\eta\to\infty} = 2\pi$, as stated above. The distinction between $\Delta\chi_{\eta\to 0} = 0$ and $\Delta\chi_{\eta\to\infty} = 2\pi$ suggests the existence of a transition in the behavior of the geometric phase, as the measurement strength η is varied. Because $\Delta\chi = 2\pi m$, the nature of the transition is topological.

The topological nature of this transition becomes evident when plotting the function $\chi \in [0,2\pi)$ as a function of $\theta \in [0, \pi]$ (Fig. 1, D to F). Because $\chi(0) = \chi(\pi) = 0 (\mathrm{mod}\ 2\pi)$, this function can be mapped onto a closed loop on the torus $T = [0,2\pi) \times [0, \pi)$, as shown in Fig. 1F. For $\Delta\chi = 2\pi$ (sufficiently large η), one obtains a curve that wraps once around the vertical cycle of the torus, while for $\Delta\chi = 0$ (sufficiently small η), the corresponding curve can be continuously deformed in the coordinate curve $\chi = 0$. The two curves obtained in the strong and weak measurement cases cannot be continuously deformed into each other. Therefore, the dependence of the geometric phase on θ in the strong and weak measurement regimes is topologically distinct.

Note that the topological transition is not possible if the function $\chi(\theta)$ is always well defined and continuous. At the critical measurement strength, η_{cr}, the function $\chi_{cr}(\theta)$ is not well defined. The studies in (*23*–*25*) predict that this happens via a vanishing interference contrast at some θ at η_{cr}. Below, we confirm this in our experiments.

Experimental setup

We demonstrate the existence of this topological transition in an optical experiment where the qubit state is associated with the polarization of a coherent beam. As illustrated in Fig. 2A, the beam goes through a series of $N = 3$ identical optical stages that emulate the measurement steps. Each stage is composed of a quarter wave plate (QWP), whose fast axis is oriented at angle $\alpha = \theta/2$ with respect to the vertical, followed by a YVO_4 beam displacer (BD) and an additional compensation wave plate (CWP). The BD's ordinary and extraordinary axes are aligned along $\hat{\mathbf{y}}$ and $\hat{\mathbf{x}}$, respectively. Therefore, the BD shifts the centroid of the horizontally polarized component by a distance d_x, keeping the vertically polarized contribution unchanged. The BD essentially performs measurement on the vertical/horizontal polarization basis, as the horizontally polarized component of the beam is spatially displaced. If the beam waist w_0 is larger than d_x, then the measurement is weak, because there is no sharp separation between the two polarization components (see Fig. 2B). If the waist is much smaller than the displacement, $w_0 \ll d_x$, then this implements a projective measurement, as the two polarization components are completely separated. Therefore, we can control the measurement strength by modifying w_0. The CWP with a vertically aligned fast axis is used to compensate for the phase difference between the two polarization components accumulated while propagating inside the BD.

The role of the QWPs is to implement the desired sequence of measurement directions (θ, ϕ_n) on the Bloch sphere. The rotation by angle α enables controlling the polar angle θ of the measurement axis. The sequence of measurements induced by the setup in Fig. 2A corresponds to the directions (θ, ϕ_n) rotated by an angle $\theta = 2\alpha$ around the *y* axis of the Bloch sphere; cf. Fig. 2C. The details of this correspondence are explained in the "Simplifying the

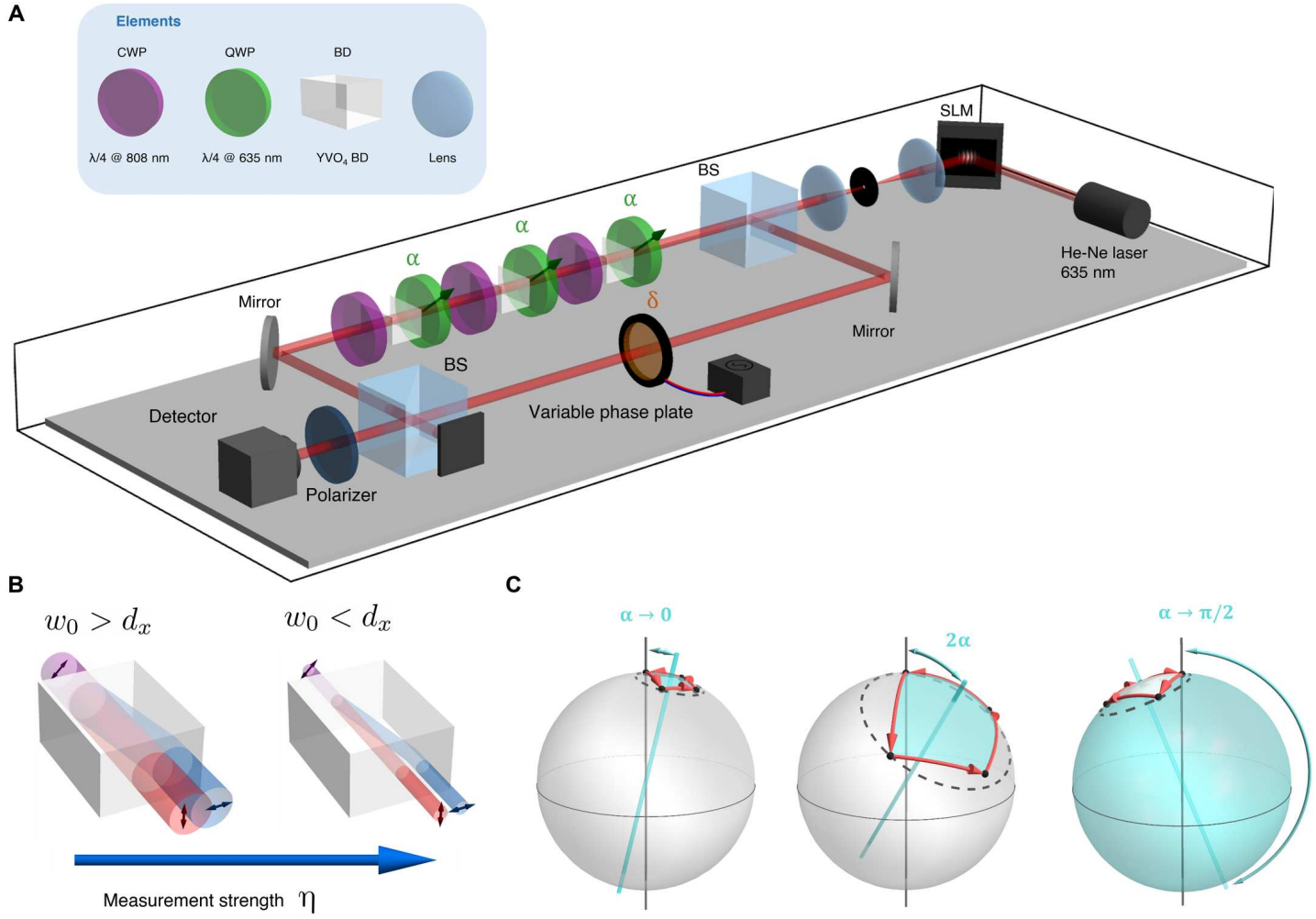

Fig. 2. Optical implementation of a sequence of weak polarization measurements. (**A**) Experimental setup used to detect the geometrical phase acquired because of a sequence of polarization measurements. A 632.9-nm laser emits a vertically polarized Gaussian beam that impinges on a spatial light modulator (SLM) to obtain a beam with a certain width w_0. The beam is split into two paths: in one is subjected to a sequence of transformations, while a spatially uniform phase δ is applied to the other path. Each stage is composed of a QWP, whose fast axis is oriented at angle α with respect to the vertical, a BD, and a QWP for 808 nm acting as the compensation wave plate (CWP). Lastly, the output power of the interference is recorded after the recombined beam passes through a vertical polarizer. BS, beam splitter. (**B**) The measurement strength $\eta = d_x/w_0$ is controlled by varying the waist parameter w_0 of the input beam. When w_0 is much larger than the beam displacement d_x, the displacement is ineffectual, corresponding to a weak measurement. For $w_0 < d_x$, the two polarizations become two well-separated beams, leading to a projective measurement in the limit $w_0 \to 0$. (**C**) In contrast to the examples exhibited in Fig. 1 (B and C), the sequence of measurements produced by this setup corresponds to a circle of $\theta = 2\alpha$, which is additionally rotated by 2α around the *x* axis of the Bloch sphere. This does not affect the subtended area and, consequently, the accumulated geometric phase.

experimental setup″ section. Given the geometric nature of the induced phase, the expected topological transition remains unaffected by this rotation, both qualitatively and quantitatively. Lastly, to complete the cyclic evolution, the polarization state is projected onto the initial state using a polarizer. Our aim is to investigate the geometrical phase acquired by the undeflected beam (corresponding to the measurement postselected to yield a null outcome). This is done by interfering the final state with the reference beam, which only experiences a controllable phase shift δ introduced by a variable phase plate. The output power at the interferometer exit is recorded as a function of δ. The shift of this curve corresponds to the acquired geometric phase. The input beam is generated by means of a spatial light modulator that displays a hologram allowing to tailor the beam waist through the technique introduced in (*27*). We set the input beam's polarization state to be vertical ($\hat{\mathbf{y}}$), corresponding to the initial state in the direction (θ, ϕ_0) in the theoretical protocol. On the basis of this setup, the measurement protocol to unveil the hidden topological transition is given as follows. The strength of our intermediate $N = 3$ measurements is regulated by varying the waist parameter of the input beam: The value of w_0 is inversely proportional to the measurement strength $\eta = d_x/w_0$ (see Fig. 2C). For a fixed waist parameter, we proceed to get power readouts as a function of the reference arm phase shift $\delta \in [0, 2\pi]$, while $\alpha = \theta/2$ is kept constant. From here, it is possible to retrieve the accumulated geometrical phase $\chi_\eta(\theta = 2\alpha)$ for a given orientation of QWPs, α, by proper curve fitting. By varying the QWP orientation, it is possible to reconstruct the behavior of $\chi_\eta(\theta = 2\alpha)$ for all α for a given measurement strength.

Experimental results

Here, we discuss the experimental results and their relation to the theoretical predictions. Because the postselection in our experiment goes beyond the original theoretical proposal, we have modeled the experiment to confirm the presence of a topological transition theoretically (see the "Optical implementation of the null-weak measurement" section). Figure 3A shows that when w_0 is sufficiently small, i.e., strong measurement regime, the simulation predicts $\Delta\chi = \chi(\alpha = \pi/2) - \chi(\alpha = 0) = 2\pi$, while for the case of weak measurements ($w_0 < d_x$), $\Delta\chi = 0$. A sharp transition occurs at $w_0 = 0.85$ mm, where the interference contrast vanishes for $\alpha \approx \pi/4$, enabling the abrupt change of the phase behavior. The experiment was carried on by performing measurements for w_0 between 0.6 and 2.5 mm. The experimental results, shown in Fig. 3B, clearly exhibit a similar transition between $\Delta\chi = 2\pi$ for small w_0 and $\Delta\chi = 0$ for large w_0, as well as the vanishing contrast at the transition.

The difference $\Delta\chi = \chi(\pi/2) - \chi(0)$ in the observations is not strictly equal to 0 or 2π but can slightly deviate from these values. This is seen most prominently for $w_0 = 0.6$ mm. We attribute this to the stability of the Mach-Zehnder interferometer, in particular to a small drift in the phase between the two arms during the measurement process (which was performed in 45 min). We emphasize that this does not violate the topological quantization of $\Delta\chi$ but introduces an error in its extraction. In all the cases, the extracted $\Delta\chi$ is close to either 0 or 2π, making the determination of the topological index m straightforward. The vanishing contrast at the transition also confirms the expected phenomenology of the topological transition.

We note that the waist w_0^* at which the transition happens clearly deviates from the theory predictions: $w_0^* = 0.85$ mm in the simulation, while $w_0^* = 1.2$ mm in the experiment. We attribute this deviation to the fact that the surfaces of the BDs are parallel within a few tens of arc seconds, as stated by the manufacturer and verified by us independently. This tiny angle between the two surfaces induces a small transverse wave vector difference between the two components. We have incorporated this effect into our theoretical modeling, the results of which are presented in Fig. 3C. With this, we are able to reproduce the change in the transition location. A detailed analysis of these imperfections and the enhanced modeling can be found in section S2.

Theoretical studies have predicted (*24*, *25*) that the topological transition only exists if the dynamical phases are compensated accurately enough. In our work, this condition is satisfied. In Fig. 4 we explored theoretically the topological phase diagram considering the additional parameter γ corresponding to the optical retardation of the CWP. The results show that there is a range of values of γ where the topological transition can be observed, both in the ideal scenario and in the case of imperfect optical elements.

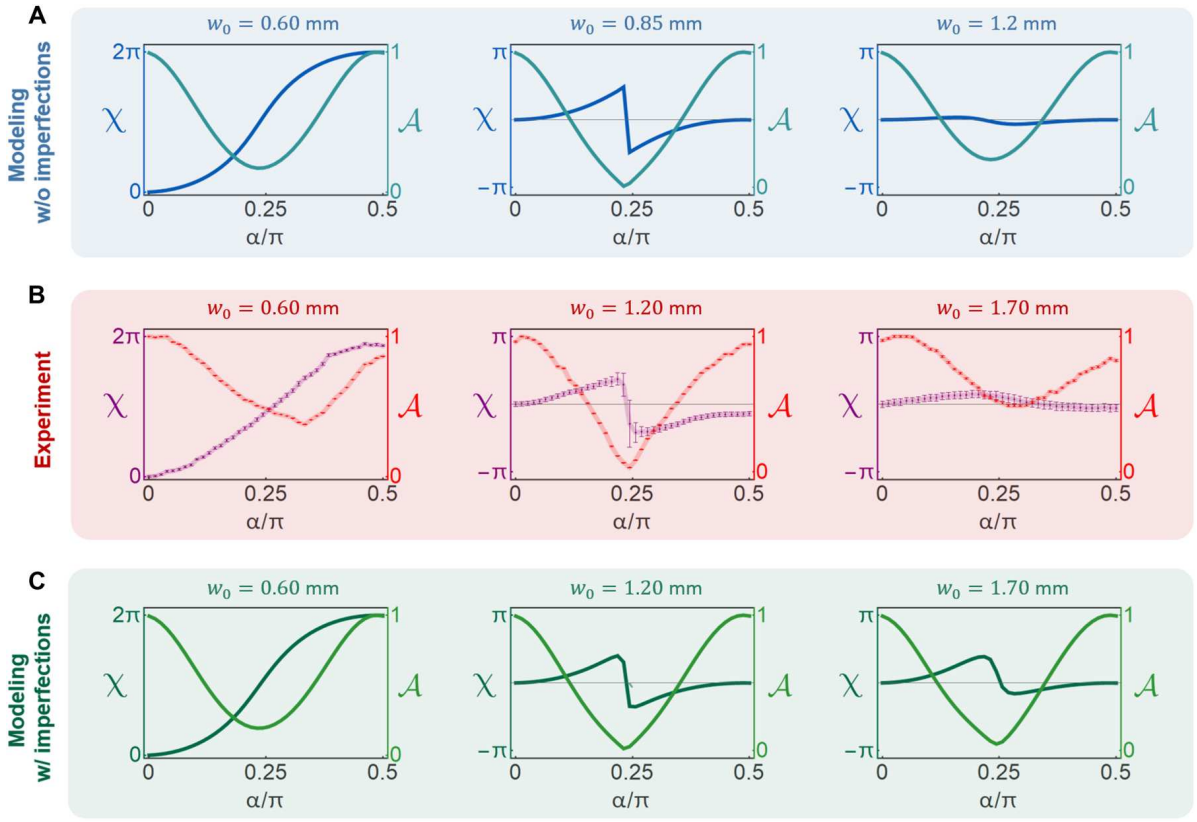

Fig. 3. Experimentally measured and theoretically simulated geometric phase. Topological transition in the measurement-induced geometric phase $\chi(\alpha = \theta/2)$: (**A**) theoretical modeling, (**B**) experimental results, and (**C**) modeling incorporating the imperfection of the birefringent crystals. The plots show the phase $\chi(\alpha)$ and the interference contrast $\mathcal{A}$. The left column corresponds to a narrow beam (small w_0, strong measurement) and features $\Delta\chi = 2\pi$. The right column corresponds to a large beam width (weak measurement) and exhibits $\Delta\chi = 0$. The middle column represents a point close to the transition: The phase $\chi(\alpha)$ exhibits a sharp change near $\alpha = \pi/4$. The sharp change of the phase coincides with the vanishing of the interference contrast, which renders $\chi(\alpha)$ ill-defined and enables the topological transition.

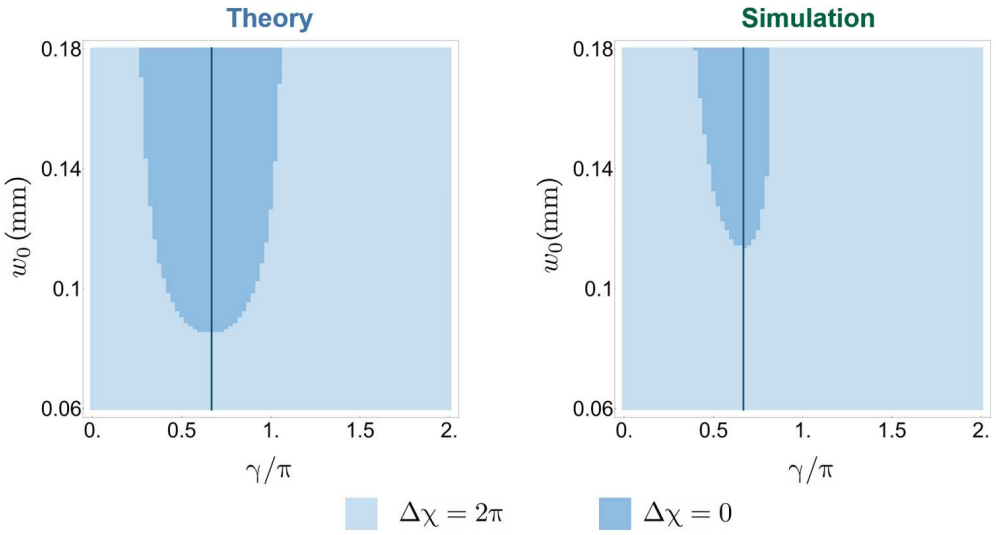

Fig. 4. Topological phase dependence on compensating waveplates. The phase diagram (theoretical) depicting the topological properties of the measurement-induced phase as a function of beam waist w_0 and the compensation phase γ. We present the results of a theory simulation without (left) and including (right) the experimental imperfections of the birefringent crystals. Note that the trivial phase with (Δχ = 0) exists only in a narrow interval of the phase compensation parameter The vertical line indicates the parameters used in our experiment. The imperfections of birefringent crystals clearly make the trivial region shrink yet do not eliminate the topological transition.

DISCUSSION

We have demonstrated that measurement-induced geometric phases in optical systems exhibit a topological transition. In particular, we consider a family of processes parameterized by a variable α and a measurement strength η. We demonstrated that the geometrical phase, with respect to η and α, exhibits a nontrivial topology. More precisely, the variation Δχ in the geometrical phase as a function of α undergoes a sharp transition of 2π as η is varied. The parameter η can be viewed as the coupling strength with an environment, here represented by the light's spatial degree of freedom. In this framework, our observations can be interpreted as topological transitions induced by the coupling to an external environment. The topological transition is robust to amending the protocol and the imperfections in the measurement process. The location of the topological transition depends on specific details of the system (quality of BDs, retardation of the compensating wave plates, etc.). This sensitivity of the transition location may be useful for characterizing optical elements or for sensing. We leave this, however, to future investigations.

MATERIALS AND METHODS

Optical implementation of the null-weak measurement

In our optical implementation of the measurements, the detectors are two-state systems with possible readouts $r = \pm$. We use the photon spatial degree of freedom, i.e., its location in the xy plane (transverse to the propagation direction). The formal description of this is as follows. The incident photon's electric field can be described as

$$\mathbf{E}_0(x,y) = \begin{pmatrix} E_{0y} \\ E_{0x} \end{pmatrix} \sqrt{\frac{2}{\pi w_0^2}} e^{-(x^2+y^2)/w_0^2} e^{ikz} \quad (1)$$

The measurement is implemented via a BD (see Fig. 2B) that shifts the x-polarized component in space

$$\mathbf{E}(x,y) \propto \begin{pmatrix} e^{ikn_yL_y} E_{0y} e^{-(x^2+y^2)/w_0^2} \\ e^{ikn_xL_x} E_{0x} e^{-([x-d_x]^2+y^2)/w_0^2} \end{pmatrix} e^{ikz} \quad (2)$$

where normalizing factors are not shown. Apart from the displacement, the phases associated with propagation in the BD, kn_xL_x and kn_yL_y, are imprinted onto the polarization components. The overall phase is not important, whereas the difference $\gamma = kn_xL_x - kn_yL_y$ may lead to observable consequences; cf. Fig. 4. In our protocol, we compensate for this phase difference; see below. Therefore, here we put, for simplicity, $kn_xL_x = kn_yL_y = 0$.

If, after experiencing the BD, the beam were to interfere with the original beam, then the interference term would be

$$\int dx\, dy\, \mathbf{E}_0^*(x,y)\mathbf{E}(x,y) = |E_{0y}|^2 + |E_{0x}|^2 e^{-\frac{d^2}{2w_0^2}} \quad (3)$$

$$= \begin{pmatrix} E_{0y} \\ E_{0x} \end{pmatrix}^\dagger M_- \begin{pmatrix} E_{0y} \\ E_{0x} \end{pmatrix} \quad (4)$$

where M_-, in analogy with the notation in the Supplementary Materials, is the diagonal matrix $\mathrm{diag}(1, \sqrt{1-\zeta})$, with $\sqrt{1-\zeta} = e^{-d_x^2/(2w_0^2)}$. Therefore, a BD implements a postselected null weak measurement in the photon's polarization space. The measurement strength $\eta = \sqrt{-\ln(1-\zeta)} = d_x/w_0$, as defined in the section "Experimental setup." The limit of projective measurement corresponds to $\eta \to \infty$, while the infinitely weak measurement corresponds to $\eta \to 0$.

Note that in our actual setup (cf. Fig. 2A), the interference happens after three beam displacements have been performed. Therefore, the postselection is implemented not on the readout of each individual measurement but on the combined "readout" of all measurements. This constitutes an important conceptual difference

compared to the original definition of the measurement-induced phase and its topological transition, detailed in the Supplementary Materials. Observation of the topological transition in our work, thus, underlines that the transition is not a feature of a specific narrow protocol but a more general phenomenon.

Phase difference compensation

To compensate for the unwanted phase difference $\gamma = kn_xL_x - kn_yL_y$, one can use a phase plate

$$\mathrm{P}(\varphi) = \begin{pmatrix} e^{i\varphi/2} & 0 \\ 0 & e^{-i\varphi/2} \end{pmatrix} \tag{5}$$

Choosing $\phi = \gamma$ and placing the phase plate after the BD leads to

$$\mathrm{P}(\gamma)\ \mathrm{BD}\ \mathbf{E}_0(x,y) = \sqrt{\frac{2}{\pi w_0^2}} e^{ik(n_xL_x+n_yL_y)/2} e^{ikz} \times \begin{pmatrix} E_{0y} e^{-(x^2+y^2)/w_0^2} \\ E_{0x} e^{-([x-d_x]^2+y^2)/w_0^2} \end{pmatrix} \tag{6}$$

leaving one only with an unimportant overall phase. The overall phase is unimportant because it does not depend on the incoming polarization and thus can be calibrated away.

In our setup (cf. Fig. 2A), the required phase compensation is implemented with a QWP for a wavelength distinct from that of the laser we use. We denote it as CWP.

Measuring different observables

The measurement procedure described above leads to the back action matrix M_-, i.e., to measuring σ_z. To implement measurements of different observables $\mathbf{n} \cdot \boldsymbol{\sigma}$, corresponding to $\mathbf{n} = (\sin\theta\cos\phi, \sin\theta\sin\phi, \cos\theta)$, one needs to be able to (i) discriminate different linear polarizations (not only horizontal and vertical) with a BD and (ii) convert elliptical polarizations to linear and back, so that they can be discriminated by the BD.

(i) can be implemented by rotating the BD in the xy plane

$$\mathrm{BD}(\theta/2) = R(\theta/2)\ \mathrm{BD}\ R(-\theta/2) \tag{7}$$

with the rotation matrix

$$R(\theta/2) = \begin{pmatrix} \cos\theta/2 & -\sin\theta/2 \\ \sin\theta/2 & \cos\theta/2 \end{pmatrix} \tag{8}$$

(ii) can be implemented by placing phase plates $P(\pm\phi)$ before and after the BD.

Therefore, a measurement of $\mathbf{n} \cdot \boldsymbol{\sigma}$ can be implemented via a sequence of elements that involves a rotated BD and CWP, as well as two phase plates

$$\mathcal{M}(\theta,\phi) = \mathrm{P}(-\phi)R(\theta/2)\mathrm{P}(\gamma)\ \mathrm{BD}\ R(-\theta/2)\mathrm{P}(\phi) \tag{9}$$

Note that to rotate the measurement axis by θ, one needs to perform real space rotations by $\alpha = \theta/2$.

This sequence uses four elements per measurement, whereas our setup in Fig. 2 features only three optical elements per measurement. We describe how this is achieved in the next section.

Simplifying the experimental setup

The protocol for observing the topological transition requires sending in a laser beam with polarization

$$\mathbf{E}_{in} = \begin{pmatrix} E_{0y} \\ E_{0x} \end{pmatrix} = \begin{pmatrix} \cos\theta/2 \\ \sin\theta/2 \end{pmatrix} = R(\theta/2)\begin{pmatrix} 1 \\ 0 \end{pmatrix} \tag{10}$$

and using N measurements $\mathcal{M}(\theta, \phi_j)$, where the measurement stages are defined in Eq. 9 and $\phi_j = 2\pi j/(N+1)$. The number of required optical elements can be reduced. To do this, one needs two observations.

First, consider the incoming polarization and the first measurement

$$\mathcal{M}(\theta,\phi_1)\begin{pmatrix} \cos\theta/2 \\ \sin\theta/2 \end{pmatrix} = \mathrm{P}(-\phi_1)R(\theta/2)\mathrm{P}(\gamma)\ \mathrm{BD} \times \underbrace{R(-\theta/2)\mathrm{P}(\phi_1)R(\theta/2)}\begin{pmatrix} 1 \\ 0 \end{pmatrix} \tag{11}$$

The block $R(-\theta/2)\mathrm{P}(\phi_1)R(\theta/2)$ can be interpreted as a phase plate rotated by the angle $\alpha = \theta/2$, $\mathrm{P}(\phi_1, \alpha)$.

Second, consider two sequential measurements

$$\mathcal{M}(\theta,\phi_{j+1})\mathcal{M}(\theta,\phi_j) = \mathrm{P}(-\phi_{j+1})R(\theta/2)\mathrm{P}(\gamma)\ \mathrm{BD} \times \underbrace{R(-\theta/2)\mathrm{P}(\phi_{j+1})\mathrm{P}(-\phi_j)R(\theta/2)} \times \mathrm{P}(\gamma)\ \mathrm{BD}\ R(-\theta/2)\mathrm{P}(\phi_j) \tag{12}$$

The block $R(-\theta/2)\mathrm{P}(\phi_{j+1})\mathrm{P}(-\phi_j)R(\theta/2)$ can be replaced with a single rotated phase plate $\mathrm{P}(\phi_{j+1} - \phi_j, \alpha) = \mathrm{P}(2\pi/(N+1), \alpha) = \mathrm{P}(\phi_1, \alpha)$.

Therefore, instead of having a rotated incoming polarization and rotated BDs, one can have vertical incoming polarization and rotated phase plate $\mathrm{P}(\phi_1, \alpha)$ before the BDs. Note that this setup simplification involves replacing all phase plates $\mathrm{P}(\phi_j)$ with their rotated versions $R(-\theta/2)\mathrm{P}(\phi_j)R(\theta/2)$ and the input polarization $R(\theta/2)(1\ 0)^{\mathrm{T}}$ with $(1\ \ 0)^{\mathrm{T}}$. The simplified setup is related to the original protocol by rotating all the measurement axes $\mathbf{n}_j$ by angle θ around the y axis of the Bloch sphere. For our choice of $N = 3$, we have $\phi_1 = \pi/2$, making the required phase plates $\mathrm{P}(\phi_1, \alpha)$ QWPs and leading to the setup in Fig. 2A.

Supplementary Materials

This PDF file includes:

Sections S1 and S2
Fig. S1
References

REFERENCES AND NOTES

1. M. V. Berry, Quantal phase factors accompanying adiabatic changes. *Proc. R. Soc. Lond.* **392**, 45–57 (1984).
2. S. Pancharatnam, Generalized theory of interference, and its applications. *Proc. Indian Acad. Sci. A.* **44**, 247–262 (1956).
3. J. Samuel, R. Bhandari, General setting for berry's phase. *Phys. Rev. Lett.* **60**, 2339–2342 (1988).
4. M. V. Berry, S. Klein, Geometric phases from stacks of crystal plates. *J. Mod. Optic.* **43**, 165–180 (1996).
5. D. Chruscinski, A. Jamiolkowski, *Geometric Phases in Classical and Quantum Mechanics* (Birkhäuser Basel, 2004).
6. E. Cohen, H. Larocque, F. Bouchard, F. Nejadsattari, Y. Gefen, E. Karimi, Geometric phase from Aharonov–Bohm to Pancharatnam–Berry and beyond. *Nat. Rev. Phys.* **1**, 437–449 (2019).
7. Z. Bomzon, G. Biener, V. Kleiner, E. Hasman, Space-variant Pancharatnam–Berry phase optical elements with computer-generated subwavelength gratings. *Opt. Lett.* **27**, 1141–1143 (2002).
8. K. Y. Bliokh, M. A. Alonso, M. R. Dennis, Geometric phases in 2d and 3d polarized fields: Geometrical, dynamical, and topological aspects. *Rep. Prog. Phys.* **82**, 122401 (2019).
9. A. Rubano, F. Cardano, B. Piccirillo, L. Marrucci, Q-plate technology: A progress review [Invited]. *J. Opt. Soc. Am. B.* **36**, D70 (2019).

10. C. P. Jisha, S. Nolte, A. Alberucci, Geometric phase in optics: From wavefront manipulation to waveguiding. *Laser & Photonics Reviews* **15**, 2100003 (2021).
11. H. C. Higgins, H. C. L.-H. Öpik, U. Öpik, M. H. L. Pryce, R. A. Sack, Studies of the jahn-teller effect. II. the dynamical problem. *Proc. R Soc. Lond.* **244**, 1–16 (1958).
12. J. Zak, Berry's phase for energy bands in solids. *Phys. Rev. Lett.* **62**, 2747–2750 (1989).
13. R. Resta, Manifestations of berry's phase in molecules and condensed matter. *J. Phys. Condens. Matter* **12**, R107–R143 (2000).
14. C. Nayak, S. H. Simon, A. Stern, M. Freedman, S. D. Sarma, Non-abelian anyons and topological quantum computation. *Rev. Mod. Phys.* **80**, 1083–1159 (2008).
15. E. Fradkin, *Field Theories of Condensed Matter Physics* (Cambridge Univ. Press, 2013).
16. R. Resta, Macroscopic polarization in crystalline dielectrics: The geometric phase approach. *Rev. Mod. Phys.* **66**, 899–915 (1994).
17. J. K. Asbóth, L. Oroszlány, A. Pályi, A short course on topological insulators. *Lecture Notes in Physics* **919**, 166 (2016).
18. M. Z. Hasan, C. L. Kane, Colloquium: Topological insulators. *Rev. Mod. Phys.* **82**, 3045–3067 (2010).
19. J. Garrison, E. Wright, Complex geometrical phases for dissipative systems. *Phys. Lett. A.* **128**, 177–181 (1988).
20. G. Dattoli, R. Mignani, A. Torre, Geometrical phase in the cyclic evolution of non-hermitian systems. *J. Phys. A Math. Gen.* **23**, 5795–5806 (1990).
21. R. El-Ganainy, K. G. Makris, M. Khajavikhan, Z. H. Musslimani, S. Rotter, D. N. Christodoulides, Non-Hermitian physics and PT symmetry. *Nat. Phys.* **14**, 11–19 (2018).
22. Y.-W. Cho, Y. Kim, Y.-H. Choi, Y.-S. Kim, S.-W. Han, S.-Y. Lee, S. Moon, Y.-H. Kim, Emergence of the geometric phase from quantum measurement back-action. *Nat. Phys.* **15**, 665–670 (2019).
23. V. Gebhart, K. Snizhko, T. Wellens, A. Buchleitner, A. Romito, Y. Gefen, Topological transition in measurement-induced geometric phases. *Proc. Natl. Acad. Sci. U.S.A.* **117**, 5706–5713 (2020).
24. K. Snizhko, P. Kumar, N. Rao, Y. Gefen, Weak-measurement-induced asymmetric dephasing: Manifestation of intrinsic measurement chirality. *Phys. Rev. Lett.* **127**, 170401 (2021).
25. K. Snizhko, N. Rao, P. Kumar, Y. Gefen, Weak measurement-induced phases and dephasing: Broken symmetry of the geometric phase. *Phys. Rev. Res.* **3**, 043045 (2021).
26. Y. Wang, K. Snizhko, A. Romito, Y. Gefen, K. Murch, Observing a topological transition in weak-measurement-induced geometric phases. *Phys. Rev. Res.* **4**, 023179 (2022).
27. E. Bolduc, N. Bent, E. Santamato, E. Karimi, R. W. Boyd, Exact solution to simultaneous intensity and phase encryption with a single phase-only hologram. *Opt. Lett.* **38**, 3546–3549 (2013).
28. K. Jacobs, *Quantum Measurement Theory and its Applications* (Cambridge Univ. Press, 2014).
29. D. A. Coley, *An Introduction to Genetic Algorithms for Scientists and Engineers* (World Scientific Publishing Company, 1999).

Acknowledgments

Funding: This work was supported by Canada Research Chairs (CRC); Canada First Research Excellence Fund (CFREF) Program; NRC-uOttawa Joint Centre for Extreme Quantum Photonics (JCEP) via High Throughput and Secure Networks Challenge Program at the National Research Council of Canada; Deutsche Forschungsgemeinschaft (German Research Foundation) through project no. 277101999, TRR 183 (Project C01), and project nos. EG 96/13-1, GO 1405/6-1, and MI 658/10-2; Helmholtz International Fellow Award; the Israeli Science Foundation (ISF); NSF Grant No. DMR-2037654; the U.S.-Israel Binational Science Foundation (BSF); and the Royal Society, grant no. IECR2212041. **Author contributions:** K.S., A.R., Y.G., and E.K. conceived the idea. M.F. F.-G., A.D., K.S., and E.K. designed the experiment. M.F.F.-G. and K.S. performed the theoretical simulations. M.F.F.-G. and A.D. performed the experiment and collected the data. M.F.F.-G., A.D., and K.S. analyzed the data. M.F.F.-G., K.S., A.D., and A.R. prepared the first version of the manuscript. All authors discussed the results and contributed to the text of the manuscript. **Competing interests:** The authors declare that they have no competing interests. **Data and materials availability:** All data needed to evaluate the conclusions of the paper are present in the paper. Raw data of interferometric measurements can be found at: https://doi.org/10.5061/dryad.41ns1rnmg.

Submitted 16 January 2023
Accepted 25 October 2023
Published 24 November 2023
10.1126/sciadv.adg6810

Chapter 6

Conclusions

In conclusion, we have carried out four projects in which we have explored different topological effects using the framework of structured light.

In chapter 2, we theoretically analyze the radiation-induced force exerted by different vector beams on a dissipative-absorptive substrate. In particular, we consider the family of cylindrical vector beams and full Poincaré beams carrying different types of polarization topologies. Finally, we extended our analysis by assuming non-paraxial light obtained by tight focusing the vector vortex beams mentioned above. As a result of our calculations, we identify the effect of the polarization singularities on both the scattering and absorption-dependent components of the force. The authors expect that these results will provide tools for optical manipulation and nanostructuring materials.

Inspired by the study on bichromatic polarization states and the three-dimensional structured fields obtained by tight focusing, we explore the *zoo* of polychromatic polarization states in chapter 3. Here, the authors propose a technique to tie the tip of the electric field vector and obtain knotted polarization states. Experimentally, these exotic states can be generated by exploiting recent advances in phase locking and spectrum manipulation. Their detection and reconstruction are possible by analyzing the scattering pattern of the focused fields on molecules or by making use of recently developed interferometric methods in nano-optics. We believe that the use of these non-trivial states unveils new complex phenomena when shined on single atoms and bulk solid materials.

In chapter 4, we propose the use of low-dimensional topological elements for encoding and the establishment of secure public communication. The use of these topological objects relies on the greater resilience to imperfections due to their physical materialization and their posterior interaction with the environment. In the first part of the chapter, we

show the experimental reconstruction of framed knots using structured light. In addition, the distribution of half twists per strand in the braid representation is employed to encode prime numbers. Based on this encoding scheme, we establish protocols to share information securely between two users. Particularly, we introduce a challenge-response authentication protocol based on framed links. We hope that the results of this work inspire and motivate future research of topological elements to store and share information.

Finally, we analyze the emergence of a topological transition on the Pancharatnam-Berry phase acquired when the operators in the evolution move from the limit of a strong (projective) measurement to the case of weak measurements. The theoretical results were corroborated experimentally by using an optical platform. It must be noted that the observed topological transition is robust, allowing its observation despite the presence of imperfections in the optical elements. The results of this work may motivate the study of environment-induced geometric phases and unveil new subtle topological features.

APPENDICES

Appendix A

Numerical calculation of focused fields

In this section, we provide the Wolfram Mathematica and Python notebooks used for the calculation of the focal field beams. Further explanation and examples can be found in this GitHub repository.

A.1 Wolfram Mathematica

A.1.1 Main code

Contribution of the x-polarized component of the input field

```
(* Resultant X-component *)
LGxx[Rho_, Phi_, z_, ScriptL_,a_, b_] :=
    Exp[I ScriptL Phi] NIntegrate[ Sqrt[Cos[Theta]] Sin[Theta]
     *lg[(Sin[Theta]/Sin[Alpha]),ScriptL] Exp[I k z Cos[Theta]]
      *(1/2 (1 + Cos[Theta]) BesselJ[ScriptL, k Rho Sin[Theta]]
       + 1/4 (1 - Cos[Theta]) (BesselJ[ScriptL + 2, k Rho Sin[Theta]]
        *Exp[I 2 Phi] + BesselJ[ScriptL - 2, k Rho Sin[Theta]] Exp[-I 2 Phi]))
      ,{Theta, a, b}];

(* Resultant Y-component *)
LGxy[Rho_, Phi_, z_, ScriptL_, a_, b_] :=
    Exp[I ScriptL Phi] (-1/(2 I)) NIntegrate[ Sqrt[Cos[Theta]] Sin[Theta]
     *lg[(Sin[Theta]/ Sin[Alpha]), ScriptL] Exp[I k z Cos[Theta]]
      *((Cos[Theta] - 1) (BesselJ[ScriptL + 2, k Rho Sin[Theta]] Exp[2 I Phi]
        -BesselJ[ScriptL - 2, k Rho Sin[Theta]] Exp[-2 I Phi]))*
     ,{Theta, a, b}];
```

```
(* Resultant Z-component *)
LGxz[Rho_, Phi_, z_, ScriptL_, a_, b_] :=
    Exp[I ScriptL Phi] (-I/2) NIntegrate[Sqrt[Cos[Theta]] Sin[Theta]^2
     *lg[(Sin[Theta]/ Sin[Alpha]), ScriptL] Exp[I k z Cos[Theta]]
      *(BesselJ[ScriptL + 1, k Rho Sin[Theta]] E^(I Phi)
       - BesselJ[ScriptL - 1, k Rho Sin[Theta]] E^(-I Phi))
     ,{Theta, a, b}];
```

Contribution of the y-polarized component of the input field

```
(* Resultant X-component *)
LGyx[Rho_, Phi_, z_, ScriptL_, a_, b_] :=
    Exp[I ScriptL Phi] (-1/(2 I)) NIntegrate[ Sqrt[Cos[Theta]] Sin[Theta]
      *lg[(Sin[Theta]/Sin[Alpha]), ScriptL] Exp[I k z Cos[Theta]]
       *((Cos[Theta] - 1) (BesselJ[ScriptL + 2, k Rho Sin[Theta]] Exp[ 2 I Phi]
        - BesselJ[ScriptL - 2, k Rho Sin[Theta]] Exp[-2 I Phi]))
     , {Theta, a, b}];

(* Resultant Y-component *)
LGyy[Rho_, Phi_, z_, ScriptL_, a_, b_] :=
    Exp[I ScriptL Phi] NIntegrate[ Sqrt[Cos[Theta]] Sin[Theta]
     *lg[(Sin[Theta]/Sin[Alpha]), ScriptL] Exp[I k z Cos[Theta]]
      *(1/2 (1 + Cos[Theta]) BesselJ[ScriptL, k Rho Sin[Theta]]
       - 1/4 (1 - Cos[Theta]) ( BesselJ[ScriptL + 2, k Rho Sin[Theta]] Exp[I 2 Phi]
        + BesselJ[ScriptL - 2, k Rho Sin[Theta]] Exp[-I 2 Phi]))
     , {Theta, a, b}];

(* Resultant Z-component *)
LGyz[Rho_, Phi_, z_, ScriptL_, a_, b_] :=
    Exp[I ScriptL Phi] (-1/2) NIntegrate[ Sqrt[Cos[Theta]] Sin[Theta]^2
     *lg[(Sin[Theta]/Sin[Alpha]), ScriptL] Exp[I k z Cos[Theta]]
      *(BesselJ[ScriptL + 1, k Rho Sin[Theta]] Exp[I Phi]
       +BesselJ[ScriptL - 1, k Rho Sin[Theta]] Exp[-I Phi])*
     ,{Theta, a, b}];
```

Beam calculation

```
(*Calculation of the focused fields*)
Ef[xmax_, dx_, z_ ScriptL_, NA_, n_] :=
  Block[{EXx, EXy, EXz, EYx, EYy, EYz, Alpha = ArcSin[NA/n]},
   EXx = ParallelTable[ LGxx[Sqrt[x^2 + y^2], ArcTan[x, y], z, ScriptL, 0, Alpha],
        {y, -xmax, xmax, dx}, {x, -xmax, xmax, dx}];
   EXy = ParallelTable[ LGxy[Sqrt[x^2 + y^2], ArcTan[x, y], z, ScriptL, 0, Alpha],
        {y, -xmax, xmax, dx}, {x, -xmax, xmax, dx}];
   EXz = ParallelTable[ LGxz[Sqrt[x^2 + y^2], ArcTan[x, y], z, ScriptL, 0, Alpha],
```

```
        {y, -xmax, xmax, dx}, {x, -xmax, xmax, dx}];
   EYx = ParallelTable[ LGyx[Sqrt[x^2 + y^2], ArcTan[x, y], z, ScriptL, 0, Alpha],
        {y, -xmax, xmax, dx}, {x, -xmax, xmax, dx}];
   EYy = ParallelTable[ LGyy[Sqrt[x^2 + y^2], ArcTan[x, y], z, ScriptL, 0, Alpha],
      {y, -xmax, xmax, dx}, {x, -xmax, xmax, dx}];
   EYz = ParallelTable[ LGyz[Sqrt[x^2 + y^2], ArcTan[x, y], z, ScriptL, 0, Alpha],
      {y, -xmax, xmax, dx}, {x, -xmax, xmax, dx}];
   Return[{EXx, EXy, EXz, EYx, EYy, EYz}]
   ];

(*Constructing the arbitrary polarised*)
Ep[E_, Alpha_, Beta_] := {Cos[Alpha]*E[[1]] + Sin[Alpha] Exp[I Beta]*E[[4]],
                          Cos[Alpha]*E[[2]] + Sin[Alpha] Exp[I Beta]*E[[5]],
                          Cos[Alpha]*E[[3]] + Sin[Alpha] Exp[I Beta]*E[[6]]};
```

Toolbox for visualization

```
(*Phase distribution*)
Ph[Psi_] :=
  ListDensityPlot[Arg[Psi], ColorFunction -> (Hue[Rescale[#, {0, 2 Pi}, {0, 1}]] &),
   PlotRange -> All, ColorFunctionScaling -> False, Frame -> None,
   DataRange -> {{-1.5, 1.5}, {-1.5, 1.5}},
   BoundaryStyle -> Directive[Transparent, Thick],
   RegionFunction -> Function[{x, y, f}, (x)^2 + (y)^2 < 2]];

(*Intensity distribution*)
Int[Psi_] :=
  ListDensityPlot[Abs[Psi]^2, ColorFunction -> ColorData["AvocadoColors"], PlotRange ->
     All,
   Frame -> None, DataRange -> {{-1.5, 1.5}, {-1.5, 1.5}},
   BoundaryStyle -> Directive[Transparent, Thick],
   RegionFunction -> Function[{x, y, f}, (x)^2 + (y)^2 < 2]];

k = 2 Pi;

lg[Rho_, ScriptL_] := Rho^Abs[ScriptL] Exp[-Rho^2];
```

A.2 Python

A.2.1 Main code

```
# Loading the libraries
import numpy as np
import scipy
import scipy.interpolate
import cmath
import matplotlib.pyplot as plt

#Tightly focusing a single-ringed Laguerre-Gauss beam with topological charge l.
# l    -   Topological charge of the LG mode
# xmax -   Half length of the numerical window
# kk   -   Frequency scaling factor for different wavelengths
# z    -   Plane of interest in the focal volume
# N    -   Number of points per dimension
# NA   -   Numerical aperture of the applanatic lens
# n    -   Refractive index of the medium in which the focusing occurs
# pol  -   Polarization parameters pol=[alpha,beta] in E=Cos(alpha)Ex+Sin(alpha)exp(i beta
    ) Ey

def FocusLG(l,xmax,z,N,NA,n,pol,):
  # Wavenumber
  k=2*np.pi*kk

  # Defining Position Domain
  xx=np.linspace(-xmax,xmax,N)
  X, Y = np.meshgrid(xx, xx)
  varphi=np.arctan2(Y,X)
  r=np.sqrt(X**2+Y**2)

  # Refence sphere domain
  THETA=np.linspace(0,np.arcsin(NA/n),N)
  dth=np.abs(THETA[0]-THETA[2]);
  R=np.linspace(0,np.max(r),N)
  RR,TT=np.meshgrid(R,THETA)

  # Mapping r to the sphere coordinates
  rp=np.sin(TT)/(np.sin(NA/n))

  # Shared term for each integral
  K= np.sqrt(np.cos(TT))*np.sin(TT)*(rp**np.abs(l))*np.exp(-(rp/(np.sqrt(2)))**2)*np.exp(1
      j*k*z*np.cos(TT))

  # Numerical integration
  I1=scipy.interpolate.CubicSpline(R,dth*np.sum(K*(1+np.cos(TT))*scipy.special.jv(l,k*RR*
      np.sin(TT)),0))
  I2=scipy.interpolate.CubicSpline(R,dth*np.sum(K*(1-np.cos(TT))*scipy.special.jv(l+2,k*RR
```

```
    *np.sin(TT)),0))
I3=scipy.interpolate.CubicSpline(R,dth*np.sum(K*(1-np.cos(TT))*scipy.special.jv(l-2,k*RR
    *np.sin(TT)),0))
I4=scipy.interpolate.CubicSpline(R,dth*np.sum(K*np.sin(TT)*scipy.special.jv(l+1,k*RR*np.
    sin(TT)),0))
I5=scipy.interpolate.CubicSpline(R,dth*np.sum(K*np.sin(TT)*scipy.special.jv(l-1,k*RR*np.
    sin(TT)),0))

# Individual Cartesian components construction
Exx= (1j**l)*np.exp(1j*l*varphi)*( I1(r)+0.5*np.exp(1j*2*varphi)*I2(r)+0.5*np.exp(-1j*2*
    varphi)*I3(r))
Exy=-0.5*(1j**(l-1))*np.exp(1j*l*varphi)*(-np.exp(1j*2*varphi)*I2(r)+np.exp(-1j*2*varphi
    )*I3(r))
Exz=(1j**(l+1))*np.exp(1j*l*varphi)*( np.exp(1j*varphi)*I4(r)-np.exp(-1j*varphi)*I5(r))
Eyx=Exy;
Eyy=(1j**l)*np.exp(1j*l*varphi)*( I1(r)-0.5*np.exp(1j*2*varphi)*I2(r)-0.5*np.exp(-1j*2*
    varphi)*I3(r))
Eyz=(1j**(l))*np.exp(1j*l*varphi)*( np.exp(1j*varphi)*I4(r)+np.exp(-1j*varphi)*I5(r))

# Output field
Ex=np.cos(pol[0])*Exx+np.exp(1j*pol[1])*np.sin(pol[0])*Exy
Ey=np.cos(pol[0])*Exy+np.exp(1j*pol[1])*np.sin(pol[0])*Eyy
Ez=np.cos(pol[0])*Exz+np.exp(1j*pol[1])*np.sin(pol[0])*Eyz

return Ex, Ey, Ez
```

Appendix B

Supplementary Materials: Optical knots as information carriers

Supplementary Information for:
Optical Framed Knots as Information Carriers

Larocque et al.

SUPPLEMENTARY FIGURES

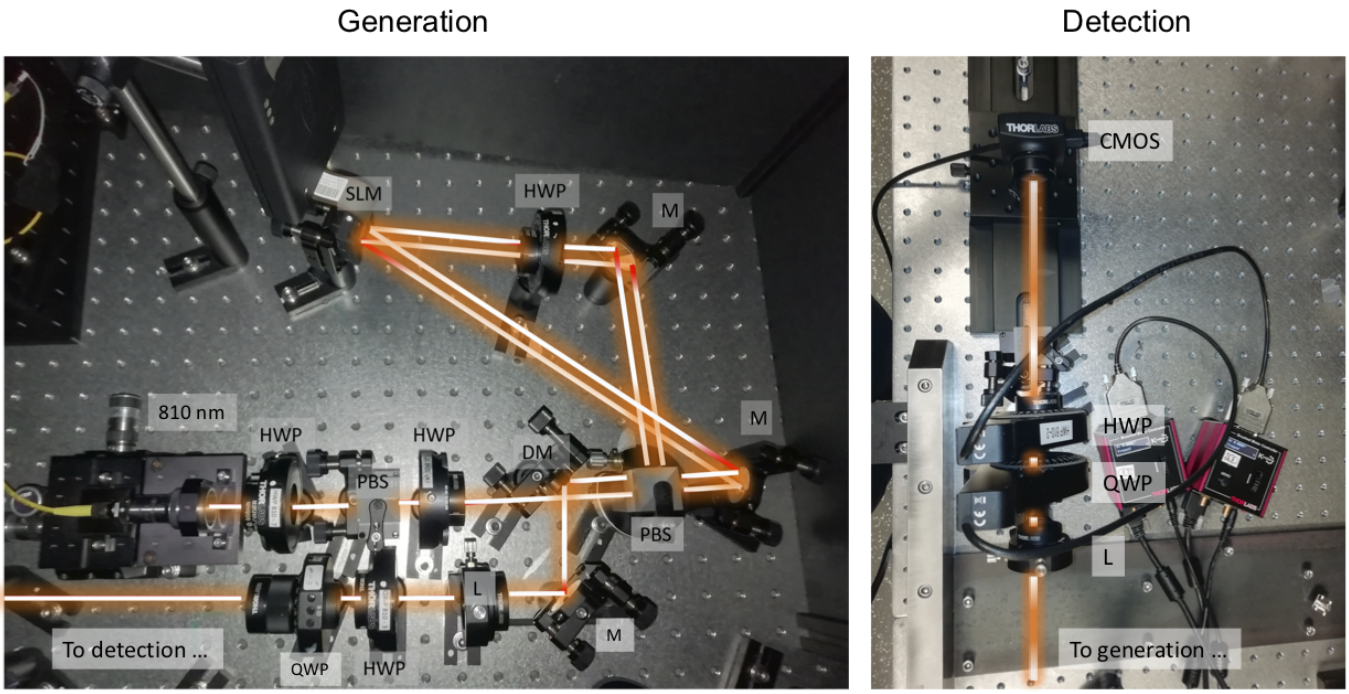

Supplementary Figure 1. **Photo of the experimental setup.** Left: Knot generation component of the setup. Right: Knot detection component of the setup. Figure legend: HWP: half-wave plate, PBS: polarizing beam splitter, M: mirror, SLM: spatial light modulator, DM: D-shaped mirror, L: lens, QWP: quarter-wave plate, CMOS: complementary metal–oxide–semiconductor camera.

SUPPLEMENTARY NOTE 1: POLYNOMIAL REPRESENTATION OF NON-PARAXIAL KNOTS

Here, we provide the formulation of the non-paraxial trefoil knotted ribbon displayed in Fig. 1 of the main text. To do so, we follow the derivation of the non-paraxial trefoil knot performed in [1]. Assuming that the electric field is circularly polarized ($\mathbf{e}_- = (\mathbf{x} - i\mathbf{y})/\sqrt{2}$), one can start this derivation with the knotted paraxial field [2]

$$E_-^{\text{par}} = (1 - R^2 - R^4 + R^6 - 8e^{3i\phi}R^3) - 2iZ - 8iR^2Z + 18iR^4Z + 8Z^2 - 72R^2Z^2 - 48iZ^3, \tag{1}$$

where $R = krs^{-1}$ and $Z = kzs^{-2}$, (r, ϕ, z) are the cylindrical coordinates, k is the wave vector, and s is a scaling parameter. An $s \gg 1$ value corresponds to the paraxial regime, whereas an $s \approx 1$ entails non-paraxial behavior. Gauss' law determines the z component of the paraxial field, which is given by

$$E_z^{\text{par}} = -\sqrt{2}is^{-1}Re^{-i\phi}[1 + 2R^2 - 3R^4 + 24Re^{3i\phi} + 4iZ(2 - 9R^2) + 72Z^2] + O(s^{-2}), \tag{2}$$

where higher orders in s^{-1} are ignored given that $s \gg 1$ for paraxial waves. One can then use Supplementary Equation 1 in conjunction with Bessel polynomials [3] to determine a generalized formulation of the trefoil knot accounting for non paraxial behavior. Doing so yields the field $\mathbf{E}^{\text{k}} = E_-^{\text{k}}\,\mathbf{e}_- + E_z^{\text{k}}\,\mathbf{z}$, where

$$E_-^{\text{k}} = E_-^{\text{par}} + s^{-2}[8i(1 + 18s^{-2} - 9R^2)Z + 144Z^2]. \tag{3}$$

Gauss' law is then also used to derive the z component of the generalized field, which yields,

$$E_z^{\text{k}} = E_z^{\text{par}} + 4\sqrt{2}iRe^{-i\phi}s^{-3}[2 + 54s^{-2} - 9R^2 - 54iZ], \tag{4}$$

where all orders of s are now included. The knot considered in Fig. 1 of the main text is defined by $s = 4.5$. Note that these components are expressed in terms of polynomial beams [3]. Though they do consist of full solutions to Maxwell's equations,

they carry an infinite amount of energy and are thus not deemed physical. Nonetheless, the dynamics of these beams can still hold in physically realizable systems provided that the extent of the field enclosing the beam's vortices is large enough [1, 2]. More specifically, the diffraction length of the enclosing field, which could be a Gaussian beam for instance, must exceed the length over which the knot is formed in the polynomial beam.

We then proceed by coherently adding a left-circular polarized plane wave, to the above non-paraxial field. Given the polynomial nature of our analysis, we choose to represent this additional component as a complex constant. This component is represented by the E_+^{p} structure shown in Fig. 1c of the main text. This results in the formation of a complex vector field $\mathbf{E}(\mathbf{r}) = (E_x(\mathbf{r}), E_y(\mathbf{r}), E_z(\mathbf{r}))$ which can be expressed as [4, 5]:

$$\mathbf{E} = |\mathbf{E}|\,(\mathbf{A} + i\mathbf{B})\exp(i\epsilon), \tag{5}$$

where $|\mathbf{E}|$ is the amplitude of the field, $\mathbf{e} = \mathbf{A} + i\mathbf{B}$ is a complex vector representing the polarization ellipse traced by the electric field, and ϵ is a phase that is set such that $\mathbf{A}$ and $\mathbf{B}$ represent the major and minor axes of the polarization ellipse, respectively. Note that the scalar $\mathbf{e}\cdot\mathbf{e}$ represents the eccentricity of the polarization ellipse and is minimized for circular polarization where $\mathbf{e}\cdot\mathbf{e} = 0$ [5]. Furthermore, the orientation of $\mathbf{A}\times\mathbf{B}$ provides the vector normal to the oscillation plane of the polarization ellipse. We use these two quantities to reconstruct the frame of the C-line of the fields in Fig. 1 of the main text by first localizing the field's knotted C-line through regions where $\mathbf{e}\cdot\mathbf{e} = 0$. The results of this process are depicted in Fig. 1d of the main text. We then find the tangent and the $\mathbf{A}\times\mathbf{B}$ vector along this C-line. As discussed in the main text, taking the cross product of these two quantities allows us to obtain the knot's frame. Examples of the frames constructed from this method are shown in Fig. 1e of the main text. At this point, a few remarks can be made regarding the interplay between the knotted field $\mathbf{E}^{\mathrm{k}}$ and the plane wave E_+^{p}. On its own, $\mathbf{E}^{\mathrm{k}}$ has C-lines located by default along the nulls of the E_z field. The coherent addition of E_+^{p} deforms the C-line into a knot within the proximity of the one formed by E_-^{k}. When the amplitude of this additional field is increased, the knotted C-line gradually adopts the shape of the E_-^{k} knot and its frame experiences less influence from E_z^{k}. The formation of the C-lines in $\mathbf{E}_{\mathrm{k}}$ and how they are deformed by the addition of E_+^{p} are depicted in Figs. 1c,d of the main text, respectively. The normal of the circular polarization vector then gradually aligns itself to the beam's direction of propagation, z, thereby reducing the presence of z components in the C-line's framing illustrated in Fig. 1e of the main text. Note that expressing the amplitude of the field of E_+^{p} relative to $\mathbf{E}^{\mathrm{k}}$ becomes an ill-defined task because the depicted fields are formed with polynomial beams [3], which are not normalizable. We therefore abstain from relatively expressing the amplitude of E_+^{p} by simply expressing both fields as polynomials.

The sudden transition observed between the topologies of the C-lines formed with $E_+^{\mathrm{p}} = 0$ and $E_+^{\mathrm{p}} = 5$ further elucidates the importance of E_+^{p} in our framed knots' construction. Given that a knotted C-line formed with $\left|E_+^{\mathrm{p}}\right| = 0$ is entirely determined by the topology of E_z^{k} whereas that formed with $\left|E_+^{\mathrm{p}}\right| \gg 0$ is entirely determined by the topology of E_-^{k}, then there exists a range of $\left|E_+^{\mathrm{p}}\right|$ where the topology of the knotted C-line becomes unstable as it transitions from one form to the other. Note that such transitions are of little practical importance for structures realized within paraxial fields given the negligible presence of the z-polarized field.

SUPPLEMENTARY NOTE 2: LOW DIMENSIONAL TOPOLOGY

Combinatorial knot theory studies knots as planar diagrams instead of as embedded objects in 3–space. These diagrams are decomposed into tangles [6]. Knots and tangles are modified by *local moves*, which replace one tangle within a knot by another. Knots are thus revealed to be algebraic objects arising as concatenations of crossings (which are very simple tangles) in the plane [7].

The combinatorial paradigm of knot theory manifests a new philosophy of what constitutes algebra. For the combinatorial knot theorist, algebra no longer consists merely of formal manipulations of strings of symbols, but rather of operations and local modifications of labeled figures in the plane and in higher dimensions. This philosophy of diagrammatic algebra has become particularly well established in the representation theory of quantum groups, in higher category theory, and in quantum field theory [8–11].

Two planar diagrams are considered equivalent if one may be transformed into the other through a series of local deformations known as the Reidemeister moves, referring to the three kinds of archetypal manipulations shown in Supplementary Figure 2,

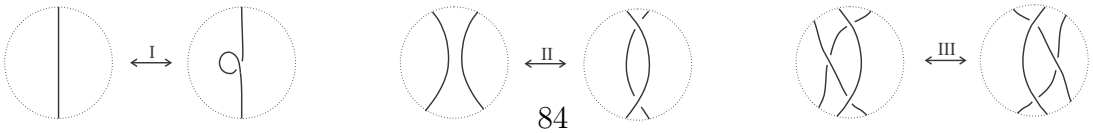

Supplementary Figure 2. Diagrammatic representations of the three Reidemeister moves.

In this work we chiefly care about framed knots and more broadly knotted ribbons (see Supplementary Figure 3). Mathematically speaking, they are embeddings of the solid torus in 3-sphere.

Definition 1 *A framed knot* (K, V) *in* S^3 *is a knot* K*, i.e., an embedding of* S^1*, equipped with a vector field* V *called a framing.*

The framing is characterized by a number, the *framing integer*, which is the linking number of the image of the ribbon $I \times S^1$ with the knot. In other words, it counts the number of times the vector field twists (2π rotations) around the knot. Knotted ribbons generalize framed knots to an odd number of half-twists, e.g., knotted Möbius bands.

The planar diagrams of knotted ribbons are respectively equipped with a (blackboard) framing representing the number of half-twists along the ribbon. The Reidemeister type-I move clearly changes the framing while the two other moves preserve it. For that reason, two knotted ribbons are considered equivalent if one may be transformed into the other by a sequence of type-II and type-III moves only, though it is worthwhile noting that a modified type-I move may be introduced which preserves the framing.

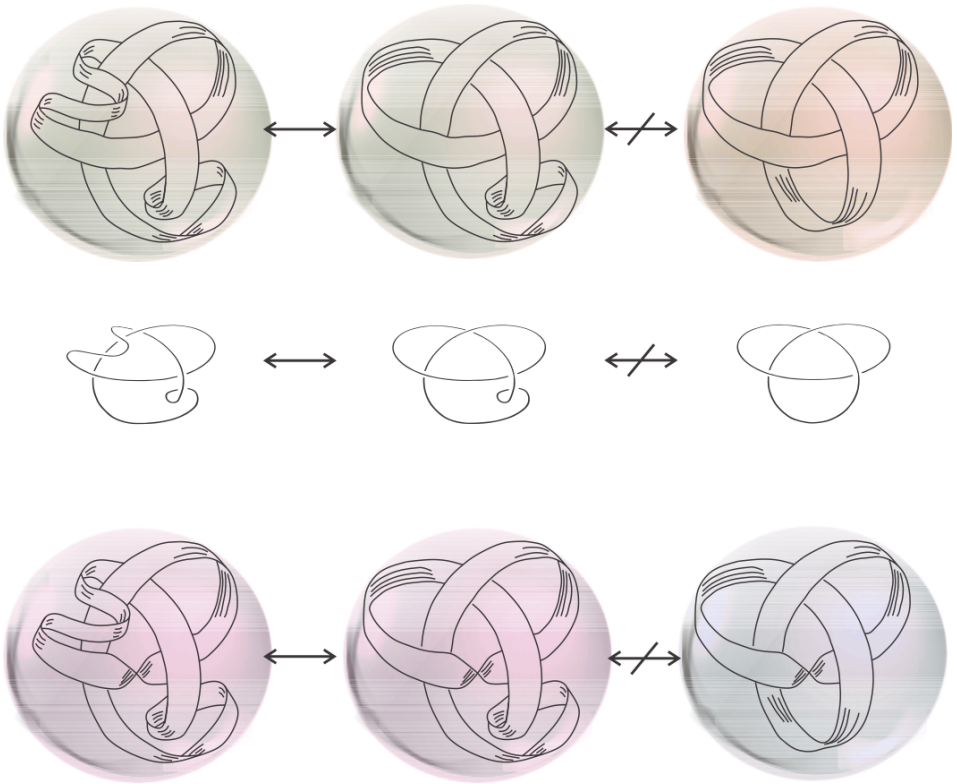

Supplementary Figure 3. **Equivalence of framed knots and ribbons.** The two leftmost framed trefoil knots in the upper row are equivalent for they are related by a Reidemeister type-II move. To their right is another, though not equivalent, framed trefoil (it lacks the full twist, the Reidemeister-I deformation, shared by the two other). The corresponding planar diagrams (excluding blackboard framing) are shown in the middle row. The bottom row illustrates three knotted ribbons – they all have an odd number (3) of half-twists. The two leftmost knotted ribbons are related by a Reidemeister type-II move whereas the one on the right is not equivalent to any of them (for it lacks the half-twist).

Braids are yet another family of tangles which, much like framed knots, are invariant to type-II and type-III moves. For a matter of fact, braids are purely algebraic entities defined via fundamental groups of a configuration space. The braid group on n strands, $\mathcal{B}_n$, consists of $n-1$ generators (represented as crossings between two nearby strands) and relations encoding the possible type-III moves. The type-II move is manifested by concatenating generators with their inverses.

Every knot may be represented as the closure of some braid (due to Alexander's theorem), namely, by attaching pairs of corresponding string ends in the braid. Similarly, every framed knot may be represented as the closure of some framed braid.

SUPPLEMENTARY NOTE 3: KNOTTED RIBBONS AND FRAMED KNOTS AS INFORMATION CARRIERS

As carriers of information, knotted objects may exhibit greater resilience to environmental disturbances than conventional data structures. The information content – the myriad of topological invariants – is generally insensitive to many of the deformations occurring when topological objects are materialized and handled. This section describes an approach, reminiscent of integer

factorization, that allows representing a number by a knotted ribbon or a framed knot in such as a way that its respective framed braid representation corresponds to the prime factorization of that number.

A. The framed braid group and its representation

We begin with the following observation concerning braid representations. As already pointed out, every unframed knot has a braid representation, i.e., a braid whose closure is that knot. The braid representation is not unique for there may be other braids whose closure is the same knot. These different braid representations are related by two types of local deformations known as Markov moves, i.e., the braid representation is in fact an equivalence class.

A framed knot, and more generally a closed knotted ribbon, likewise admits a framed braid representation, i.e., a framed braid whose closure is equivalent to the knotted ribbon. But in this case, we face an irreducible arbitrariness in the construction of the braid representation; there is more than one way to specify a framing for a braid from which a particular knotted ribbon is formed. Another way to see this is to imagine how half-twists are slided along the knotted ribbon such that every time it is cut into the same set of strands a different framed braid is formed.

Here we supplement the knotted ribbon with additional information, a pair of real numbers (α,β), that allows uniquely recovering its framed braid representation. The idea is analogous to prime factorization of integers; with the aid of (α,β) the knotted ribbon represents a natural number while the framed braid is akin to the (unique) prime factorization of this number.

A framed braid with n strands is a word in the group [12]

$$\mathcal{FB}_n = \left\langle \sigma_1,\ldots,\sigma_{n-1},\tau_1,\ldots,\tau_n \,\middle|\, \begin{array}{l} \sigma_{j+1}\sigma_j\sigma_{j+1} = \sigma_j\sigma_{j+1}\sigma_j, \\ \tau_i\tau_j = \tau_j\tau_i, \\ \tau_{j+1}\sigma_j = \sigma_j\tau_j,\ \sigma_j\tau_{j+1} = \tau_j\sigma_j \\ \sigma_i\sigma_j = \sigma_j\sigma_i,\ \tau_i\sigma_j = \sigma_j\tau_i \end{array} \right\rangle \tag{6}$$

where the second to last relation holds for $|i-j|>1$. The σ_j is the braiding generator of the jth and $(j+1)$th strands, and τ_j is the twisting generator of the jth strand. The generators and relations of the framed braid group are illustrated in Supplementary Figure 4.

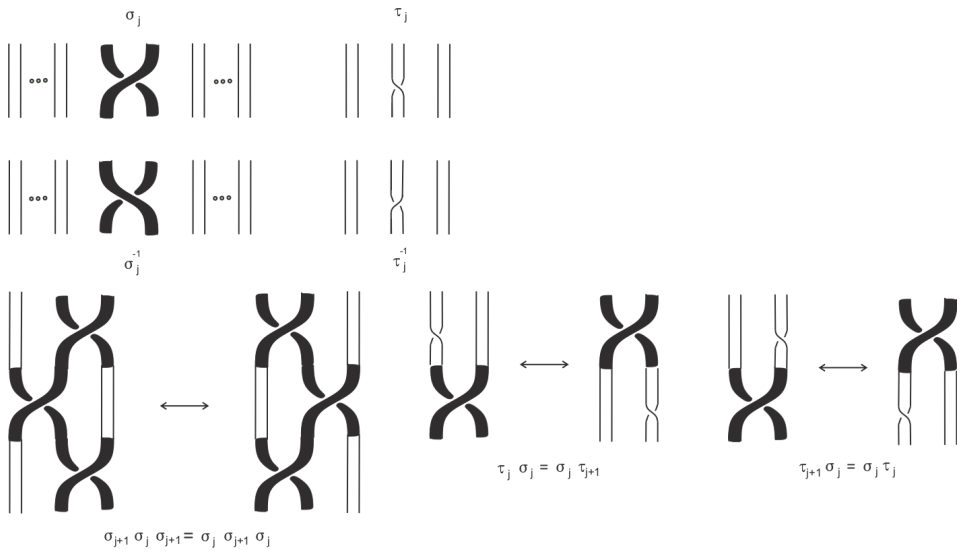

Supplementary Figure 4. **Generators and relations of the framed braid group, $\mathcal{FB}_n$.**

An unframed braid of n strands may act on the composite Hilbert space $\mathcal{H}^{\otimes n}$. The braid generators σ_j correspond to braiding operators,

$$R_j = \mathbb{1}^{\otimes(j-1)} \otimes R \otimes \mathbb{1}^{\otimes(n-j-1)} \tag{7}$$

where $\mathbb{1}$ is the identity operator, and R, a unitary operator on $\mathcal{H}\otimes\mathcal{H}$ that satisfies the Yang-Baxter equation,

$$(R\otimes\mathbb{1})(\mathbb{1}\otimes R)(R\otimes\mathbb{1}) = (\mathbb{1}\otimes R)(R\otimes\mathbb{1})(\mathbb{1}\otimes R) \tag{8}$$

As was shown in [13], this R may be an entangling operator acting on the composite system, e.g., $R|00\rangle = (|00\rangle + |11\rangle)/\sqrt{2}$.

A framed braid, $\mathcal{F}_n \times \mathcal{B}_n$, acts on the composite Hilbert space $\mathcal{H}^{\otimes n} \otimes \mathcal{H}^{\otimes n}$. This time the braiding operator R_j acts on the first (framing) space as a swap gate and as an entangling operator on the second (braid) space. In particular, it assumes the form

$$R_j = \left[\mathbb{1}^{\otimes(j-1)} \otimes \mathrm{SWAP} \otimes \mathbb{1}^{\otimes(n-j-1)}\right] \otimes \left[\mathbb{1}^{\otimes(j-1)} \otimes R \otimes \mathbb{1}^{\otimes(n-j-1)}\right] \tag{9}$$

The twisting operator corresponding to τ_j is the self-adjoint

$$T_j = \left(\sum_{k\neq j} |k\rangle\langle k| + \alpha|j\rangle\langle j|\right) \otimes \mathbb{1}^{\otimes n} \tag{10}$$

where the kets, $|k\rangle$, $k = 1, \ldots, n$, span the framing space, and α is some real positive number. It can be verified that R_j and T_j thus defined satisfy the relations of $\mathcal{FB}_n$.

B. Framed braids and prime factorization

The framed braid group admits a natural representation in Hilbert space. Because the two spaces (the framing and the braiding) do not interact, we may take the trace of each one of them separately. Consider a framed braid, a word w in the group $\mathcal{FB}_n$, whose representation is $A(w)$. The framing space of $A(w)$ is obtained by tracing over the braid space,

$$F(w) = \mathrm{Tr}_{\mathcal{B}}\left[A(w)\right] = \sum_{\{k|d_k\neq-\infty\}} \alpha^{d_k}|k\rangle\langle k| \tag{11}$$

where d_k is the number of half-twists along the kth strand exhibiting half-twists, i.e., $d_k = -\infty$ for untwisted strands. If we now assign a *distinct* prime p_k with each such strand while constraining α to positive integers, then the framed braid may be thought of as representing the prime factorization of some natural number encoded by the underlying framed knot. Here, we define this number as

$$N_{\alpha,\beta}(M) \stackrel{\mathrm{def}}{=} \beta^{(\alpha^M)} = \prod_{\{k|d_k\neq-\infty\}} p_k^{(\alpha^{d_k})} \tag{12}$$

where,

$$M = \log_\alpha \mathrm{Tr}\left[F(w)\log_\beta P\right] = \log_\alpha\left(\sum_{\{k|d_k\neq-\infty\}} \alpha^{d_k}\log_\beta p_k\right) \tag{13}$$

is the corresponding number of half-twists in the associated knotted ribbon (as every half twist, by definition, amounts to multiplication by α), and $P = \sum_k p_k|k\rangle\langle k|$ is the corresponding prime association matrix.

The number of half-twists in the braid representation amounts to that in the framed knot, $M = \sum_{\{k|d_k\neq-\infty\}} d_k$, which determines the logarithm basis as

$$\beta = \prod_{\{k|d_k\neq-\infty\}} p_k^{(\alpha^{d_k-M})} \tag{14}$$

The number $N_{\alpha,\beta}(M)$ is determined exclusively by the number of half-twists, M, in a the knotted ribbon and the pair (α,β). In other words, given α and β, this number is a topological invariant of the knotted ribbon. The prime factorization of $N_{\alpha,\beta}(M)$ encodes the number of half-twists per strand in the framed braid representation of the knotted ribbon. This encoding scheme is depicted in Supplementary Figure 5, which consists of the symbolic representation of Supplementary Equation 12.

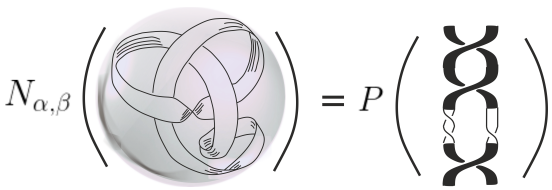

Supplementary Figure 5. **Symbolic representation of the prime encoding of a framed braid.** The prime factorization, P, of a framed braid corresponds to that of the integer $N_{\alpha,\beta}(M)$, which is determined by the pair (α,β) and the framed knot attributed to the braid.

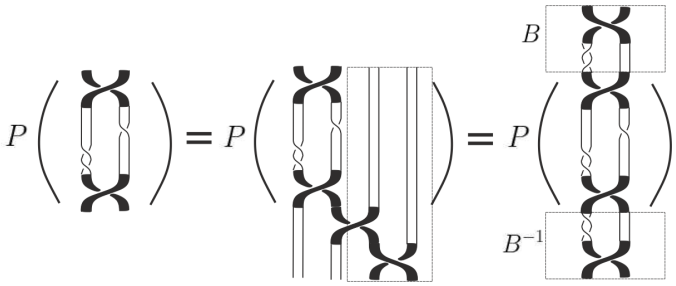

Supplementary Figure 6. **Markov moves attributed to framed braids.** The prime factorization of a framed braid (left) remains the same as the braid experiences stabilization (center) or conjugation (right).

As previously noted, the braid representation of a knot is not unique. Braid representations of the same knot are related by two kinds of Markov moves known as *stabilization* and *conjugation*. The same applies to knotted ribbons as long as the number of half-twists remains unchanged by these moves. As shown in Supplementary Figure 6, this invariance is carried over to the prime factorization captured by the framed braid. The left identity is stabilization – the act of adding untwisted strands, possibly interacting through Reidemeister-I moves, – which here amounts to padding the prime factorization with 1's, i.e., no half-twists are introduced by the newly added strands (primes). Note that there must be as much Reidemeister-I moves as their inverses for otherwise the number of half-twists would change. Similarly, conjugation of a braid A, i.e. the newly formed braid, BAB^{-1} on the right of Supplementary Figure 6, where $BB^{-1} = B^{-1}B = I$ is the framed unbraid, has the same number of half-twists as A, hence also the same prime factorization.

C. Some properties of $N_{\alpha,\beta}$

The number $N_{\alpha,\beta}(M)$ is a topological invariant of a knotted ribbon with M half-twists. Equivalent knotted ribbons necessarily have the same number $N_{\alpha,\beta}$ for a given pair (α,β). The converse clearly does not hold true; different knotted ribbons may be conceived having the same number $N_{\alpha,\beta}(M)$.

The role of $N_{\alpha,\beta}$ in the reconstruction of framed braids from knotted ribbons may be appreciated by considering the following scenario. Alice would like to send Bob a message which is here obtained as an output of a certain program running on some initial inputs, the set of numbers, d_k, $k = 1, 2, \ldots, n$. The program itself is a sequence of operations each taking as inputs some of these numbers or the outputs obtained by preceding operations. Running the program with the set of initial inputs is expected to yield Alice's message.

Alice conceives her program and its inputs as a framed braid. She identifies an operation with a sequence of crossings in the braid's planar diagram while the initial inputs are taken as the number of half-twists per strand. Alice has her program completely specified by the n-strand framed braid representation of her knotted ribbon K_A. To maintain some degree of privacy, she would like to send Bob her K_A rather than the original framed braid. She takes note of the fact that K_A may be complicated by a series of Reidemeister-II and III moves which would somewhat conceal the original framed braid. She proceeds by performing the following steps.

1. Choose a positive integer α.
2. Determine the framed braid representation of K_A; Allocate the number of half-twists in K_A to different strands of the braid, i.e., set d_k such that $M_A = \sum_k d_k$ is the total number of half-twists in K_A.
3. Assign prime numbers p_k to strands exhibiting half-twists.
4. Determine the number β according to Supplementary Equation 14.

Alice then sends Bob her knotted ribbon K_A and the pair of numbers α and β. Upon receiving these, Bob proceeds by computing $N_{\alpha,\beta}(M_A)$ whose prime factorization unfolds d_k. He can now recover an equivalent of the encoded framed braid from step (2) above.

SUPPLEMENTARY NOTE 4: DERIVATION OF THE PARAMETRIZED KNOTTED FIELD

88

We follow the method outlined in [14] to construct the knotted fields of the optical beams used in this work. We start by parametrizing the transverse coordinates of the braid representation of the trefoil and cinquefoil knots with respect to the height

coordinate $h \in [0, 2\pi]$. The Cartesian representation of these coordinates is given by:

$$X_j^r(h) = a\cos\left(\frac{1}{2}[rh + 2\pi(j-1)]\right), \qquad Y_j^r(h) = b\sin\left(\frac{1}{2}[rh + 2\pi(j-1)]\right), \tag{15}$$

where $i = \sqrt{-1}$, $j = 1, 2$ refers to one of the two strands in the braid, a and b are postive scaling constants, and $r = 3, 5$ for the trefoil and cinquefoil knots, respectively. We then express these coordinates in terms of $v = \exp(ih)$, thereby yielding

$$X_j^r(v) = \frac{a}{2}\left(v^{r/2}e^{i\pi(j-1)} + v^{*r/2}e^{-i\pi(j-1)}\right), \qquad Y_j^r(v) = \frac{b}{2i}\left(v^{r/2}e^{i\pi(j-1)} - v^{*r/2}e^{-i\pi(j-1)}\right), \tag{16}$$

where $v^* = \exp(-ih)$. We then express the braid as the roots of the following complex polynomial

$$p_v^r(u) = \prod_{j=1}^{2}(u - Z_j^r(v)) \tag{17}$$

where $Z_j^r(v) = X_j^r(v) + iY_j^r(v)$ and $u = x + iy$ is a complex value expressed in terms of the transverse Cartesian coordinates (x, y). We may then convert this polynomial into a complex field with knotted complex roots. This task is achieved with the stereographic projection

$$u = \frac{\rho^2 + z^2 - 1 + 2iz}{\rho^2 + z^2 + 1}, \qquad v = \frac{2\rho e^{i\varphi}}{\rho^2 + z^2 + 1}, \tag{18}$$

where (ρ, φ, z) refer to the cylindrical coordinates of the space in which the knot is embedded. Note that this projection effectively maps the h coordinate of the space in which the braid is embedded to the φ coordinate of the knot. For the cases of the trefoil ($r = 3$), and cinquefoil ($r = 5$) knots, the numerator of this expression at the $z = 0$ plane are respectively given by

$$p^{r=3}(\rho, \varphi, z = 0) = 1 - \rho^2 - 4(a^2 - b^2)\rho^3 - \rho^4 + \rho^6 - 2(a-b)^2\rho^3 e^{-3i\varphi} - 2(a+b)^2\rho^3 e^{3i\varphi}, \tag{19}$$

$$p^{r=5}(\rho, \varphi, z = 0) = 1 + \rho^2 - 2\rho^4 - 16(a^2 - b^2)\rho^5 - 2\rho^6 + \rho^8 + \rho^{10} - 8(a-b)^2\rho^5 e^{-5i\varphi} - 8(a+b)^2\rho^5 e^{5i\varphi}. \tag{20}$$

As demonstrated in Supplementary Figure 7a, reducing the b parameter of Eqs. (19,20) compresses the braid along the y direction. For the knot obtained from the projection of this braid, the observed compression is now along z, thereby resulting in a shorter knot. This corresponding compression is displayed in Supplementary Figure 7b,c. As further discussed in Supplementary Note 5, this compression property can be used to stabilize the frame of the knots generated in this work.

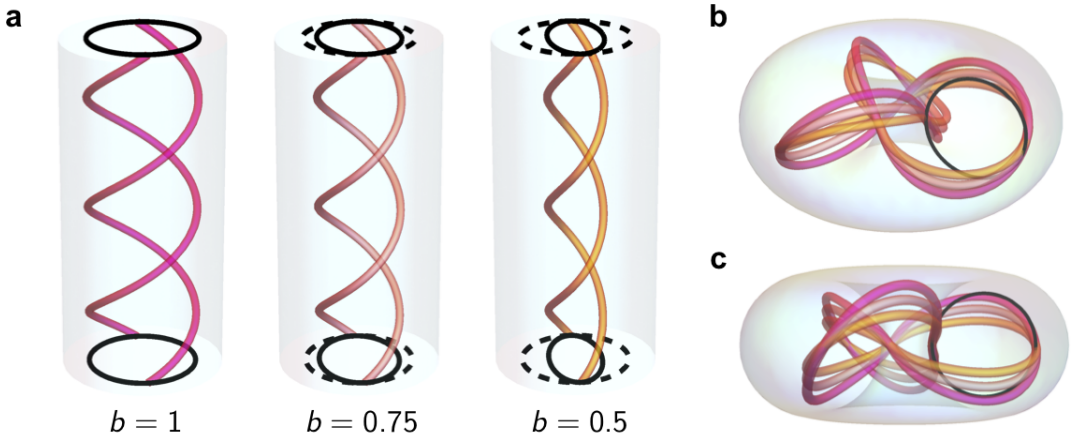

Supplementary Figure 7. **Effect of reducing the b parameter of the knot's parametrization. a,** Braids formed by the zeros of the complex polynomial defined in Supplementary Equation 17 with $r = 3$ and $a = 1$. The solid ellipses at the ends correspond to the ones traced out by the strands of the braids. The dashed ellipses are traced out by the braid with $b = 1$. **b,** Corresponding knots formed by the stereographic projection of the braids shown in (**a**) as prescribed by Supplementary Equation 18. **c,** Side view of the knot shown in (**b**) emphasizing the compression induced by a decreasing b parameter.

To obtain the optical fields $\psi_{a,b,s}^{\text{Tref}}(\varrho, \varphi)$ and $\psi_{a,b,s}^{\text{Cinq}}(\varrho, \varphi)$ provided in the main text, we take the projections from Eqs. (19,20), and let $\rho \mapsto \varrho$, where $\varrho = \rho/w_0$ is a dimensionless counterpart to the cylindrical radial coordinate ρ and w_0 refers to a scaling

factor. We then define the optical fields as the stereographic projections modulated by a Gaussian function, i.e. $\psi^{r}_{a,b,s}(\varrho,\varphi) = p^{r}(\varrho,\varphi)\,\exp\left(-(\varrho/s)^2/2\right)$, thereby resulting in the field formulations presented in the main text:

$$\psi^{\mathrm{Tref}}_{a,b,s}(\varrho,\varphi,z=0) = (1-\varrho^2-4(a^2-b^2)\varrho^3-\varrho^4+\varrho^6-2(a-b)^2\varrho^3e^{-3i\varphi}-2(a+b)^2\varrho^3e^{3i\varphi})\,e^{-(\varrho/s)^2/2}, \tag{21}$$

$$\psi^{\mathrm{Cinq}}_{a,b,s}(\varrho,\varphi,z=0) = (1+\varrho^2-2\varrho^4-16(a^2-b^2)\varrho^5-2\varrho^6+\varrho^8+\varrho^{10}-8(a-b)^2\varrho^5e^{-5i\varphi}-8(a+b)^2\varrho^5e^{5i\varphi})\,e^{-(\varrho/s)^2/2}. \tag{22}$$

SUPPLEMENTARY NOTE 5: RESILIENCE OF THE FRAME

The effect of reducing the b value of the knot's parametrization can also be seen in the optical knots presented in this work. To illustrate, we consider the propagation of space-varying polarized light beams that can be conveniently expressed as the coherent superposition of two components in the circular polarization basis. As shown in Fig. 3b of the main text, the left circular polarization term is defined by a large Gaussian beam. The right circular polarization component consists of the scalar fields shown in Supplementary Figure 8a. In the latter, we observe that the field's phase vortices become progressively asymmetric as b is decreased. This asymmetry causes the resulting polarization field of the beam to experience a contraction in the C-line forming a knotted structure. The contraction, displayed in the theoretical optical knots of Supplementary Figure 8b, is observed to be along the beam's longitudinal, z, direction. Furthermore, the motion of the C-line in the transverse plane, xy, becomes a lot more definitive. The knots formed by experimental structures with the same parameters are illustrated in Supplementary Figure 8c. Though not as pronounced as their theoretical counterparts, one can still observe some features that are indicative of the knot's longitudinal compression and the sharper transverse motion that is brought with the reduction of b.

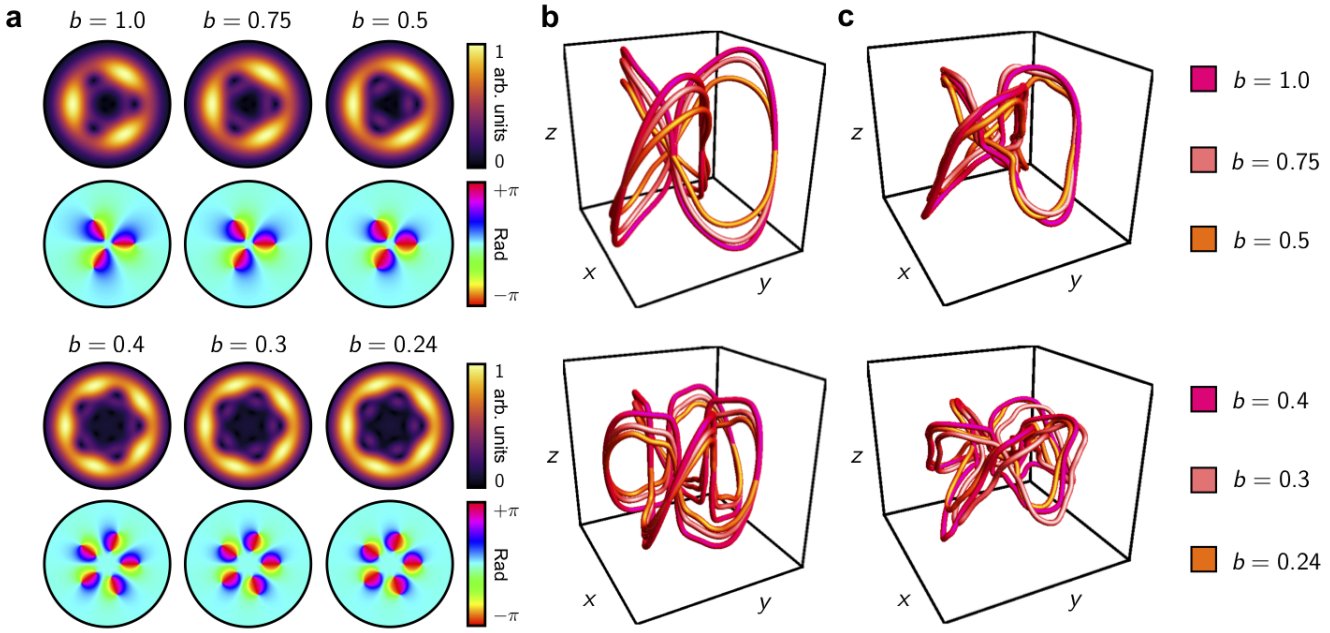

Supplementary Figure 8. **Effect on reducing the b parameter on the knotted optical field. a,** Amplitude and phase profiles of $\psi^{\mathrm{Tref}}_{a=1,b,s=1.2}$ (top) and $\psi^{\mathrm{Cinq}}_{a=0.5,b,s=0.65}$ (bottom). **b,** Knots expected from theory resulting from the paraxial propagation of the optical fields shown in (**a**). **c,** Knots obtained from experiment resulting from the holographic generation of optical beams based on the field profiles shown in (**a**).

One of the main sources of perturbation in the frame of the knots studied in this work are attributed to regions of the C-line that are very close to being parallel to the beam's direction of propagation. In these regions, all of the polarization vectors enclosing the C-line have a major axis that is close to being perpendicular to the knot's trajectory, and therefore to defining the knot's frame. Hence, any small perturbation in the C-line's trajectory, be it numerical or experimental, can have drastic effects on the knots frame and change its total number of half-twist. Therefore, having a knotted C-line with less longitudinal motion, such as those with lower b values, should help with improving the frame's resiliency to perturbations.

Another source of perturbation involves the birth of spurious C-lines that merge with those of the knot. Though they may not affect the knot's topology, they may introduce some swirls in the C-lines which affect the number of half-twists in the frame.

The reconstructed frame of these experimental structures is illustrated in Supplementary Figure 9. As mentioned earlier, decreasing the b parameter of the knotted field results in C-lines with sharper trajectories that are less prone to be oriented along

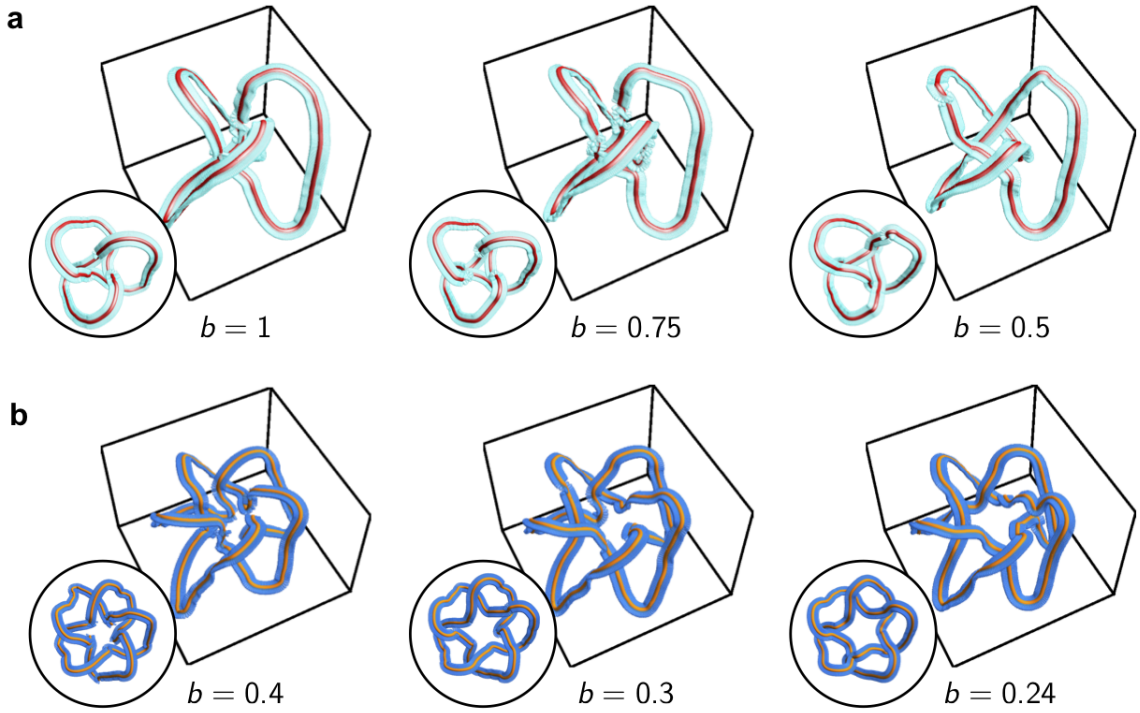

Supplementary Figure 9. **Frame stability of experimentally realized knotted C-lines. a,** Experimental framed trefoil knots defined by parameters of $s = 1.2$ and $a = 1$ and b values of 1, 0.75, and 0.5. **b,** Experimental framed cinquefoil knots defined by parameters of $s = 0.65$ and $a = 0.5$ and b values of 0.4, 0.3, and 0.24. Top views of the knots are provided as insets.

the beam's direction of propagation. Furthermore, fields with lower b parameters also tend to have less secondary singularities affecting the global structure of the knotted C-line. As a result, the frame of these structures globally appears to be more stable.

SUPPLEMENTARY NOTE 6: FRAMED KNOT EXTRACTION FROM RAW DATA

We rely on the procedure outlined in Supplementary Figure 10 to extract the framed knots formed by our optical structures. In the latter, we illustrate this process on the experimental trefoil knot presented in Fig. 4b of the main text. After recording polarization projections of the knotted C-line at several planes along the beam's propagation, we take these raw projections and make them go through a non-aggressive low-pass (LP) filter. This step is depicted in Supplementary Figure 10a. The filtering is performed in order to remove defects associated with dust and damage on the CMOS camera used to capture the image. In Fourier space, the filter specifically consists of a circular box function with a radius of 40 pixels. The filtered projections are then used to calculate the beam's reduced Stokes parameters, defined as

$$s_1 = (H - V)/I_0 \qquad s_2 = (A - D)/I_0 \qquad s_3 = (L - R)/I_0 \tag{23}$$

where H, V, A, D, L, and R represent the horizontal, vertical, anti-diagonal, diagonal, left circular, and right circular projections, respectively. I_0 represents the total intensity of the beam. The positions of the C-lines are then extracted by finding intersections of the phase contours formed by the field $s_1 + is_2$ [15]. This process is illustrated in Supplementary Figure 10b. We then proceed by connecting the location of the C-lines extracted at each measurement plane into the beam's underlying knot. In order to mitigate the effects related to the pixelation of the CMOS measurements, we make the transverse coordinates, i.e., x and y, of the resulting curve go through a Gaussian filter with a width of one bin. A spline going through each of the filtered points is then interpolated to obtain a continuous representation of the curve. The raw coordinates of the knotted C-line along with the spline arising from the interpolation of the filtered data are shown in Supplementary Figure 10c. The raw coordinates of the C-line along with its Gaussian filtered transverse coordinates are plotted in Supplementary Figure 10d. Once we have reconstructed the continuous representation of the knot, we scale it to fit within the proximity of the torus obtained from the stereographic projection of the cylinder enclosing the braid representation of our knot. An image of such a scaled knot along with said torus is provided in Supplementary Figure 10e. Finally, the frame of the knot is obtained by taking the cross product of the knot's tangent and the normal of the C-line's oscillation plane. For the case of paraxial structures, the normal is oriented along the

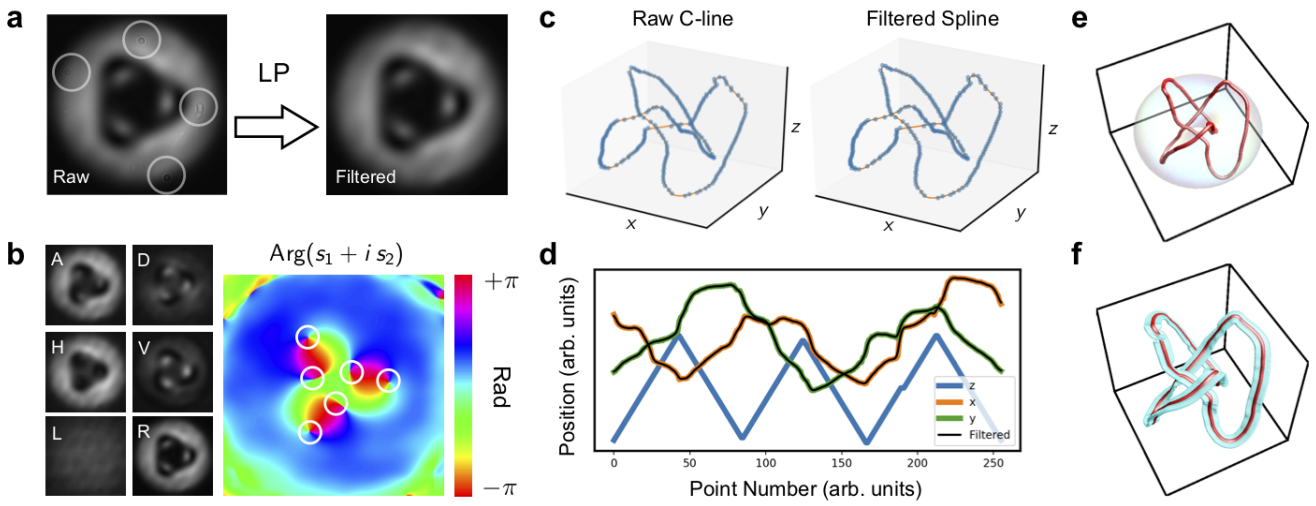

Supplementary Figure 10. **Reconstruction of optical framed knots from raw data. a,** Polarization projections are first low-pass (LP) filtered to remove any defects in the images. Examples of such defects are circled in the raw image. **b,** The filtered polarization projections are then used to obtain the Stokes parameters, s_i, of the beam at various planes along the beam's propagation. Intersections of the phase contours of the field formed by $s_1 + is_2$, herein labeled in the figure, may then pinpoint the location of the C-lines. **c,** Knots formed by the raw coordinates of the C-line extracted in (**b**) and by the spline interpolated C-line where the x and y coordinates have been subjected to a Gaussian filter. **d,** Coordinates of the curve formed by the C-line along with the Gaussian filtered transverse coordinates. **e,** Scaled version of the interpolated knot fitting within the torus related to the stereographic projection used to extract the knot's braid representation. **f,** Final knotted structure accompanied by the frame determined by the oscillation plane of the C-line.

beam's direction of propagation, i.e. the z axis, thereby confining the frame within the xy plane. An image of the resulting structure is displayed in Supplementary Figure 10f.

Supplementary References

[1] Sugic, D. & Dennis, M. R. Singular knot bundle in light. *J. Opt. Soc. Am. A* **35**, 1987–1999 (2018).
[2] Dennis, M. R., King, R. P., Jack, B., O'Holleran, K. & Padgett, M. J. Isolated optical vortex knots. *Nat. Phys.* **6**, 118–121 (2010).
[3] Dennis, M. R., Götte, J. B., King, R. P., Morgan, M. A. & Alonso, M. A. Paraxial and nonparaxial polynomial beams and the analytic approach to propagation. *Opt. Lett.* **36**, 4452–4454 (2011).
[4] Berry, M. V. & Dennis, M. R. Polarization singularities in isotropic random vector waves. *Proc. R. Soc. A* **457**, 141–155 (2001).
[5] Bliokh, K. Y., Alonso, M. A. & Dennis, M. R. Geometric phases in 2d and 3d polarized fields: geometrical, dynamical, and topological aspects. *Rep. Prog. Phys.* **82**, 122401 (2019).
[6] Conway, J. H. An enumeration of knots and links, and some of their algebraic properties. In *Computational Problems in Abstract Algebra*, 329–358 (1970).
[7] Jones, V. F. R. Planar algebras. Preprint at https://arxiv.org/abs/math/9909027 (1999).
[8] Fröhlich, J. & Kerler, T. *Quantum groups, quantum categories and quantum field theory* (Springer, 2006).
[9] Bilson-Thompson, S., Hackett, J., Kauffman, L. & Smolin, L. Particle identifications from symmetries of braided ribbon network invariants. Preprint at https://arxiv.org/abs/0804.0037 (2008).
[10] Bilson-Thompson, S., Hackett, J. & Kauffman, L. H. Particle topology, braids, and braided belts. *J. Math. Phys.* **50**, 113505 (2009).
[11] Gresnigt, N. Knotted boundaries and braid only form of braided belts Preprint at https://arxiv.org/abs/1808.03910 (2018).
[12] Ko, K. H. & Smolinsky, L. The framed braid group and 3-manifolds. *Proc. Am. Math. Soc* **115**, 541–551 (1992).
[13] Kauffman, L. *Knots and Physics* (World Scientific: Singapore, 1991).
[14] Bode, B., Dennis, M. R., Foster, D. & King, R. P. Knotted fields and explicit fibrations for lemniscate knots. *Proc. R. Soc. A* **473**, 20160829 (2017).
[15] Larocque, H. *et al.* Reconstructing the topology of optical polarization knots. *Nat. Phys.* **14**, 1079–1082 (2018).

Appendix C

Supplementary Materials: Topological transitions of the generalized Pancharatnam-Berry phase

Science Advances
AAAS

Supplementary Materials for

Topological transitions of the generalized Pancharatnam-Berry phase

Manuel F. Ferrer-Garcia *et al.*

Corresponding author: Alessio D'Errico, aderrico@uottawa.ca

Sci. Adv. **9**, eadg6810 (2023)
DOI: 10.1126/sciadv.adg6810

This PDF file includes:

Section 1. THEORETICAL PROTOCOL AND ITS RELATION TO THE EXPERIMENTAL SETUP

Here we provide a brief theoretical background on quantum measurement theory, on measurement induced geometric phases, and the topological transition in them, as well as connect the quantum measurement formalism to the optical setup employed in the paper.

A. Null-weak measurements of different observables in the polarisation space

The formalism applies to the transition reported in the main text when regarding the polarisation of the laser beam as a quantum polarisation state $|\theta,\phi\rangle = \cos(\theta/2)\,|\uparrow\rangle + e^{i\phi}\sin(\theta/2)\,|\downarrow\rangle$ of a photon, where $|\uparrow\rangle$ and $|\downarrow\rangle$ label the linearly independent vertical and horizontal polarisations respectively with $\theta \in [0,\pi]$ and $\phi \in [0,2\pi)$.

In the most general setting, a measurement of a quantum system in a state $|\psi\rangle$ returns an outcome r with probability $P(r) = \langle\psi|M_r^\dagger M_r|\psi\rangle$, while the state is updated as $|\psi\rangle \to |\psi'\rangle = M_r\,|\psi\rangle\,/\sqrt{P(r)}$. The process is controlled by the Kraus operators M_r, which depend on the specific detection process and fulfil $\sum_r M_r^\dagger M_r = 1$ due to overall probability conservation [28]. For what we are concerned here, we specialize in a measurement process, known as null weak measurement, with two possible outcomes, $r = +, -$, and corresponding Kraus operators

$$M_+ = \sqrt{\zeta}\,|\downarrow\rangle\langle\downarrow|\,, \quad M_- = |\uparrow\rangle\langle\uparrow| + \sqrt{1-\zeta}\,|\downarrow\rangle\langle\downarrow|\,, \tag{S1}$$

where $0 \le \zeta \le 1$ corresponds to the measurement strength $\eta = \sqrt{-\ln(1-\zeta)}$. For $\zeta = 1$ ($\eta \to \infty$), the measurement is projective: the operation projects the state on $|\downarrow\rangle$ if $r = +$ and $|\uparrow\rangle$ if $r = -$. For $\zeta < 1$, however, we either have a collapse to $|\downarrow\rangle$ ("click", described by M_+) or no collapse ("no-click" or "null measurement", described by M_-). In the latter case, the system's state is updated to a the post-measurement state, which depends on the pre-measurement one.

The measurement procedure in Eq. (S1) corresponds to an imperfect, or weak, measurement of σ_z. This can be generalized to measure arbitrary observables, i.e. to distinguish two arbitrary basis states. A direction $\mathbf{n} = (\sin\theta\cos\phi, \sin\theta\sin\phi, \cos\theta)$ is identified by the polar and azimuthal angles θ and ϕ on the Bloch sphere. The corresponding orthogonal basis states, $|\uparrow_\mathbf{n}\rangle$ and $|\downarrow_\mathbf{n}\rangle$, are defined as eigenstates of $\mathbf{n}\cdot\boldsymbol{\sigma}$ associated with the respective eigenvalue ± 1. For $\phi = 0$ and π these states correspond to two mutually orthogonal linear polarisations, whereas for all other values of ϕ they correspond to general elliptic polarisations. The analog of Eq. (S1) is then given by $M_+(\mathbf{n}) = \sqrt{\zeta}\,|\downarrow_\mathbf{n}\rangle\langle\downarrow_\mathbf{n}|$, $M_-(\mathbf{n}) = |\uparrow_\mathbf{n}\rangle\langle\uparrow_\mathbf{n}| + \sqrt{1-\zeta}\,|\downarrow_\mathbf{n}\rangle\langle\downarrow_\mathbf{n}|$.

B. Measurement-induced geometric phases

In order to induce a geometric phase, one needs to use multiple measurements. We label them by $j = 1, ..., N$. Each measurement is determined by the observable it measures, i.e., by the direction $\mathbf{n}_j$. The respective Kraus operators are $M_{r_j}^{(j)} = M_{r_j}(\mathbf{n}_j)$, where $r_j = \pm$ is the readout of measurement j.

For each such measurement with a given outcome, the phase of the post-measurement state is gauge-dependent, hence non-physical. However, if a sequence of measurements leads to a post-measurement final state $|\psi_f\rangle$ which is proportional to the initial one, $|\psi_0\rangle$, the phase difference between $|\psi_f\rangle$ and $|\psi_0\rangle$ is a legit observable given by

$$\chi_{\{r_j\}} = \arg\langle\psi_0|\psi_f\rangle = \arg\langle\psi_0|\,M_{r_N}^{(N)}\ldots M_{r_2}^{(2)}M_{r_1}^{(1)}\,|\psi_0\rangle\,, \tag{S2}$$

where r_j is the outcome (readout) of the j-th measurement, whose effect is encoded in the Kraus operator $M_{r_j}^{(j)}$.

Note that even if the final state, $|\psi_f\rangle$, differs from the initial one, the phase defined in Eq. (S2) is still well-defined: this can be understood by introducing a fake projective measurement onto the initial state, $|\psi_0\rangle\langle\psi_0|$, after the application of all $M_{r_j}^{(j)}$, in order to force $|\psi_f\rangle \propto |\psi_0\rangle$. Therefore, Eq. (S2) defines a legitimate observable for a general sequence of measurements. The sequence of (normalized) post-measurement intermediate states, $|\psi_0\rangle$, $M_{r_1}^{(1)}|\psi_0\rangle$, ..., $M_{r_N}^{(N)}...M_{r_1}^{(1)}|\psi_0\rangle$, defines a trajectory on the Bloch sphere. This trajectory is given by the set of geodesics connecting the states. For Hermitian Kraus operators, $M_{r_j}^{(j)\dagger} = M_{r_j}^{(j)}$ (which is the case in Eq. (S1)), the measurement-induced phase, (S2), has a geometric interpretation as $\chi_{\{r_j\}} = \Omega/2$, where Ω is the solid angle subtended by the trajectory on the Bloch sphere [22-25].

C. Protocol for topological transition in measurement-induced phases

Consider a family of measurement sequences, defined in the main text. Each sequence consists of N measurements corresponding to $(\theta, \phi_j = 2\pi j/(N+1))$, where $j = 1, ..., N$ is the measurement number. The family is obtained when considering such sequences at all $\theta \in [0, \pi]$. We perform postselection, which restricts measurement readouts to be $r_j = -$ for all j. According to Eq. (S2), this defines a phase $\chi_{\{-\}}(\theta)$ for each measurement sequence in the family. For briefness, we denote this phase $\chi(\theta)$.

The function $\chi(\theta)$ possesses a topological invariant. This follows from the fact that at $\theta = 0$ and $\theta = \pi$, $M_{r_j}^{(j)} |\psi_0\rangle = |\psi_0\rangle$ for all j, implying that $|\psi_f\rangle = |\psi_0\rangle$. That is, the measurements do not change the system state so that the resulting phase is trivial: $e^{i\chi(0)} = e^{i\chi(\pi)} = 1$. As with any phase, the measurement-induced phase is defined up to an integer multiple of 2π. Without loss of generality, we can set $\chi(0) = 0$. This, however, eliminates the freedom of adding multiples of 2π at all other θ due to the natural demand of continuity of $\chi(\theta)$. In particular, $\chi(\pi)$ may be non-zero; yet $e^{i\chi(\pi)} = 1$ implies that $\chi(\pi) = 2\pi m$ with integer m. In other words, the difference $\Delta\chi = \chi(\pi) - \chi(0)$, must be quantized in units of 2π, as stated in the main text. Further, the quantization of $\Delta\chi$ implies that its value cannot be changed by continuous deformations of the function $\chi(\theta)$. Therefore, $\Delta\chi$ constitutes a topological invariant.

As discussed in the main text, for infinitely weak ($\zeta \to 0$) and projective ($\zeta \to 1$) measurements $\Delta\chi_{\zeta\to 0} = 0$ and $\Delta\chi_{\zeta\to 1} = 2\pi$ respectively. This necessitates a jump in the topological invariant, i.e., a topological transition, at some critical measurement strength, $\zeta_c \in [0, 1]$.

D. Detection of measurement-induced geometric phases

In order to detect a measurement-induced phase, one needs to interfere the state that underwent measurements with the initial unmeasured state, as in Fig. 2a of the main text. Here we provide a theoretical description of this in the quantum measurement formalism.

The incoming photon in polarisation state $|\psi_0\rangle$ becomes, after the beam splitter, the state $|\psi\rangle = \frac{1}{\sqrt{2}} |\psi_0\rangle \otimes (|0\rangle + |1\rangle)$ where $|0\rangle$ and $|1\rangle$ refer to the two arms of the interferometer. A sequence of measurements with Kraus operators $M_{r_j}(\mathbf{n}_j)$ is performed in the interferometer arm denoted as $|0\rangle$. The arm denoted as $|1\rangle$ features only a phase shifter, δ. Therefore, after passing through the respective interferometer arms the photon state is

$$|\psi\rangle_{int} = \frac{1}{\sqrt{2}} \left[\sum_{\{r_j\}} |\Psi_0(\{r_j\})\rangle \otimes |0\rangle + |\Psi_1\rangle \otimes |1\rangle \right], \tag{S3}$$

where

$$|\Psi_0(\{r_j\})\rangle = M_{r_N}^{(N)} ... M_{r_1}^{(1)} |\psi_0\rangle \otimes |\{r_j\}\rangle, \tag{S4}$$

$$|\Psi_1\rangle = e^{i\delta} |\psi_0\rangle \otimes |\{r_j = -\}\rangle. \tag{S5}$$

Here we introduced the collective state of all the detectors, $|\{r_j\}\rangle$. In the arm denoted by $|1\rangle$ the detectors do not interact with the photon and thus stay in the no-click position.

The second beam splitter converts $|0\rangle \to \frac{1}{\sqrt{2}}(|0\rangle + |1\rangle)$, $|1\rangle \to \frac{1}{\sqrt{2}}(|0\rangle - |1\rangle)$, so that the output state is

$$|\psi\rangle_{out} = \frac{1}{2} \left[\left(|\Psi_1\rangle + \sum_{\{r_j\}} |\Psi_0(\{r_j\})\rangle \right) \otimes |0\rangle + \left(-|\Psi_1\rangle + \sum_{\{r_j\}} |\Psi_0(\{r_j\})\rangle \right) \otimes |1\rangle \right]. \tag{S6}$$

Therefore, the probability of the photon appearing at output ports $|0\rangle$ or $|1\rangle$ is given by

$$\begin{aligned} P_{0/1} &= \frac{1}{2} \left[1 \pm \sum_{\{r_j\}} \mathrm{Re}\, e^{-i\delta} \langle \Psi_1 | \Psi_0(\{r_j\}) \rangle \right] \\ &= \frac{1}{2} \left[1 \pm \mathrm{Re}\, e^{-i\delta} \langle \psi_0 | M_-^{(N)} ... M_-^{(1)} |\psi_0\rangle \right]. \end{aligned} \tag{S7}$$

Note that only the term with no-click readouts, $\{r_j = -\}$, in the measured interferometer arm contributes to the interference, which thus enables the observation of the measurement-induced phase, cf. Eq. (S2) and Section 1 B. In other words, the interference implicitly performs the postselection to $\{r_j = -\}$ required by the definition of $\chi(\theta)$, cf. Section 1 C.

Section 2. EFFECT OF IMPERFECT BIREFRINGENT CRYSTALS

In this section, we discuss some details about the modeling and exploration of the possible defects that may explain the mismatch between the theory and experimental results. While a plethora of plausible defects may occur in our system, it has been assumed that the optical properties of any element correspond to the nominal ones given by the manufacturing companies. Therefore, the study focuses on the effects of minor misalignment on the optical elements, such as incorrect rotation of the QWP at each stage, the imperfect placing of the compensation plate, and non-parallel output beams exiting the Beam displacer. While our preliminary calculations show that these imperfections lead to translation on the transition point. We found that the main contribution to the shift of the transition point is given by effects in which the field's extraordinary and ordinary components exit from the birefringent crystal with slightly non-parallel propagation directions. While the non-parallelism can result from minor misalignment, the beam displacer (THORLABS3 BDY12) manufacturer mentions that both components are parallel to each other within 30 arcseconds. Figure **S1**-b shows the intensity profile from a YBO_4 crystal when illuminated with diagonally polarized light, and a polariser is placed on the output. The presence of an interference pattern corroborates the existence of a slight deviation in the propagation direction of one of the output beams.

Following these results, we modified the model for our beam displacer to account for our crystals' imperfections. For the sake of a simpler model, higher order optical aberrations have not been considered, despite the intensity profile in Figure **S1**-b depicts an indication of their presence. First, we assumed that only the extraordinary component experiences a deflection from the optical axis by an angle β. Due to variability from one crystal to another, we allow the deviation to occur along any direction in the transverse plane, characterized by an angle ν. Therefore, it is possible to write the effect of an imperfect beam displacer on an impinging electric field as

$$\mathbf{E}(x,y) = \mathrm{BD}_{\nu,\beta}\,\mathbf{E}_0(x,y) = \sqrt{\frac{2}{\pi w_0^2}}\begin{pmatrix} e^{ikn_yL_y}E_{0y}e^{-(x^2+y^2)/w_0^2} \\ e^{ikn_xL_x+i\Delta(x,y)}E_{0x}e^{-([x-d_x]^2+y^2)/w_0^2}\end{pmatrix}e^{ikz}. \tag{S8}$$

where $\Delta(x,y) = k\sin\beta(\cos\nu x + \sin\nu y)$ implements the deflection on the extraordinary component. Therefore, it is possible to describe the evolution of the input beam $\mathbf{E}_0(x,y)$ due to a sequence of N stages with distinct imperfections as

$$\mathbf{E}_\mathbf{u}(x,y) = \prod_{j=1}^{N}\mathcal{M}_{\nu_j,\beta_j}(\theta,\phi_j)\mathbf{E}_0(x,y), \tag{S9}$$

where $\mathcal{M}_{\nu,\beta}(\theta,\phi)$ is obtained by substituting Eq. (S8) into Eq. 9 (Methods Section). A first glance at the effect of these imperfections on the location of the transition is obtained when considering the case when the $N=3$ measurement stages possess identical crystals. As shown in Figure **S1**c, the location of the topological transition shifts towards higher values of w_0 when the deflection angle increases.

Although the results shown in Figure **S1**c demonstrate that non-parallel output beams have a dramatic effect on the location of the transition, the assumption of three identical crystals is not valid in our experiment. As a consequence, the behavior of the geometrical phase curve depends directly on three pairs (ν,β), which quantify the non-parallelism between the faces of each BD. A genetic algorithm (GA)[29] was implemented to perform the search for the set of optimal parameters $P = \{\nu_1,\beta_1,\nu_2,\beta_2,\nu_3,\beta_3\}$ that match the experimental results. It should be noted that it is possible to calculate a deviation from the interference pattern in Figure **S1**b. Additional corrections due to small curvatures in the crystals surfaces could be responsible for residual mismatches between experiment and theory

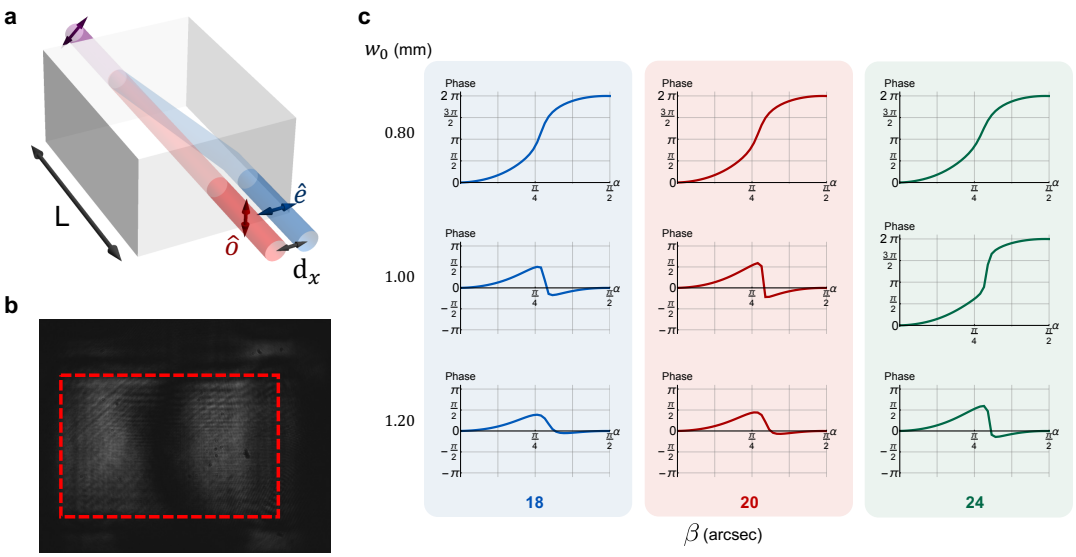

Figure S1. **Modeling an imperfect beam displacer. a.** Schematic of a beam displacer (BD). **b.** Interference pattern obtained from the output beams after projecting on circular polarisation (and with a circularly polarized input beam). **c.** Geometrical phase curves for different values of the deviation angle β.

REFERENCES AND NOTES

1. M. V. Berry, Quantal phase factors accompanying adiabatic changes. *Proc. R. Soc. Lond.* **392**, 45–57 (1984).
2. S. Pancharatnam, Generalized theory of interference, and its applications. *Proc. Indian Acad. Sci. A.* **44**, 247–262 (1956).
3. J. Samuel, R. Bhandari, General setting for berry's phase. *Phys. Rev. Lett.* **60**, 2339–2342 (1988).
4. M. V. Berry, S. Klein, Geometric phases from stacks of crystal plates. *J. Mod. Optic.* **43**, 165–180 (1996).
5. D. Chruscinski, A. Jamiolkowski, *Geometric Phases in Classical and Quantum Mechanics* (Birkhäuser Basel, 2004).
6. E. Cohen, H. Larocque, F. Bouchard, F. Nejadsattari, Y. Gefen, E. Karimi, Geometric phase from Aharonov–Bohm to Pancharatnam–Berry and beyond. *Nat. Rev. Phys.* **1**, 437–449 (2019).
7. Z. Bomzon, G. Biener, V. Kleiner, E. Hasman, Space-variant Pancharatnam–Berry phase optical elements with computer-generated subwavelength gratings. *Opt. Lett.* **27**, 1141–1143 (2002).
8. K. Y. Bliokh, M. A. Alonso, M. R. Dennis, Geometric phases in 2d and 3d polarized fields: Geometrical, dynamical, and topological aspects. *Rep. Prog. Phys.* **82**, 122401 (2019).
9. A. Rubano, F. Cardano, B. Piccirillo, L. Marrucci, Q-plate technology: A progress review [Invited]. *J. Opt. Soc. Am. B.* **36**, D70 (2019).
10. C. P. Jisha, S. Nolte, A. Alberucci, Geometric phase in optics: From wavefront manipulation to waveguiding. *Laser & Photonics Reviews* **15**, 2100003 (2021).
11. H. C. Higgins, Öpik, H. C. Longuet-Higgins, U. Öpik, M. H. L. Pryce, R. A. Sack, Studies of the jahn-teller effect. II. the dynamical problem. *Proc. R Soc. Lond.* **244**, 1–16 (1958).
12. J. Zak, Berry's phase for energy bands in solids. *Phys. Rev. Lett.* **62**, 2747–2750 (1989).
13. R. Resta, Manifestations of berry's phase in molecules and condensed matter. *J. Phys. Condens. Matter* **12**, R107–R143 (2000).
14. C. Nayak, S. H. Simon, A. Stern, M. Freedman, S. D. Sarma, Non-abelian anyons and topological quantum computation. *Rev. Mod. Phys.* **80**, 1083–1159 (2008).
15. E. Fradkin, *Field Theories of Condensed Matter Physics* (Cambridge Univ. Press, 2013).
16. R. Resta, Macroscopic polarization in crystalline dielectrics: The geometric phase approach. *Rev. Mod. Phys.* **66**, 899–915 (1994).

17. J. K. Asbóth, L. Oroszlány, A. Pályi, A short course on topological insulators. *Lecture Notes in Physics* **919**, 166 (2016).
18. M. Z. Hasan, C. L. Kane, Colloquium: Topological insulators. *Rev. Mod. Phys.* **82**, 3045–3067 (2010).
19. J. Garrison, E. Wright, Complex geometrical phases for dissipative systems. *Phys. Lett. A.* **128**, 177–181 (1988).
20. G. Dattoli, R. Mignani, A. Torre, Geometrical phase in the cyclic evolution of non-hermitian systems. *J. Phys. A Math. Gen.* **23**, 5795–5806 (1990).
21. R. El-Ganainy, K. G. Makris, M. Khajavikhan, Z. H. Musslimani, S. Rotter, D. N. Christodoulides, Non-Hermitian physics and PT symmetry. *Nat. Phys.* **14**, 11–19 (2018).
22. Y.-W. Cho, Y. Kim, Y.-H. Choi, Y.-S. Kim, S.-W. Han, S.-Y. Lee, S. Moon, Y.-H. Kim, Emergence of the geometric phase from quantum measurement back-action. *Nat. Phys.* **15**, 665–670 (2019).
23. V. Gebhart, K. Snizhko, T. Wellens, A. Buchleitner, A. Romito, Y. Gefen, Topological transition in measurement-induced geometric phases. *Proc. Natl. Acad. Sci. U.S.A.* **117**, 5706–5713 (2020).
24. K. Snizhko, P. Kumar, N. Rao, Y. Gefen, Weak-measurement-induced asymmetric dephasing: Manifestation of intrinsic measurement chirality. *Phys. Rev. Lett.* **127**, 170401 (2021).
25. K. Snizhko, N. Rao, P. Kumar, Y. Gefen, Weak measurement-induced phases and dephasing: Broken symmetry of the geometric phase. *Phys. Rev. Res.* **3**, 043045 (2021).
26. Y. Wang, K. Snizhko, A. Romito, Y. Gefen, K. Murch, Observing a topological transition in weak-measurement-induced geometric phases. *Phys. Rev. Res.* **4**, 023179 (2022).
27. E. Bolduc, N. Bent, E. Santamato, E. Karimi, R. W. Boyd, Exact solution to simultaneous intensity and phase encryption with a single phase-only hologram. *Opt. Lett.* **38**, 3546–3549 (2013).
28. K. Jacobs, *Quantum Measurement Theory and its Applications* (Cambridge Univ. Press, 2014).
29. D. A. Coley, *An Introduction to Genetic Algorithms for Scientists and Engineers* (World Scientific Publishing Company, 1999).

References

[1] James Clerk Maxwell. *A treatise on electricity and magnetism*, volume 1. Clarendon press, 1873.

[2] Max Born and Emil Wolf. *Principles of optics: electromagnetic theory of propagation, interference and diffraction of light*. CUP Archive, 2000.

[3] Gregory J Gbur. *Singular optics*. CRC press, 2016.

[4] Paul Adrien Maurice Dirac. Quantised singularities in the electromagnetic field. *Proceedings of the Royal Society of London. Series A, Containing Papers of a Mathematical and Physical Character*, 133(821):60–72, 1931.

[5] Hans Wolter. Zur frage des lichtweges bei totalreflexion. *Zeitschrift für Naturforschung A*, 5(5):276–283, 1950.

[6] A Boivin, J Dow, and E Wolf. Energy flow in the neighborhood of the focus of a coherent beam. *JOSA*, 57(10):1171–1175, 1967.

[7] John Frederick Nye and Michael Victor Berry. Dislocations in wave trains. *Proceedings of the Royal Society of London. A. Mathematical and Physical Sciences*, 336(1605):165–190, 1974.

[8] Michael V Berry. Geometry of phase and polarization singularities illustrated by edge diffraction and the tides. In *Second International Conference on Singular Optics (Optical Vortices): Fundamentals and Applications*, volume 4403, pages 1–12. SPIE, 2001.

[9] NB Baranova and B Ya Zel'dovich. Dislocations of the wave-front surface and zeros of the amplitude. *Zh. Eksp. Teor. Fiz*, 80:1789–1797, 1981.

[10] David L Andrews and Mohamed Babiker. *The angular momentum of light*. Cambridge University Press, 2012.

[11] Les Allen, Marco W Beijersbergen, RJC Spreeuw, and JP Woerdman. Orbital angular momentum of light and the transformation of laguerre-gaussian laser modes. *Physical review A*, 45(11):8185, 1992.

[12] John Frederick Nye. Lines of circular polarization in electromagnetic wave fields. *Proceedings of the Royal Society of London. A. Mathematical and Physical Sciences*, 389(1797):279–290, 1983.

[13] Amber M Beckley, Thomas G Brown, and Miguel A Alonso. Full poincaré beams. *Optics express*, 18(10):10777–10785, 2010.

[14] Bienvenu Ndagano, Isaac Nape, Mitchell A Cox, Carmelo Rosales-Guzman, and Andrew Forbes. Creation and detection of vector vortex modes for classical and quantum communication. *Journal of Lightwave Technology*, 36(2):292–301, 2017.

[15] Alan E Willner, Hao Huang, Yan Yan, Yongxiong Ren, Nisar Ahmed, Goudong Xie, Changjing Bao, L Li, Y Cao, Z Zhao, et al. Optical communications using orbital angular momentum beams. *Advances in optics and photonics*, 7(1):66–106, 2015.

[16] Graham Gibson, Johannes Courtial, Miles J Padgett, Mikhail Vasnetsov, Valeriy Pas'ko, Stephen M Barnett, and Sonja Franke-Arnold. Free-space information transfer using light beams carrying orbital angular momentum. *Optics express*, 12(22):5448–5456, 2004.

[17] Frédéric Bouchard, Alicia Sit, Felix Hufnagel, Aazad Abbas, Yingwen Zhang, Khabat Heshami, Robert Fickler, Christoph Marquardt, Gerd Leuchs, Ebrahim Karimi, et al. Quantum cryptography with twisted photons through an outdoor underwater channel. *Optics express*, 26(17):22563–22573, 2018.

[18] Rui Chen, Krishna Agarwal, Colin JR Sheppard, and Xudong Chen. Imaging using cylindrical vector beams in a high-numerical-aperture microscopy system. *Optics letters*, 38(16):3111–3114, 2013.

[19] Karl Zhanghao, Xingye Chen, Wenhui Liu, Meiqi Li, Yiqiong Liu, Yiming Wang, Sha Luo, Xiao Wang, Chunyan Shan, Hao Xie, et al. Super-resolution imaging of fluorescent dipoles via polarized structured illumination microscopy. *Nature Communications*, 10(1):4694, 2019.

[20] Michael V Berry and Mark R Dennis. Knotted and linked phase singularities in monochromatic waves. *Proceedings of the Royal Society of London. Series A: Mathematical, Physical and Engineering Sciences*, 457(2013):2251–2263, 2001.

[21] Danica Sugic and Mark R Dennis. Singular knot bundle in light. *JOSA A*, 35(12):1987–1999, 2018.

[22] Mark R Dennis, Robert P King, Barry Jack, Kevin O'holleran, and Miles J Padgett. Isolated optical vortex knots. *Nature Physics*, 6(2):118–121, 2010.

[23] Louis H Kauffman. *Knots and physics*, volume 1. World scientific, 2001.

[24] Antonio F Ranada. A topological theory of the electromagnetic field. *Letters in Mathematical Physics*, 18:97–106, 1989.

[25] Hridesh Kedia, Iwo Bialynicki-Birula, Daniel Peralta-Salas, and William TM Irvine. Tying knots in light fields. *Physical review letters*, 111(15):150404, 2013.

[26] NA Veretenov, SV Fedorov, and NN Rosanov. Topological three-dimensional dissipative optical solitons. *Philosophical Transactions of the Royal Society A: Mathematical, Physical and Engineering Sciences*, 376(2124):20170367, 2018.

[27] Max Born and Emil Wolf. *Principles of optics: electromagnetic theory of propagation, interference and diffraction of light*. Elsevier, 2013.

[28] John David Jackson. Classical electrodynamics, 1999.

[29] Parry Moon and Domina E Spencer. *Field theory handbook: including coordinate systems, differential equations and their solutions*. Springer, 2012.

[30] Russell A Chipman, Wai Sze Tiffany Lam, and Garam Young. *Polarized light and optical systems*. CRC press, 2018.

[31] George Gabriel Stokes. On the composition and resolution of streams of polarized light from different sources. *Transactions of the Cambridge Philosophical Society*, 9:399, 1851.

[32] H Poincaré. *Théorie mathématique de la lumière: cours de Physique Mathématique*. Georges Carré Editeur, 1889.

[33] Shivaramakrishnan Pancharatnam. Generalized theory of interference, and its applications: Part i. coherent pencils. In *Proceedings of the Indian Academy of Sciences-Section A*, volume 44, pages 247–262. Springer, 1956.

[34] Dennis G Hall. Vector-beam solutions of maxwell's wave equation. *Optics letters*, 21(1):9–11, 1996.

[35] Rebecca H Jordan and Dennis G Hall. Free-space azimuthal paraxial wave equation: the azimuthal bessel–gauss beam solution. *Optics letters*, 19(7):427–429, 1994.

[36] Eileen Otte, Christina Alpmann, and Cornelia Denz. Tailored vectorial light fields: flower, spider web and hybrid structures. In *Optical Manipulation Conference*, volume 10252, pages 30–33. SPIE, 2017.

[37] Qiwen Zhan. Cylindrical vector beams: from mathematical concepts to applications. *Advances in Optics and Photonics*, 1(1):1–57, 2009.

[38] Yuichi Kozawa and Shunichi Sato. Optical trapping of micrometer-sized dielectric particles by cylindrical vector beams. *Optics Express*, 18(10):10828–10833, 2010.

[39] Min-Cheng Zhong, Lei Gong, Di Li, Jin-Hua Zhou, Zi-Qiang Wang, and Yin-Mei Li. Optical trapping of core-shell magnetic microparticles by cylindrical vector beams. *Applied Physics Letters*, 105(18), 2014.

[40] H Moradi, V Shahabadi, E Madadi, E Karimi, and F Hajizadeh. Efficient optical trapping with cylindrical vector beams. *Optics express*, 27(5):7266–7276, 2019.

[41] Wen Qiao, Ting Lei, Zhentian Wu, Shecheng Gao, Zhaohui Li, and Xiaocong Yuan. Approach to multiplexing fiber communication with cylindrical vector beams. *Optics letters*, 42(13):2579–2582, 2017.

[42] Qiwen Zhan and James R Leger. Focus shaping using cylindrical vector beams. *Optics Express*, 10(7):324–331, 2002.

[43] Emil Wolf. Electromagnetic diffraction in optical systems-i. an integral representation of the image field. *Proceedings of the Royal Society of London. Series A. Mathematical and Physical Sciences*, 253(1274):349–357, 1959.

[44] Bernard Richards and Emil Wolf. Electromagnetic diffraction in optical systems, ii. structure of the image field in an aplanatic system. *Proceedings of the Royal Society of London. Series A. Mathematical and Physical Sciences*, 253(1274):358–379, 1959.

[45] George B Arfken and Hans J Weber. Mathematical methods for physicists, 1999.

[46] Isaac Freund. Bichromatic optical lissajous fields. *Optics communications*, 226(1-6):351–376, 2003.

[47] Thomas Bauer, Sergej Orlov, Ulf Peschel, Peter Banzer, and Gerd Leuchs. Nanointerferometric amplitude and phase reconstruction of tightly focused vector beams. *Nature Photonics*, 8(1):23–27, 2014.

[48] Pedro A Quinto-Su. Interferometric measurement of arbitrary propagating vector beams that are tightly focused. *arXiv preprint arXiv:2304.00640*, 2023.

[49] Iosif Demirtzioglou, Cosimo Lacava, Kyle RH Bottrill, David J Thomson, Graham T Reed, David J Richardson, and Periklis Petropoulos. Frequency comb generation in a silicon ring resonator modulator. *Optics express*, 26(2):790–796, 2018.

[50] Andrew M Weiner. Femtosecond pulse shaping using spatial light modulators. *Review of scientific instruments*, 71(5):1929–1960, 2000.

[51] Shilong Liu, Yingwen Zhang, Boris A Malomed, and Ebrahim Karimi. Experimental realisations of the fractional schrödinger equation in the temporal domain. *Nature Communications*, 14(1):222, 2023.

[52] LA Vaĭnshteĭn. Propagation of pulses. *Soviet Physics Uspekhi*, 19(2):189, 1976.

[53] Miguel A Porras. Ultrashort pulsed gaussian light beams. *Physical Review E*, 58(1):1086, 1998.

[54] Joseph W Goodman. *Introduction to Fourier optics*. Roberts and Company publishers, 2005.

[55] Benjamin Brecht, Dileep V Reddy, Christine Silberhorn, and Michael G Raymer. Photon temporal modes: a complete framework for quantum information science. *Physical Review X*, 5(4):041017, 2015.

[56] Michael G Raymer and Ian A Walmsley. Temporal modes in quantum optics: then and now. *Physica Scripta*, 95(6):064002, 2020.

[57] Konstantin Y Bliokh and Franco Nori. Spatiotemporal vortex beams and angular momentum. *Physical Review A*, 86(3):033824, 2012.

[58] AP Sukhorukov and VV Yangirova. Spatio-temporal vortices: properties, generation and recording. In *Nonlinear Optics Applications*, volume 5949, pages 35–43. SPIE, 2005.

[59] Nihal Jhajj, Ilia Larkin, EW Rosenthal, Sina Zahedpour, JK Wahlstrand, and HM Milchberg. Spatiotemporal optical vortices. *Physical Review X*, 6(3):031037, 2016.

[60] Nikitas Papasimakis, Tim Raybould, Vassili A. Fedotov, Din Ping Tsai, Ian Youngs, and Nikolay I. Zheludev. Pulse generation scheme for flying electromagnetic doughnuts. *Phys. Rev. B*, 97:201409, May 2018.

[61] Chenhao Wan, Qian Cao, Jian Chen, Andy Chong, and Qiwen Zhan. Toroidal vortices of light. *Nature Photonics*, 16(7):519–522, 2022.

[62] Yijie Shen, Qiang Zhang, Peng Shi, Luping Du, Anatoly V Zayats, and Xiaocong Yuan. Topological quasiparticles of light: optical skyrmions and beyond. *arXiv preprint arXiv:2205.10329*, 2022.

[63] Sergeĭ Aleksandrovich Akhmanov, Viktor Andreevich Vysloukh, Anatoliĭ Stepanovich Chirkin, and Yuri Atanov. *Optics of femtosecond laser pulses*. Springer, 1992.

[64] SW Hancock, S Zahedpour, A Goffin, and HM Milchberg. Free-space propagation of spatiotemporal optical vortices. *Optica*, 6(12):1547–1553, 2019.

[65] Andrew M Weiner. *Ultrafast optics*. John Wiley & Sons, 2011.

[66] B Piglosiewicz, D Sadiq, M Mascheck, S Schmidt, M Silies, P Vasa, and C Lienau. Ultrasmall bullets of light—focusing few-cycle light pulses to the diffraction limit. *Optics Express*, 19(15):14451–14463, 2011.

[67] Ebrahim Karimi, Carlo Altucci, Valer Tosa, Raffaele Velotta, and Lorenzo Marrucci. Influence of generalized focusing of few-cycle gaussian pulses in attosecond pulse generation. *Optics Express*, 21(21):24991–24999, 2013.

[68] Dustin H Froula, David Turnbull, Andrew S Davies, Terrance J Kessler, Dan Haberberger, John P Palastro, Seung-Whan Bahk, Ildar A Begishev, Robert Boni, Sara Bucht, et al. Spatiotemporal control of laser intensity. *Nature photonics*, 12(5):262–265, 2018.

[69] Tanner T Simpson, Dillon Ramsey, Philip Franke, Navid Vafaei-Najafabadi, David Turnbull, Dustin H Froula, and John P Palastro. Nonlinear spatiotemporal control of laser intensity. *Optics Express*, 28(26):38516–38526, 2020.

[70] Zhangyu Zhou, Changjun Min, Haixiang Ma, Yuquan Zhang, Xi Xie, Hao Zhan, and Xiaocong Yuan. Time-varying orbital angular momentum in tight focusing of ultrafast pulses. *Optics Express*, 30(8):13416–13433, 2022.

[71] Jian Chen, Lihua Yu, Chenhao Wan, and Qiwen Zhan. Spin–orbit coupling within tightly focused circularly polarized spatiotemporal vortex wavepacket. *ACS Photonics*, 9(3):793–799, 2022.

[72] RENZO L. RICCA and BERNARDO NIPOTI. Gauss' linking number revisited. *Journal of Knot Theory and Its Ramifications*, 20(10):1325–1343, 2011.

[73] Daniel S. Silver. Knot theory's odd origins: The modern study of knots grew out an attempt by three 19th-century scottish physicists to apply knot theory to fundamental questions about the universe. *American Scientist*, 94(2):158–165, 2006.

[74] De Witt Sumners. Dna, knots and tangles. In *The Mathematics of Knots: Theory and Application*, pages 327–353. Springer, 2011.

[75] Erica Flapan. *When Topology Meets Chemistry: A Topological Look at Molecular Chirality*. Outlooks. Cambridge University Press, 2000.

[76] Tomáš Liko and Louis H Kauffman. Knot theory and a physical state of quantum gravity. *Classical and Quantum Gravity*, 23(4):R63, jan 2006.

[77] Louis H Kauffman and Samuel J Lomonaco. Topological quantum information theory. In *Proceedings of Symposia in Applied Mathematics*, volume 68, 2009.

[78] Kurt Reidemeister. *Knotentheorie*, volume 1. Springer-Verlag, 2013.

[79] Charilaos N Aneziris. *The mystery of knots: computer programming for knot tabulation*, volume 20. World Scientific, 1999.

[80] Peter R Cromwell et al. *Knots and links*. Cambridge university press, 2004.

[81] James W Alexander. Topological invariants of knots and links. *Transactions of the American Mathematical Society*, 30(2):275–306, 1928.

[82] Benjamin Bode, Mark R Dennis, David Foster, and Robert P King. Knotted fields and explicit fibrations for lemniscate knots. *Proceedings of the Royal Society A: Mathematical, Physical and Engineering Sciences*, 473(2202):20160829, 2017.

[83] Hugo Larocque, Danica Sugic, Dominic Mortimer, Alexander J Taylor, Robert Fickler, Robert W Boyd, Mark R Dennis, and Ebrahim Karimi. Reconstructing the topology of optical polarization knots. *Nature Physics*, 14(11):1079–1082, 2018.

[84] Nazanin Dehghan, Alessio D'Errico, Tareq Jaouni, and Ebrahim Karimi. Effect of aberrations on 3d optical topologies. *arXiv preprint arXiv:2302.11531*, 2023.

[85] Viktor Vasilevich Prasolov and Alekseĭ Bronislavovich Sosinskiĭ. *Knots, links, braids and 3-manifolds: an introduction to the new invariants in low-dimensional topology*. Number 154. American Mathematical Soc., 1997.

[86] James W Alexander. A lemma on systems of knotted curves. *Proceedings of the National Academy of Sciences*, 9(3):93–95, 1923.

[87] Andrei Markoff. Uber die freie aquivalenz der geschlossenen zopfe. , 1(1):73–78, 1936.

[88] Mohamed Elhamdadi, Mustafa Hajij, and Kyle Istvan. Framed knots. *The Mathematical Intelligencer*, 42:7–22, 2020.

[89] Ki Hyoung Ko and Lawrence Smolinsky. The framed braid group and 3-manifolds. *Proceedings of the American Mathematical Society*, 115(2):541–551, 1992.

[90] John Von Neumann. *Mathematical foundations of quantum mechanics: New edition*, volume 53. Princeton university press, 2018.

[91] Eliahu Cohen. What weak measurements and weak values really mean: reply to kastner. *Foundations of Physics*, 47(10):1261–1266, 2017.

[92] Valentin Gebhart, Kyrylo Snizhko, Thomas Wellens, Andreas Buchleitner, Alessandro Romito, and Yuval Gefen. Topological transition in measurement-induced geometric phases. *Proceedings of the National Academy of Sciences*, 117(11):5706–5713, 2020.

[93] Michael Berry. The geometric phase. *Scientific American*, 259(6):46–55, 1988.

[94] John Oprea. Geometry and the foucault pendulum. *The American mathematical monthly*, 102(6):515–522, 1995.

[95] Michael Victor Berry. Quantal phase factors accompanying adiabatic changes. *Proceedings of the Royal Society of London. A. Mathematical and Physical Sciences*, 392(1802):45–57, 1984.

[96] Alfred Shapere and Frank Wilczek. *Geometric phases in physics*, volume 5. World scientific, 1989.

[97] JN Ross. The rotation of the polarization in low birefringence monomode optical fibres due to geometric effects. *Optical and Quantum electronics*, 16:455–461, 1984.

[98] Raymond Y Chiao and Yong-Shi Wu. Manifestations of berry's topological phase for the photon. *Physical review letters*, 57(8):933, 1986.

[99] FDM Haldane. Path dependence of the geometric rotation of polarization in optical fibers. *Optics letters*, 11(11):730–732, 1986.

[100] Raymond Y Chiao and Thomas F Jordan. Lorentz-group berry phases in squeezed light. *Physics Letters A*, 132(2-3):77–81, 1988.

[101] M Kitano and T Yabuzaki. Observation of lorentz-group berry phases in polarization optics. *Physics Letters A*, 142(6-7):321–325, 1989.

[102] H Svensmark and P Dimon. Experimental observation of berry's phase of the lorentz group. *Physical review letters*, 73(25):3387, 1994.

[103] George Casella and Roger L Berger. *Statistical inference*. Cengage Learning, 2021.

[104] Jun John Sakurai and Eugene D Commins. Modern quantum mechanics, revised edition, 1995.

[105] Yakir Aharonov, David Z Albert, and Lev Vaidman. How the result of a measurement of a component of the spin of a spin-1/2 particle can turn out to be 100. *Physical review letters*, 60(14):1351, 1988.

[106] Yakir Aharonov and Lev Vaidman. Properties of a quantum system during the time interval between two measurements. *Physical Review A*, 41(1):11, 1990.